UNIVERSITY OF CALIFORNIA SAN DIEGO

Development of Silica Hollow Shells for Ultrasound Imaging and Cancer Immunotherapy

A dissertation submitted in partial satisfaction of the requirements for the degree Doctor of Philosophy

in

Materials Science and Engineering

by

Ching-Hsin Huang

Committee in Charge:

Professor Andrew C. Kummel, Chair
Professor Jesse Jokerst
Professor Tony Reid
Professor William C. Trogler
Professor Liangfang Zhang

2021

The dissertation of Ching-Hsin Huang is approved, and it is acceptable in quality and form for publication on microfilm and electronically.

University of California San Diego
2021

DEDICATION

This work is dedicated to my father, I Huang.

TABLE OF CONTENTS

LIST OF FIGURES AND TABLES

ACKNOWLEDGEMENTS

First and foremost, I would like to thank my advisor, Professor Andrew Kummel. Without his guidance and persistent help, this dissertation would not have been possible. I would also like to acknowledge my collaborators, the Carson lab, Professor William Trogler, the Reid lab, the Gude lab, and Professor Sarah Blair. Their support has helped me in an immeasurable way.

I would like to thank my lab mates Dr. James Wang, Dr. Natalie Mendez, Dr. Jian Yang, , Maggie Tsai, and Adrian Garcia Badaracco for being the best lab mates and friends anyone could hope for.

I would like to thank my collaborators for always being willing to help in any way they could: Dr. Dennis Carson, Dr. Tomoko Hayashi, Dr. Christopher Larson, Dr. Ana Sanchez, Dr. Natalie Gude, Dr. Joi Weeks, Dr. Tadashi Hosoya, Dr. Fumi Sato-Kaneko, Dr. Howard Cottam, Oscar Hernandez Echeagaray, Shiyin Yao, Christopher Barback, Mike Chen, and Fitzgerald Lao. Their insight in countless discussions has helped me immensely in my graduate career.

I want to thank my committee members for actively participating in my senate and thesis defense presentations. My committee includes Professor Andrew Kummel, Professor William Trogler, Professor Tony Reid, Professor Jesse Jokerst, Professor Liangfang Zhang.

Finally, I want to give thanks for the continuous support from my family and friends. I would like to thank my father I Huang for being a role model and superman in my life. I would like to thank my mother Hsin-Ping Ding for showing me it is normal to pursue your dreams anytime, anywhere. I want to thank my sister Ching-Fang Huang and my brother Cheng-Chun Huang, of whom I have many fond memories and will be with me always. I would like to thank my dear friends Ti Wu, Fannie Yu, and Blanca Leon Pulido whose friendship has made my graduate years full of joy.

Chapter 1, in full, is a reprint of the material as it appears in Advanced Functional Materials 2019. Huang, Ching-Hsin; Wang James; Yang, Jian; Oviedo, Juan Pablo; Nam, Seungjin; Trogler, William C.; Blair, Sarah L.; Kim, Moon J.; Kummel, Andrew C., Wiley, 2019. The dissertation author was the primary author of this paper.

Chapter 2, in full, contains material as it appears in ACS Applied Materials & Interfaces 2019. Huang, Ching-Hsin; Mendez, Natalie; Echeagaray, Oscar Hernandez; Weeks, Joi; Wang, James; Vallez, Charles N.; Gude, Natalie; Trogler, William; Carson, Dennis A.; Hayashi, Tomoko; Kummel, Andrew C., ACS Publications, 2019. The dissertation author was the primary author of this paper.

Chapter 3, in full, contains material as it appears in Advanced Therapeutics 2020. Huang, Ching-Hsin; Mendez, Natalie; Echeagaray, Oscar Hernandez; Weeks, Joi; Wang, James; Yao, Shiyin; Blair, Sarah L.; Gude, Natalie; Trogler, William; Carson, Dennis A.; Hayashi, Tomoko; Kummel, Andrew C., Wiley, 2020. The dissertation author was the primary author of this paper.

VITA

2013 Bachelor of Science, National Cheng Kung University

2016 Master of Science, University of California San Diego

2021 Doctor of Philosophy, University of California San Diego

PUBLICATIONS

C.-H. Huang, T. Dong, A. Phung, C. Larson, A. Sanchez, S. Blair, T. Reid, W. Trogler, A. Kummel, "DOTAP-Folate Liposome Encapsulated Adenovirus Improves the Transfection Efficiency in Various CAR-Deficient Cells"; (full manuscript ready)

C.-H. Huang, N. Mendez, O. H. Echeagaray, J. Weeks, J. Wang, S. Yao, T. Hayashi, S. Blair, N. Gude, W. Trogler, D. Carson, A. Kummel, "Immunostimulatory TLR7-nanoparticles together with checkpoint blockade for effective cancer immunotherapy"; Adv. Therap., 2020, 3 (6), 1900200.

C.-H. Huang, N. Mendez, O. H. Echeagaray, J. Weeks, J. Wang, C. Vallez, N. Gude, W. Trogler, D. Carson, T. Hayashi, A. Kummel, "Conjugation of a Small-Molecule TLR7 Agonist to Silica Nanoshells Enhances Adjuvant Activity"; ACS AMI, 2019, 11 (30), 26637-26647.

C.-H. Huang, J. Wang, J. Yang, J. P. Oviedo, S. Nam, W. Trogler, S. Blair, M. Kim, A. Kummel, "Thickness and Sphericity Control of Hollow Hard Silica Shells through Iron (III) Doping: Low Threshold Ultrasound Contrast Agents"; Adv. Funct. Mater., 2019. 29 (33), 1900893.

A. G. Badaracco, E. Ward, C. Barback, J. Yang, J. Wang, C.-H. Huang, et al. "Indocyanine Green Modified Silica Shells for Colon Tumor Marking"; Applied Surface Science, 2020, (5):922-3.

J. Wang, C.-H. Huang, O. H. Echeagaray, S. Amirfakhri, S. L. Blair, W. C. Trogler, A. C. Kummel, C. C. Chen. "Microshell Enhanced Acoustic Adjuvants for Immunotherapy in Glioblastoma." Adv. Therap., 2019, (5):922-3.

J. Wang, C.-H. Huang, O. H. Echeagaray, S. Amirfakhri, S. L. Blair, W. C. Trogler, A. C. Kummel, C. C. Chen. "Immuno-stimulatory Effects of Mechanical and Thermal High Intensity of Focused Ultrasound." Neurosurgery, 2019, 212(6),1140-1146.

O. E. Echeagaray-Bredesen, N. Vallez, N. Mendez, C.-H. Huang, et al. "Localized Immune Transcriptional Response to Intratumorally Administrated TLR7 Agonist Conjugates." The FASEB Journal, 2018, 9(2):1719-1727.

FIELD OF STUDY

Major Field: Materials Science and Engineering
Studies in Cancer Nanobiotechnology
Professor Andrew C. Kummel

ABSTRACT OF THE DISSERTATION

Development of Silica Hollow Shells for Ultrasound Imaging and Cancer Immunotherapy

by

Ching-Hsin Huang

Doctor of Philosophy in Materials Science and Engineering

University of California San Diego, 2021

Professor Andrew C. Kummel, Chair

Silica hollow shells have been developed as a convenient drug carrier and ultrasound imaging contrast agent because of their ease of modification and long imaging time. However, as an imaging contrast agent, hard silica shells possess the disadvantages of requiring a relatively high ultrasound insonation power for imaging and low biodegradability due to their structural and chemical stabilities. In order to ameliorate these disadvantages, non-spherical ultrathin silica microshells (with a diameter of 2 μm) doped with iron (III) were synthesized that can be imaged at low insonation power similar to commercial soft microbubble contrast agents and lasted for days. The amount of iron doping provides control over the silica shell thickness and structural morphology, which resulted in a 83% lower insonation power threshold compared to thick counterpart, as well as enhanced biodegradability. Besides using silica microshells to enhance the imaging contrast, nano-sized pure silica shells (NS, with a diameter of 100 nm) was engineered

with a small molecule toll-like receptor 7 (TLR7) agonist, 1V209, to enhance the adjuvant activities *in vitro* and *in vivo*. TLR agonist (TLR7a) and silica NS combination triggered high level of IL-1β release while neither unconjugated TLR7a nor silica shells produced IL-1β. An immunization study demonstrated that silica nanoshell-conjugated TLR7a (NS-TLR7a) increased OVA-specific IgG antibodies a thousand-fold in mice sera and skewed response to a Th1-mediated immunity compared to unconjugated TLR7a. NS-TLR7a were administered intratumorally into mice and silica shells have a tendency to prolong the agonist accumulation time, leading to an increase of the T cell infiltration. When NS-TLR7a was used in combination with checkpoint inhibitors, a higher number of infiltrating lymphocytes were induced and the survival rate was improved compared to checkpoint inhibitors only. In a two-tumor bearing mouse model, the combination therapy (NS-TLR7a+checkpoint inhibitors) showed that not only can the injected tumor be induced into remission, but an uninjected contralateral tumor can also be induced into remission (abscopal effect). The results demonstrated that the NS-TLR7a+checkpoint inhibitors therapy is able to produce a systemic and tumor-specific immune response.

Chapter 1: Thickness and Sphericity Control of Hollow Hard Silica Shells through Iron (III) Doping: Low Threshold Ultrasound Contrast Agents

1.1 Abstract

Silica particles are convenient ultrasound imaging contrast agents because of their long imaging time and ease of modification; however, they require a relatively high insonation power for imaging and have low biodegradability. In this study, 2 μm ultrathin asymmetric hollow silica particles doped with iron (III) (Fe(III)-SiO_2) are synthesized to produce biodegradable hard shelled particles with a low acoustic power threshold comparable with commercial soft microbubble contrast agents (Definity) yet with much longer *in vivo* ultrasound imaging time. Furthermore, high intensity focused ultrasound ablation enhancement with these particles shows a 2.5-fold higher temperature elevation than with Definity at the same applied power. The low power visualization improves utilization of the silica shells as an adjuvant in localized immunotherapy. The data are consistent with asymmetric engineering of hard particle properties that improve functionality of hard versus soft particles.

1.2 Introduction

Ultrasound contrast agents are used to enhance image contrast and improve diagnostic and therapeutic functionality for drug delivery, tumor detection-characterization, and image-guided surgeries.[1,2,3,4] Among ultrasound contrast agents, microbubbles encapsulated by surfactants, lipids, and polymers are the most common. [5,6,7] However, conventional microbubbles and other soft-shelled structures suffer from rapid clearance from the injection site, short *in vivo* imaging lifetimes, large bubble size variance, and complex surface modification procedures.[8,9,10] Therefore, hard particles made with silica are being studied as alternative contrast agents for ultrasound imaging because of their long shelf life, persistent imaging properties, high thermal stability,

chemical stability, and low toxicity. [11,12,13]

In addition to ultrasound image contrast enhancement, several contrast agents have been reported to augment high intensity focused ultrasound (HIFU) therapy. HIFU therapy induces tissue necrosis through energy conversion of ultrasound energy to regional hyperthermia, and it has gained interest for tumor ablation applications. [14] Microbubbles enhance tumor ablation during HIFU therapy; [15,16,17] however, the short in vivo lifetime of their soft shells limits this application. Hard silica shells are long lived in tissue and even under insonation and, therefore, may offer better potential as HIFU therapy enhancers. [18,19]

Despite the advantages, rigid silica shells still require higher insonation power to fracture, which releases gas in situ and produces signal contrast comparable to soft shell particles. Since insonation energy deposited in tissue significantly attenuates with increasing penetration depth, for deeper tissue imaging, low power threshold imaging for hard silica shells is still required. Liberman et al. demonstrated that substitution of a fraction of the initial silica shell precursors with organically modified silanes produced thinner nanoshells. These thinner shells decreased ultrasound mechanical index (MI) imaging thresholds compared to the control nanoshells synthesized with only tetramethyl orthosilicates (TMOSs). [20]

In the present study, it is shown that in addition to substitution of the initial silica precursor with phenyl precursors, [20] the iron doping further alters the shell thickness and structural morphology. With 3.5% iron doping (corresponding to 0.010% w/v), 2 μm ultrathin iron (III) doped particles with irregular particle subpopulations were synthesized and demonstrated a 83% lower threshold for ultrasound imaging than non-iron doped particles. The power threshold of these asymmetric 2 μm ultrathin iron (III) doped silica hard particles is similar to that of soft shell commercial particles, which have much shorter imaging lifetimes.[10] The 2 μm ultrathin Fe(III)-

SiO_2 shells also exhibited a larger temperature rise during HIFU insonation compared to thicker shells or commercial microbubbles. These new ultrathin asymmetric Fe(III)-SiO_2 shells have the ability to amplify the immune response and potentially to be utilized as an adjuvant in localized immunotherapy which can be readily visualized by ultrasound imaging. In vitro cytokines analysis for the asymmetric 2 μm ultrathin silica shells in contact with RAW264.7 macrophages plus lipopolysaccharide (LPS), demonstrated a 40-fold increase in interleukin 1β (IL-1β) production com- pared to RAW264.7 macrophages plus LPS alone. The imaging, HIFU, and immune response results showed that engineering asymmetry opens a new dimension for tuning the properties of ultrasound active nanoparticles.

1.3 Methods

1.3.1. Materials

TMOS, trimethyloxyphenylsilane (TMPS), and N1-(3-trimethoxysilylpropyl) diethylenetriamine (DETA) were purchased from Sigma-Aldrich (St. Louis, MO) and the polystyrene beads were purchased from PolySciences Inc. (Warrington, PA). Iron (III) ethoxide was purchased from Gelest Inc. (Moorisville, PA). Heat inactivated human serum was purchased from Gemini Bio-Products Inc (West Sacamento, CA). Ultrasound images were acquired with use of a Seimens Sequoia 512 (Mountainview, CA), and an Acuson 15L8 imaging transducer. The H-102 single element transducer used in HIFU experiments was acquired from Sonic Concepts Inc (Bothell, WA). Software programs used for data analysis include Matlab (Natick, MA), ImageJ, Microsoft Excel (Redomond, WA), GraphPad Prism (La Jolla, CA), and OsiriX (Bernex, Switzerland).

1.3.2. Synthesis of Silica Shells

A 0.2% DETA solution was prepared in ethanol solvent and vortexed slightly to mix.

Subsequently, 100 mL of ethanol, 8 mL of 0.2% DETA solution, and 5 mL of 2 μm polystyrene beads were vortex-mixed for an hour to produce cationic polystyrene beads. 270 μL of TMOS was added and vortex mixed for an additional 7.5 h to generate robust non-iron (III) doped 2 μm silica shells. Trimethoxyboron was also added to the sol gel synthesis to enhance the shell structure as previously described.[21] To generate thinner shells, the silica precursor amount was reduced to 70 mol% using a TMOS/TMPS mixture (1:1 molar ratio). The silica precursor solution was added into the cationic beads reaction mixture and mixed for an additional 5 h. This reduced amount of silica precursor did not allow shell formation after calcination. However, by incorporating iron (III) into the silica network to strengthen the shells, an intact thin shell structure was obtained. The detailed synthesis process is as follows for four iron (III) doping levels. 1,000, 750, 500, or 250 μL of the 20 mg/mL iron (III) ethoxide solution were added into the DETA/polystyrene beads mixture together with the silica precursor solution, and vortex mixed for 5 h, to produce iron (III) doped silica shells. Brown core–shell Fe(III)-SiO_2 particles were collected by centrifugation at 3500 rpm for 5 mins, and washed twice with 15 mL of ethanol. The core–shell particles were calcined in air in a muffle furnace, starting from room temperature and heating at 1.5 °C per minute to 550 °C to yield ≈20 mg of the rigid hollow particles.

Step (1): DETA was added into polystyrene beads mixture in ethanol to assist templating reaction

$$(C_8H_8)n + (CH_3O)_3\,Si(CH_2)_3NHCH_2CH_2NHCH_2CH_2NH_2 \rightarrow (C_8H_8)n \cdot (CH_3O)_3\,Si(CH_2)_3NHCH_2CH_2NHCH_2CH_2NH_2 \text{.....physisorption} \quad (1)$$

Step (2): TMOS, TMPS, and iron (III) ethoxide were added into polyamine-modified polystyrene beads mixture. TMOS and TMPS reacted with H_2O presented in the solution and started hydrolysis and iron (III) was incorporated into silica network, cationic protonated DETA

helped attract anionic deprotonated sol hydrolysis products for templating on the polystyrene bead surface

$$Si(OR)_4 + H_2O \rightarrow HO{-}Si(OR)_3 + R{-}OH \quad (2)$$

Step (3): Spin down the iron(III)/silica-polystyrene core–shells. Calcine and obtain hollow iron (III) doped silica shells.

The 70 mol% of TMOS/TMPS mixture was a previously determined to be the optimized silica precursor concentration to generate thin silica shells. It was observed that a lower amount of initial silica precursor concentration, even with addition of iron ethoxide to strength the shells or with addition of increased DETA to attract more silicic acid to the polystyrene bead template surface, would fail to robustly generate intact shell.

1.3.3. Characterization of Particles

The iron (III) doped silica shell particles were imaged in a JEOL 2100F Transmission electron microscope (TEM) operating at 200 kV. TEM samples were prepared by drop-casting the shells (diluted in ethanol) on lacey carbon coated copper TEM grids. Energy filtered imaging TEM through a Gatan imaging filter (Tridiem) was used to investigate the elemental distribution in the sample. In addition, the shell thickness was measured from high-magnification TEM images in ImageJ software.

1.3.4. Biodegradability

Iron (III) doped or non-iron (III) doped 2 μm silica shells were dispersed at 1 mg/mL concentration in heat inactivated human serum. The samples were vortex mixed to suspend the particles and incubated at 37 °C in a temperature-controlled water bath. The samples were vortexed every 24 h. The human serum was replaced with fresh human serum every 4 d after centrifugation and samples were vortexed to resuspend the shells. Every 8 d, a pellet was isolated by

centrifugation, washed twice with water, and calcined. scanning electron microscopy (SEM) images and energy-dispersive X-ray spectroscopy (EDX) analysis of the pellet at each time point were obtained to characterize the extent of biodegradation.

1.3.5. Ultrasound Contrast Pulse Sequencing and Color Doppler Imaging

The 2 μm shells were suspended in 1 mL of water at a concentration of 0.4 mg/mL in a pipette bulb. Microbubbles (Definity) with gas volumes equivalent to the shells were filled in a pipette bulb tube. The bulb was placed in a water bath with an ultrasound transducer placed perpendicularly. Ultrasound was applied at 7 MHz for both contrast pulse sequencing (CPS) imaging and color Doppler imaging from low to high insonation power, which is referred to as the MI values in the study.

1.3.6. High Intensity Focused Ultrasound

100 μL of 4 mg/mL PFP-filled Fe(III)-SiO_2 shell/water suspension was mixed with 900 μL of water in a pipette bulb. Definity microbubbles at the same gas volume as occupied by the silica microshells were used for comparison. The bulb was placed in the focal region of the HIFU transducer. HIFU power of 100 W was applied at a 100% duty cycle for 10 s. The temperature rise for each sample was measured with a thermocouple.

1.3.7. In Vitro Studies

RAW264.7 cells (mouse macrophage cell line) were purchased from the American Type Culture Collection (Rockville, MD) and cultured in complete Dulbecco's modified Eagle's medium (DMEM) media (Gibco, Carlsbad, CA). Cells were plated at a concentration of 10^4 cells/well and primed with lipopolysaccharide at 100 ng/mL for 2 h before exposure to silica shells. IL-1β in the supernatant after 18 h incubation was measured by enzyme-linked immunosorbent assay (ELISA) kit (Cat. No. DY401, R&D system, Minneapolis, MN).

1.3.8. In Vivo Studies

The C57BL/6 mice were purchased from the Jackson Laboratory (Bar Harbor, ME). 50 μL of 4 mg/mL shell/water suspension was intramuscularly injected into the flank of each mouse. Color Doppler images were acquired continuously as the MI was increased from 0.06 to the maximum clinically allowable MI of 1.9. The threshold is defined as the first signal generated in the color Doppler images as the MI is increased. For the signal persistence study, the images were taken daily at MI = 1.9 for 10 d. All animal procedures have been approved by the Institutional Animal Care and Use Committee (IACUC) at University of California San Diego (UCSD).

1.4 Results and discussion

1.4.1. Iron (III) Doping Modulates Shell Thickness

Iron (III) doped silica shells with a diameter of 2 μm were synthesized with varying iron (III) doping concentrations (Table 1.1). TEM and scanning electron microscopy SEM images in Figure 1.1 show that the 2 μm iron doped silica shells (0.010%, 0.015%, and 0.020% of iron (III) ethoxide-concentrations are shown in weight/volume percentages) formed intact spherical structures. When iron (III) doping was reduced less than 0.010%, shell synthesis was not viable.

Based on EDX analysis in Table 2.1, 0.01%, 0.015%, and 0.02% of $Fe(OEt)_3$ doping percent yielded 3.5 ± 1.0, 5.7 ± 1.7, and 6.8 ± 2.9 Fe (III) atomic % in final products, respectively.

The effect of iron (III) content on shell thickness and structure were quantified using TEM and imageJ software. Thickness was defined as the dense layer of the shells as previously described.[20] Figure 1.1 and Table 1.1 validated that iron (III) content controls shell thickness for a given silica precursor. The failure of shell formation with 0.005% iron (III) doping is consistent with insufficient iron (III) needed for shell strengthening. The formulations synthesized with 0.01% of iron (III) ethoxide have a markedly thinner shell thickness when compared to

formulations with a higher iron (III) content, and thus were denoted as 2 μm ultrathin Fe(III)-SiO_2 shells (2.7 nm vs 21.1 nm thickness, respectively). Particles with 0.01% of iron (III) ethoxide will be referred to as ultrathin, particles with 0.015% of iron (III) ethoxide will be referred to as medium thickness, and particles with 0.02% of iron (III) ethoxide will be referred to as thick shell particles.

Table 1. 1: The starting concentration of iron precursor of Fe-SiO_2 shells and the final Fe atomic % and shell thickness.

Iron ethoxide Starting Concentration (% in w/v)	Fe atomic % (by EDX)	Shell thickness (nm)	Sample
0.020%	6.8 ± 2.9	21.1 ± 5.6	Thick shells
0.015%	5.7 ± 1.7	6.2 ± 2.3	Medium-thickness shells
0.010%	3.5 ± 1.0	2.7 ± 1.5	Ultrathin shells
0.005%	1.1 ± 0.5	--	--

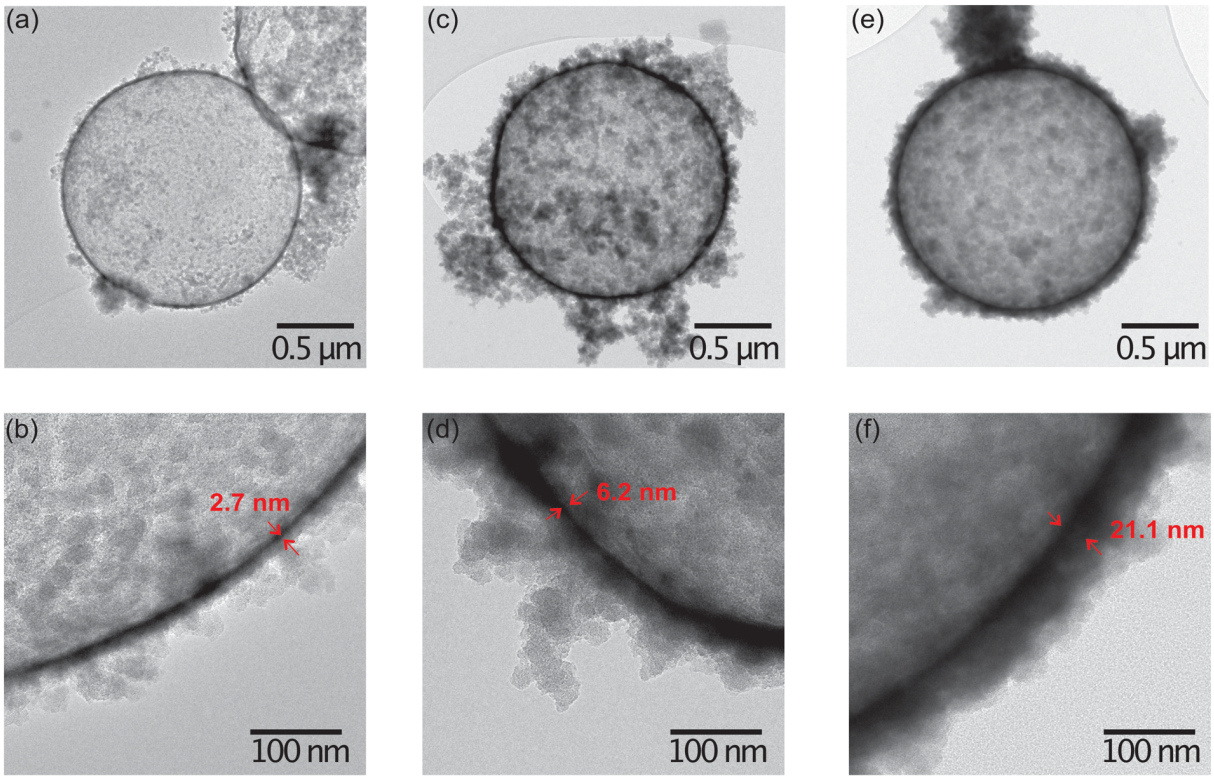

Figure 1. 1: TEM images of iron (III) doped silica hollow shells.
(a,b) ultrathin, (c,d) medium-thickness, and (e,f) thick iron (III) doped silica shells.

1.4.2. Irregular Shells Formed by Low Iron (III) Doping

A correlation between iron (III) doping and particle sphericity was observed after examining more than 100 randomly obtained microscopy images for each sample. While only a 1.7% ± 1.7% irregular particle subpopulation was found in the medium-thickness Fe(III)-SiO_2 shells (0.015% w/v formula), a 26% ± 3% irregular particle subpopulation was observed in the ultrathin Fe(III)-SiO_2 shells. Irregular particles were not observed for either high iron (III) doped silica shells (0.020% w/v formula) nor non-iron (III) doped silica shells (Figure 1.2). Since iron (III) doping lower than 0.005% w/v could not produce an intact sphere structure under the synthetic conditions, 0.010% w/v of iron (III) doping was the optimal concentration for obtaining a significant fraction of irregular shells.

Previous studies show that a particle's shape is a critical factor in mechanical strength, and that the structural heterogenicity of the irregular particles can cause discrete local stresses.[21,22,23] For the 26% irregularly shaped subpopulation in the ultrathin particles, it is expected they will exhibit lower shell strength, fracture more easily, and, therefore, enhance the ultrasound imaging performance at lower insonation powers. Among the ultrathin Fe(III)-SiO_2 particles, nanoscale deep surface inclusions were also found in some particles, which implies that there may be more structural defects in the ultrathin shells that are not visible in TEM.

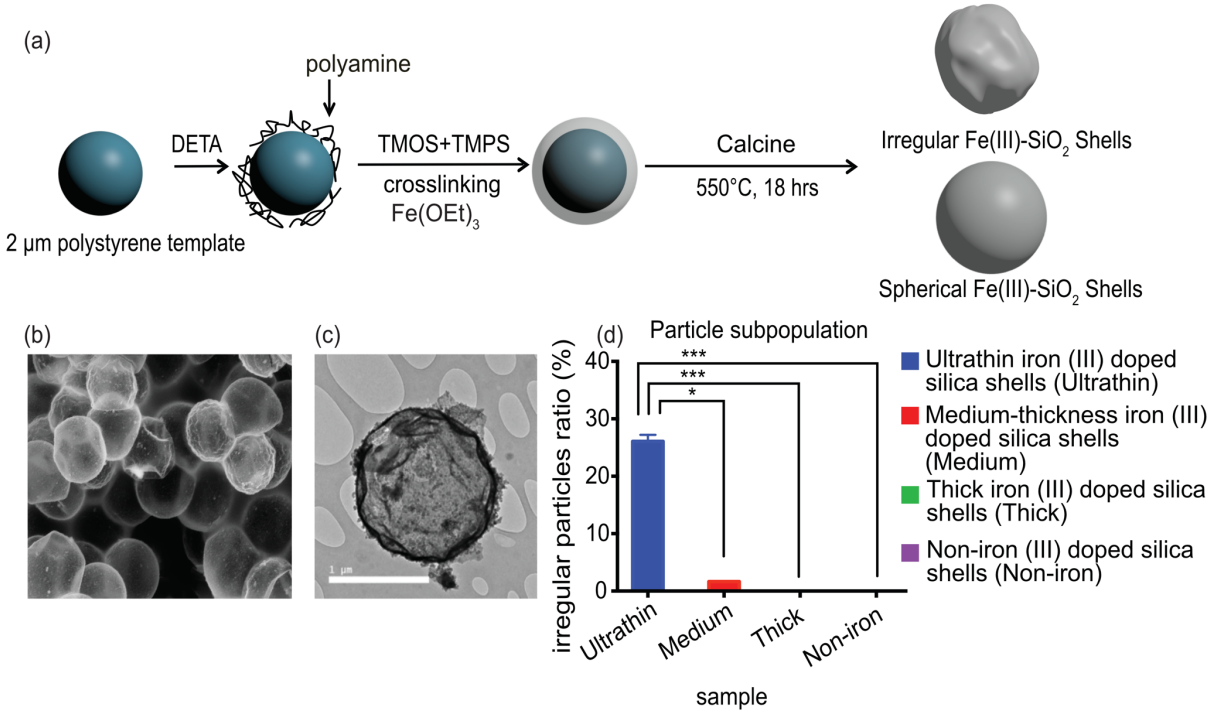

Figure 1. 2: Irregular particle subpopulation from ultrathin iron (III) doped silica shells. (a) Synthesis of ultrathin shells with a large subpopulation of irregular shells. (b) Representative SEM image of 2 μm Fe(III)-SiO_2 ultrathin shells containing spherical and irregular particle subpopulations. (c) Representative TEM image of single irregular 2 μm Fe(III)-SiO_2 ultrathin shell. d) Irregular particle ratios in ultrathin Fe(III)-SiO_2 particles, medium- thickness Fe(III)-SiO_2 particles, thick Fe(III)-SiO_2 particles and non-iron (III) doped SiO_2 particles (Data were analyzed for fraction of irregular using Kruskal–Wallis test. P-values are as follows: *$P \leq 0.05$, **$P \leq 0.01$, ***$P \leq 0.001$).

1.4.3. Low Ultrasound Imaging Threshold for New Ultrathin Fe(III)-SiO_2 Shells

To verify that sphericity and shell thickness of iron (III) doped silica shells control ultrasound performance, shells were filled with perfluoropentane (PFP) gas and imaged with ultrasonography. The ultrasound sensitivity of the particles was quantified using CPS; CPS extracts nonlinear signals to produce images,[22] and the CPS signals correspond to echo decorrelation events. According to the CPS, 2 μm diameter thick and ultrathin shells began generating signals at MI = 0.66 and MI = 0.11, respectively. The average intensity of pixels in CPS images was referred to brightness in this study. When the MI started at 0.06, the signal was due to background noise which was ≈50 a.u. (Figure 1.3a–c). As the MI increased, the intensity of pixels

in CPS images increased far above the background noise. As shown in Figure 1.3a, the 2 μm ultrathin shells demonstrated a much lower power insonation threshold for CPS brightness (at frame 55; MI = 0.11) than the thick shells (at frame 150; MI = 0.66). The differences in brightness profiles are attributed to the thick shells providing a more robust structure so that there are fewer shells fractured at low MI. In Figure 1.3a, as the MI was increased, the ultrathin shells generated two plateaus at MI = 0.9 and 1.9. For the first plateau, it was hypothesized that the ultrasound waves at low insonation power (MI = 0.2–0.9) interacted with the irregular shells that have a weaker structure, breaking the irregular shells to release gas and create more non- linear events. It was hypothesized that the second plateau represents the 2 μm ultrathin shells with a normal spherical structure fracturing to release PFP gas at higher insonation powers and enhancing the output ultrasound signals (MI = 1.0–1.9). The effect of shell thickness on threshold power for CPS was quantified using a new metric.

The threshold for CPS brightness was defined as 20% of the maximum brightness at MI = 1.9. The power threshold of ultrathin, medium-thickness, and thick shells occurred at MIs of 0.2, 1.0, and 0.97, respectively (Figure 1.3d). By reducing the iron (III) doping and reducing corresponding shell thickness and symmetry, the threshold of CPS imaging of ultrathin shells decreased by 83% (p-value = 3.00×10^{-5}) compared to the thick symmetric non-iron (III) doped shells.

A commercial contrast agent (Definity) was used for com- paring the ultrasound performance of fluorocarbon-filled soft shells with the PFP-filled ultrathin Fe(III)-SiO_2 hard shells. Definity is a clinically used microbubble emulsion filled with octafluoropropane gas that has an extremely low CPS threshold, but at the same time it has a large size distribution and short imaging lifetime; in vivo studies showed that microbubbles can only be imaged for few minutes.[23]

Definity was tested at equivalent gas volume concentration as silica shells. The ultrathin iron (III) doped hard shells and commercial microbubbles have no difference in imaging thresholds (p-value = 0.88) and both demonstrated low threshold mean (MI = 0.20 and 0.16, respectively) as shown in Figure 1.3d. These results indicate the feasibility of microbubble alternative by rigid ultrathin iron (III) doped silica shells that provide a longer imaging usage time.

Similar to CPS imaging, the enhancement of color Doppler imaging by PFP-filled Fe(III)-SiO_2 hard shells were tested in vitro. Appearance of the first signal of the color Doppler image is presented in Figure 1.3e. Consistent with the CPS results, the ultrathin asymmetric shells showed a lower threshold com- pared to thick shells. Signals from the 2 μm ultrathin shells and microbubbles (Definity) both appeared at MI = 0.2 with similar signals, while that of the thick shells first appeared at MI = 1.1. At modest insonation power (MI = 0.4–1.1), ultrathin and medium thickness iron (III) doped shells showed a much stronger signal compared to Definity (Figure 1.3f,g).

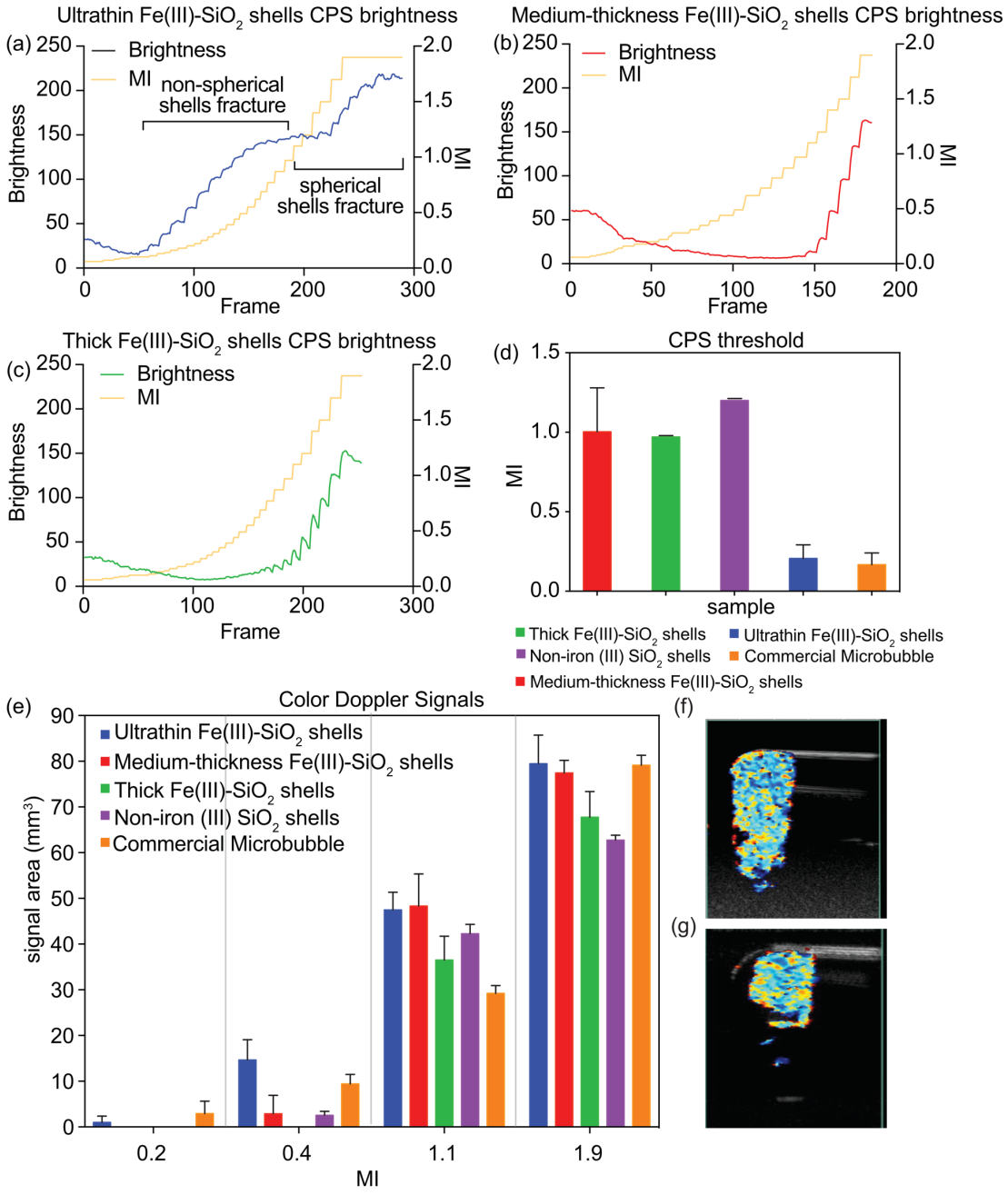

Figure 1. 3: CPS and color Doppler ultrasound imaging of PFP-filled iron (III) doped silica shells, non-iron (III) doped silica shells and microbubbles.
(a–c) CPS brightness of iron (III) doped silica shells over frames from MI = 0.06 to MI = 1.9. (a) Ultrathin Fe(III)-SiO_2 2 µm shells, b) medium-thickness Fe(III)-SiO_2 2 µm shells, and (c) thick Fe(III)-SiO_2 2 µm shells. (d) CPS thresholds of non-iron (III) doped 2 µm silica shells, commercial microbubbles (Definity), and thick, medium-thickness, and ultrathin Fe(III)-SiO_2 shells. (e) Color Doppler imaging of 2 µm shells with thick, medium-thick, ultrathin thickness, compared to non-iron (III) doped shells and microbubbles (Definity). (f) Image of color Doppler ultrasound of ultrathin Fe(III)-SiO_2 shells at MI = 1.9. (g) Image of color Doppler ultrasound of thick Fe(III)-SiO_2 shells at MI = 1.9.

1.4.4. HIFU Enhancement by Ultrathin Fe(III)-SiO_2 Shells

Several commercial microbubble contrast agents such as Levovist, Optison, and Definity have been studied to enhance HIFU treatment.[24,25] In the present study, the enhancement of HIFU by particles was characterized in vitro by comparing the temperature rise of a solution of silica shells, commercial microbubbles with same gas volume, and pure water. In Figure 1.4, ultrathin Fe(III)-SiO_2 shells demonstrated a 33.4 °C temperature rise from 23.1 to 56.5 °C after applying 100 W 100% duty cycle HIFU for 10 s. Conversely, thick and medium thickness Fe(III)-SiO_2 shells only increased the temperature by ≈15.2 °C from 23.6 to 38.8 °C, and 17.0 °C from 23.4 to 40.4 °C, respectively. In water without added particles, the temperature only increased by 8.3 °C under HIFU exposure, which is approximately a quarter of temperature rise obtained by the ultrathin Fe(III)-SiO_2 shells. At the same applied HIFU power and the same gas volume concentration, commercial microbubbles (Definity) produced only 13.6 °C of temperature rise (from 20.5 to 34.1 °C). This is a 2.5-fold smaller temperature rise compared to ultrathin Fe(III)-SiO_2 hard shells. The data con- firms and quantifies the HIFU enhancement effects achieved by the ultrathin hard microshells ultrasound contrast agent.

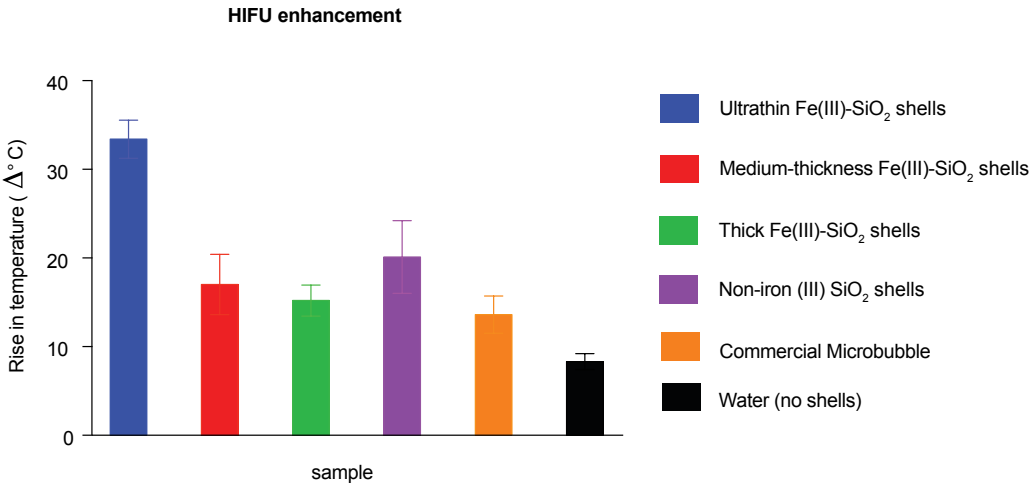

Figure 1. 4: HIFU response of iron (III) doped silica shells, non-iron (III) doped silica shells, commercial microbubbles, and absence of shells (pure water).
0.4 mg/mL silica shells or Definity microbubbles at the same gas volume were applied HIFU (100 Watts) at 100% duty cycle for 10 s.

1.4.5. Biodegradability

Pohaku-Mitchell et al. demonstrated that by doping iron (III) into nanometer-sized silica shells at 6 at% Fe, the silica particles became biodegradable through an iron (III)-chelating pathway via transferrin after 17 d incubation with human serum.[26] To test the in vitro biodegradability of the new ultrathin shells, 2 μm non-iron (III) doped silica shells, thick Fe(III)-SiO_2 shells (6.8 at% Fe), and ultrathin Fe(III)-SiO_2 shells (3.5 at% Fe) were immersed in human serum for 24 d. The morphology of the silica shells was monitored to determine the progress of biodegradation. On the 8th day, both ultrathin and thick Fe(III)-SiO_2 shells began merging into irregular solid clusters while the nanosized Fe(III)-SiO_2 particles remained mostly intact on day 10 in previous studies.[26] On day 24, ultrathin Fe(III)-SiO_2 samples pre-dominantly disappeared, whereas thick Fe(III)-SiO_2 samples remained partially intact. The non-iron (III) doped silica shells remained mainly intact in serum over the course of 24 d. It is hypothesized that thinner shells are easier to degrade despite the decreased amount of iron (III) doping. Only 3.5 at% of iron (III) doping is sufficient to convert nonbiodegradable silica matrix to biodegradable shells while in the literature 6% of iron (III) doping gave a much slower biodegradation profile due to the much thicker shells.[26]

1.4.6. In Vivo Imaging Threshold and Persistence of Fe(III)-SiO_2 Shells

The iron (III) doped silica shells were tested for use as an intraoperative, low threshold color Doppler tissue marker in vivo. Imaging was performed at 7 MHz, the previously determined optimal frequency. 0.4 mg of ultrathin or thick Fe(III)-SiO_2 shell solutions were intramuscularly injected into mice, and insonation power was increased from MI = 0.06 to MI = 1.9. The color Doppler signal was monitored over different insonation powers to assess the in vivo imaging enhancement by the 2 μm shells. Figure 1.5a shows that thick shells began to show the first signal

at MI = 1.1 and persisted to MI = 1.9, yet the signals remained faint throughout the MI range. In contrast, ultrathin shells produced the first signal at MI = 0.37; a threshold value over 3× lower than that of the thicker shells. As the MI increased, the color Doppler signals became stronger until MI = 1.9, by which point the signal sur- passed that of thicker shells. With the improved performance of in vivo color Doppler imaging and HIFU enhancement, these new ultrathin asymmetric iron (III) doped silica hard shells offer added safety in applications of image-guided HIFU tumor ablation, by providing HIFU enhancement at reduced power levels.

To explore the potential utilization as long-term ultrasound biomarkers, these ultrathin asymmetric Fe(III)-SiO_2 shells were injected into mice flanks and imaged over 10 d at MI = 1.9 to assess the signal persistence. The commercially available microbubbles Definity could only be imaged within a few minutes after injection on the first day as reported previously. The color Doppler of Definity could not be detected after 1 d. Conversely, the gas filled ultrathin 2 μm Fe(III)-SiO_2 shells could be detected for 10 d in vivo after the initial injection. The results shown in Figure 1.5b also indicated that the 2 μm ultrathin Fe(III)-SiO_2 shells remained stationary at the injected tissue and did not excavate from the injected tissue site. The in vivo imaging stability and the long retention time at the injection site suggested the promising application for these ultrathin asymmetric shells to be used as tissue labeling agents.

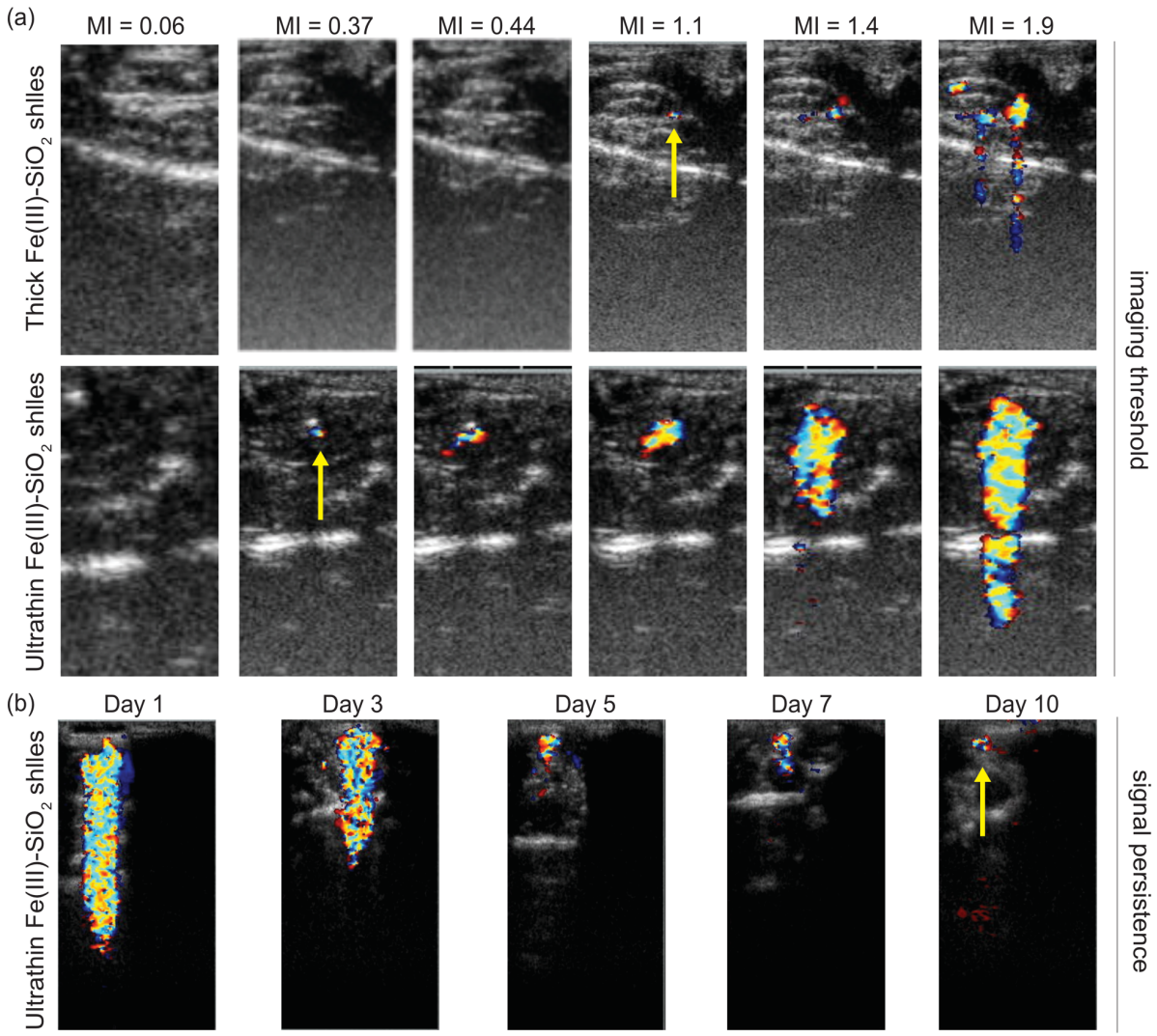

Figure 1. 5: In vivo color Doppler ultrasound images of 2 µm Fe(III)-SiO_2 shells filled with PFP gas.
(a) Thresholds of thick Fe(III)-SiO_2 shells and ultrathin Fe(III)-SiO_2 shells. Shells were injected into mice intramuscularly and imaged with MIs from 0.06 to 1.9. (b) Signal persistence of ultrathin Fe(III)-SiO_2 shells. Shells were injected into mice intramuscularly and imaged over the course of 10 d at MI = 1.9.

1.4.7. 2 µm Ultrathin Fe(III)-SiO_2 Shells Can Be Used as an Immune Adjuvant

The aforementioned advantages for these new ultrathin asymmetric Fe(III)-SiO_2 shells, such as prolonged persistency and easy visualization, are important in promoting a mature immune response and designing immunotherapy strategies, respectively.[27] Since silica nanoparticles have been previously reported to be a strong immune adjuvant that amplify antibody production and

elicit immunological protection response,[28] it is hypothesized that these new Fe(III)-SiO_2 2 μm shells can also effectively activate immune response while being able to generate stable ultrasound signals for tracking the adjuvant location. To test their adjuvanticity, innate immune cells, macrophages RAW264.7, primed with LPS were incubated with shells and IL-1β in the supernatant was measured by ELISA to assess the activation level of macrophages. IL-1β is able to enhance dendritic cells activation and T cells priming, stimulating an effective adaptive immune response.[29] As shown in Figure 1.6, these new ultrathin asymmetric Fe(III)-SiO_2 shells induced a 40-fold increase in IL-1β in cells primed with LPS compared to LPS alone. This result suggests that these new Fe(III)-SiO_2 shells have the ability to amplify the immunity, indicating the potential to be utilized as an adjuvant in immunotherapy with medical imaging capabilities.[30]

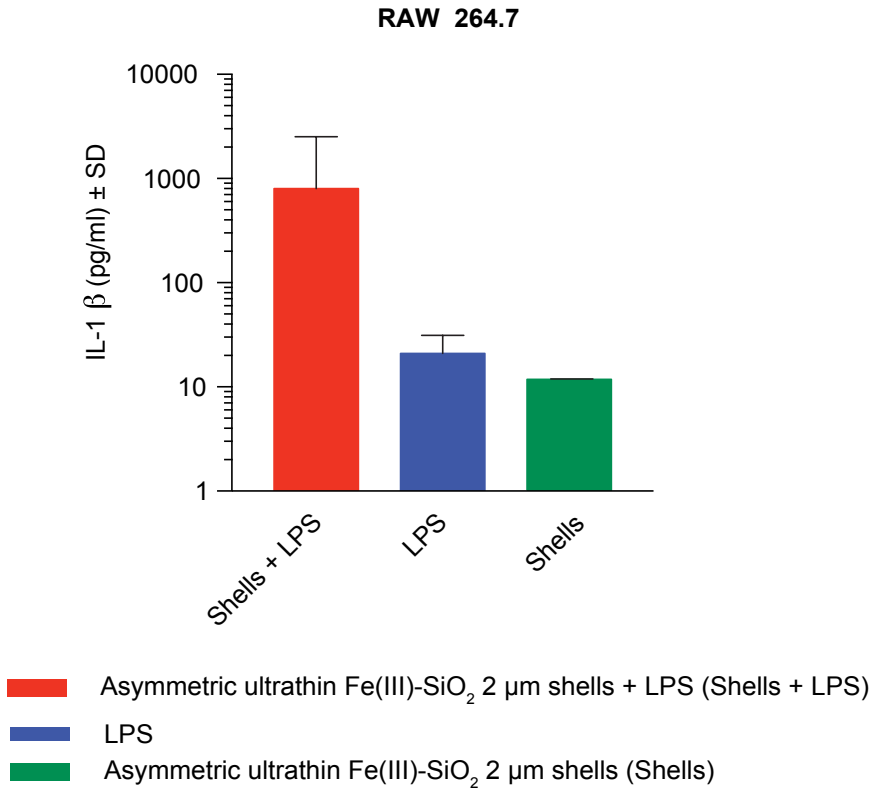

Figure 1. 6: In vitro adjuvanticity of ultrathin asymmetric Fe(III)-SiO_2 shells.
10^4 cells per well of RAW264.7 were incubated with iron (III) doped silica shells and/or LPS to determine the adjuvanticity of these new ultrathin asymmetric Fe(III)-SiO_2 shells.

1.5 Conclusion

The extent of iron (III) doping can be used to modify the thickness and structural morphology of silica shells. The low iron (III) doping (0.010% w/v) not only generated thinner shells but also produced a 26% irregular particle subpopulation among the ultrathin hard shells. These new asymmetric ultrathin Fe(III)-SiO_2 hard shells demonstrated similar performance to the commercial soft particle contrast agent, Definity, which suffers from short imaging duration. HIFU sensitization tests showed that asymmetric ultrathin 2 μm Fe(III)-SiO_2 shells induced a greater HIFU response compared to symmetric thicker shells and microbubbles. The persistency experiments demonstrated that these new Fe(III)-SiO_2 shells can be imaged in vivo for a much longer time compared to commercial microbubbles. The enhanced performance of these new Fe(III)-SiO_2 shells originates from two structural variances; the thinner shells and the irregular particles are mechanically weaker. It has been demonstrated that a new variable, asymmetry, may be introduced into hard shelled contrast agents in order to tune their structural integrity. A more fragile structure may expand their applications; for example, these new ultrathin asymmetric Fe(III)-SiO_2 shells capable of amplifying immune response can be used as a local immunotherapy with effective ultrasound visualization.

1.6 Acknowledgement

Chapter 1, in full, is a reprint of the material as it appears in Advanced Functional Materials 2019. Huang, Ching-Hsin; Wang James; Yang, Jian; Oviedo, Juan Pablo; Nam, Seungjin; Trogler, William C.; Blair, Sarah L.; Kim, Moon J.; Kummel, Andrew C., Wiley, 2019. The dissertation author was the primary author of this paper.

Chapter 2: Conjugation of a Small-Molecule TLR7 Agonist to Silica Nanoshells Enhances Adjuvant Activity

2.1 Abstract

Stimulation of Toll-like receptors (TLRs) and/or NOD-like receptors on immune cells initiates and directs immune responses that are essential for vaccine adjuvants. The small-molecule TLR7 agonist (TLR7a), imiquimod, has been approved by the US Food and Drug Administration (FDA) as an immune response modifier but is limited to topical application due to its poor pharmacokinetics that causes undesired adverse effects. Nanoparticles are increasingly used with innate immune stimulators to mitigate side effects and enhance adjuvant efficacy. In this study, a potent small-molecule TLR7a, 2- methoxyethoxy-8-oxo-9-(4-carboxybenzyl)adenine (1V209), was conjugated to hollow silica nanoshells (NS). Proinflammatory cytokine (IL-6, IL-12) release by mouse bone-marrow-derived dendritic cells and human peripheral blood mononuclear cells revealed that the potency of silica nanoshells-TLR7 conjugates (NS-TLR7a) depends on nanoshell size and ligand coating density. Silica nanoshells of 100 nm diameter coated with a minimum of ~6,000 1V209 ligands/particle displayed 3-fold higher potency with no observed cytotoxicity when compared to an unconjugated TLR7a. NS-TLR7a activated the TLR7-signaling pathway, triggered caspase activity, and stimulated IL-1β release, while neither unconjugated TLR7a nor NS alone produced IL-1β. An in vivo murine immunization study, using the model antigen ovalbumin, demonstrated that NS-TLR7a increased antigen-specific IgG antibody induction by 1,000× with a Th1-biased immune response, compared to unconjugated TLR7a. The results show that the TLR7 ligand conjugated to silica nanoshells is capable of activating an inflammasome pathway to enhance both innate immune-stimulatory and adjuvant potencies of the TLR7a, thereby broadening applications of innate immune stimulators.

2.2 Introduction

Nanoparticle technology has shown potential to improve immunotherapy. With tailored properties such as size, structure, surface chemistry, and drug-loading capacity, nanoparticles can increase the therapeutic index of immunostimulatory agents by facilitating entry into antigen-presenting cells (APCs)[31,32,33] and promoting local retention in the tissue.[34,35] The prolonged retention time can sustain a higher localized agent concentration that amplifies the immune response. Employing nanoparticles in addition to immunostimulatory agents can also enhance and shape the immune responses toward a cellular- or humoral-biased immunity.[36,37,38] Cellular immunity that is mediated by T helper 1 cells (Th1) correlates to the induction of cytotoxic T cells to fight cancerous cells; humoral immunity that is mediated by T helper 2 cells (Th2) supports B cell proliferation to fight extracellular organisms.[39] Pattern recognition receptors (PRRs), such as Toll-like receptors (TLRs) and NOD-like receptors (NLRs), can activate the immune system and are commonly targeted when designing immunostimulatory agents.[40] TLR7 is one of the most extensively characterized TLRs for drug targeting.[41,42] For example, imidazoquinoline compounds produce proinflammatory cytokines, which display antitumoral and antiviral activities and are being investigated as cancer treatments.[43] NLRs, the other common target, including subfamily members such as NLRP1, NLRP3, and NLRP4, are important factors in the activation of caspase-1 in response to proinflammatory stimuli.[44] Despite promising specificity, these immunostimulatory agents exhibit insufficient immune response induction due to poor pharmacokinetics (PK) and thus require better formulation, such as conjugation to nanoparticles, to improve efficacy.[38,45]

Silica nanoparticles have several advantages for immuno-therapy, which include the ease of surface conjugation to a variety of immune-stimulants[46] and self-adjuvanticity. While other

nanoparticles, such as polymers and lipids, have also been developed,[47,48] they have some limitations. Liposomes can improve PK;[49] however, their thermodynamic instability restrains their widespread use in a practical therapeutic setting.[50] Cholesterol insertion and PEGylation are used to improve liposome stability but may lead to decreased immune responses[51,52,53,54] or accelerated blood clearance,[55] respectively. Polymeric nanoparticles, commonly made of polylactic acid and polylactic-co-glycolic acid, are mostly compatible with soluble antigens, which are generally weak in immunogenicity and, therefore, may require the addition of commercialized adjuvants.[56] Problems with polydispersity and the requisite sophisticated manufacturing processes have also posed major challenges for reproducing a pharmaceutical-grade polymer-nanoparticle-based immunotherapy agent.[57,58,59] Conversely, silica nanoshells have the advantages of a well-established surface modification chemistry, a narrow size distribution, a highly tunable particle size, high stability in storage, and a high in vivo stability; therefore, they are a promising candidate to deliver immune-stimulants.[60] In addition, the hollow structure has shown to induce a more robust immune response compared to that of solid silica nanoparticles. [61,62] Several silica nanoparticle formulations have been reported to possess the self-adjuvanticity of being able to produce high titers of IgG antibodies comparable to the immune response induced by the commercial adjuvant alum.[63,28,64]

In the present study, immunostimulatory potencies of 100-2,000 nm silica nanoshells conjugated with TLR7 agonists (TLR7a), termed nanoshell-TLR7a conjugates (NS-TLR7a), were investigated. Conjugation of TLR7 agonist (1V209) to 100 nm silica nanoshells at a high surface coating density significantly enhanced the agonistic potency compared to the unconjugated counterpart. Furthermore, silica nanoshells conjugated with TLR7a stimulated IL-1β production through caspase activity, consistent with the silica nanoshells playing a vital role in immune

stimulation. In vivo immunization studies using a model antigen showed that the NS-TLR7a enhanced Th1-biased cellular and humoral immune responses. These results demonstrate that the conjugation of a TLR7a to silica nanoshells amplified the immune-stimulatory effects of the agonist, thereby broadening the potential agonistic application of these agents.

2.3 Experimental

2.3.3 Materials

N1-(3-Trimethoxysilylpropyl)diethylenetriamine (DETA, Cat. No. D93856), TMOS, TMPS, (3-aminopropyl)triethoxysilane (APTES), N-hydroxysuccinimide (NHS, Cat. No. 130672), N-(3- dimethylaminopropyl)-N′-ethylcarbodiimide (EDC), and solvents were purchased from Sigma-Aldrich (St. Louis, MO). Polystyrene templates (100−2,000 nm) were purchased from Polysciences Inc.(Warrington, PA). 4-[6-Amino-2-(2-methoxyethoxy)-8-oxo-7H-purin-9(8H)-yl]methylbenzoic acid (1V209) was synthesized as previously described. Roswell Park Memorial Institute medium 1640 (RPMI, Cat. No. 11875-093, Gibco, Thermo Fisher Scientific, Waltham, MA) was supplemented with 10% fetal bovine serum (Cat. No. 35-011-CV, Corning Inc., Corning, NY), 100 U/mL penicillin, 100 μg/mL streptomycin, and 292 μg/mL glutamine (Cat. No. 10378-016, Life Technologies, Carlsbad, CA) to prepare the complete media (RP-10). Pan-caspase inhibitor, carbobenzoxy-valyl-alanyl-aspartyl-[O-methyl]-fluoromethylketone (Z-VAD-FMK), was purchased from Invivogen (Cat. No. tlrlvad, San Diego, CA).

2.3.4 Instrumentation

TEM images were captured using a JEOL 1400 electron microscope. UV−vis absorption was measured with a NanoDrop ND-100 spectrophotometer (Wilmington, DE) and infinite M200 plate reader (TECAN, Mannedorf, Switzerland).

2.3.5 ELISA Reagents

Mouse anti-IL-6 antibodies (Cat. Nos. 554400 and 554402), mouse anti-IL-12 antibodies (Cat. Nos. 551219 and 554476), and recombinant mouse IL-6 and IL-12 standards (Cat. Nos. 554582 and 554594) were purchased from BD Pharmingen (Franklin Lakes, NJ). Tetramethylbenzidine (TMB) was used as a substrate for HRP. Mouse IL-1β (Cat. No. DY401) and interferon γ (IFN-γ, Cat. No. DY485) ELISA kits were purchased from R&D System (Minneapolis, MN). Chicken ovalbumin (OVA, Cat. No. LS003049) was purchased from Worthington (San Diego, CA) and IgG1-AP goat anti-mouse antibody (Cat. No. 1070-04) and IgG2a-AP goat anti-mouse (Cat. No. 1080-04) antibody were purchased from Southern Biotech (Birmingham, AL). p-Nitrophenyl phosphate tablet (pNPP) was purchased from Sigma-Aldrich (Cat. No. 2700, St. Louis, MO).

2.3.6 Synthesis of 100 nm Nanoshells

0.2% DETA solution was prepared in ethanol and quickly vortexed. Ethanol (430 mL), 40 mL of 0.2% DETA solution, 2.5 mL of water, and 6.25 mL of 100 nm polystyrene beads (2.5% solids (w/v) aqueous suspension) were mixed and stirred for an hour at 4,000 rpm. Polystyrene beads (100 nm) were used as templates for synthesizing silica nanoshells. DETA was physically adsorbed onto polystyrene beads and generated a positive surface charge during initial nucleation of the polycondensation polymerization. Silica precursor was prepared by suspending 375 μL TMOS and 500 μL TMPS in 4 mL of ethanol and briefly vortexed. This precursor solution was added to the polystyrene beads/DETA solution and stirred for 5 h at 4,000 rpm. The TMOS formed silicic acid and its various deprotonated forms, which interacted with positive charges on the surfaces of the beads to propagate polymerization. After 5 h, samples were centrifuged at 3,200 rpm for 25 min and washed twice with ethanol. Samples were left to dry overnight and calcined at

550 °C (ramping at 5 °C/min and soaked at 550 °C for 5 h). The synthesis reaction yields 80−100 mg hollow 100 nm silica nanoshells. Different sizes of hollow silica shells were synthesized with similar methods that were reported in previous studies.[21]

2.3.7 1V209 linking Chemistry and Quantification

1V209 was synthesized as previously described.[65] NHS, EDC, and 1V209 were prepared at 10 mg/mL in anhydrous dimethyl sulfoxide (DMSO). A 1:1:1 molar ratio of NHS, EDC, and 1V209 was mixed and pulse-vortexed for 2 h at 3,200 rpm to form a 1V209 solution (1×). Meanwhile, silica nanoshells were amine-functionalized as follows. The silica nanoshells were suspended in DMSO at 2.5 mg/mL, vortexed, and sonicated until the nanoshells were well suspended. APTES solution (2 μL of 10%) was added per mg of silica and pulse-vortexed for 2 h at 3,200 rpm. After 2 h, nanoshells were centrifuged at 4,000 rpm for 10 min, washed twice with 4 mL of DMSO, and resuspended at 20 mg/mL in anhydrous DMSO. Diluted 1V209/NHS/EDC solution (110 μL, 0.5× or 0.01×) was added to silica nanoshells per mg of nanoshells and corresponded to high- or medium-density coating formulation, respectively. For low-density formulations, the volume of diluted 1V209/NHS/EDC (0.01×) added to nanoshells was kept constant, but the reaction time was reduced to 30 min. All conjugates were washed twice as before and reconstituted at 20 mg/mL based on silica nanoshell mass for further characterization. To calculate the number of ligands, a standard curve was created using serial dilutions of known concentrations of 1V209. 1V209's peak absorbance at 283 nm was used to interpolate the number of TLR7 ligands conjugated per nanoshell, which was subsequently converted to the total number of ligands in the solution. Correction for scattering by the nanoshells was needed for nanoshell structure. Inner light scattering caused by the incident light interacting with the hollow nanoshell wall and passing through the interior filled with a culturing medium may be amplified by the

difference in refractive indices between the solid wall and the culturing medium. Aggregates or colloids present in the nanoshell suspension also scatter light elastically from the solution. This effect, known as Rayleigh scattering, creates high background interference at the blue end of the absorption spectrum.[66] Hence, a Rayleigh scattering curve-fitting proportional to λ^{-4} was applied to perform the baseline subtraction, and the number of ligands per nanoshell was quantified after scattering background subtraction. Note that by using blank silica nanoshells to estimate the light-scattering effect, it provided a reasonable baseline correction for the ligand absorbance measurement. However, nanoparticle aggregation and self-quenching (if measuring fluorescence) may also impact the accuracy of surface concentration estimation.

2.3.8 Animals

Female Balb/c and C57BL/6 mice (6−8 weeks old) were purchased from The Jackson Laboratory (Bar Harbor, ME) and from Charles River Laboratories (Wilmington, MA) for in vivo and bone-marrow-derived dendritic cells (BMDCs) isolation. Mice genetically deficient for TLR7 were kindly gifted from Dr Shizuo Akira (Osaka University, Osaka, Japan) and maintained by the UCSD Animal Care Program. All procedures and protocols were approved by the UCSD IACUC.

2.3.9 In Vitro Cytokine Induction in mBMDCs and hPBMCs

Murine BMDCs from C57BL/6 mice or human peripheral blood mononuclear cells (PBMCs) isolated from buffy coats obtained from the San Diego Blood Bank (San Diego, CA) were prepared as described previously.[67] mBMDCs and hPBMCs were plated in a 96-well plate at 1×10^5 or 2×10^5 cells/well (150 μL), respectively. Unconjugated 1V209, NS-TLR7a, or silica shells were serially diluted in DMSO and diluted further with RP-10 at a final DMSO concentration of 0.5%. After incubating 18 h at 37 °C under 5% CO_2, the supernatants were collected and the levels of cytokines (IL-6, IL-12, and IL-1β) were determined by ELISA.

2.3.10 In Vitro Intracellular Tracking of NS-TLR7a in APCs

BMDCs were plated at a density of 6×10^5 cells/well in #0 cover glass 24-well plates (In Vitro Scientific, Noble Park North, Australia) with RP-10 at 37 °C. The cells were treated with NS-TLR7a at a 1 μM 1V209 equivalent concentration or vehicle control. Samples were stained with lysotracker green (65 nM, Thermo Fisher Scientific) for the late endosome/lysosomes and with vybrant dye (50 nM Thermo Fisher Scientific) for nuclei for 30 min. Cell membranes were stained with cell mask deep red (Thermo Fisher Scientific) for 5 min before image acquisition. Samples were maintained at 37 °C with a 5% CO_2 using a 2 stage-top incubator. Images were obtained using an oil objective on an SP8 Leica confocal microscope. All samples were monitored up to 6 h.

2.3.11 In Vivo Immunization Study

Balb/c mice were intramuscularly injected 20 μg OVA with NS-TLR7a, a mixture of 1V209 and silica nanoshells, unconjugated 1V209, or silica nanoshells on days 0 and 20. The mice intraperitoneally (i.p.) received 100 μg OVA on day 39. Mice were sacrificed on day 42, and the sera and spleens were collected. Sera were analyzed with IgG1 and IgG2a by ELISA. Splenocytes were cultured with OVA (100 μg/mL) in RP-10 for 5 days at 37 °C, and IFN-γ in the supernatant was determined by ELISA.

2.3.12 Statistical Analysis

One-way ANOVA with Tukey's post hoc test was employed to compare two or more groups. To compare cross- sectional outcomes among two or more groups, one-way ANOVA with Dunn's post hoc test was applied. $p < 0.05$ was considered statistically significant and denoted as $*p < 0.05$, $**p < 0.01$, and $***p < 0.001$.

2.4 Results and Discussion

2.4.1 Synthesis and Characterization of Silica Shells Conjugated to TLR7 Agonists

Hollow silica nanoshells were synthesized as previously described.[21] Synthesis and conjugation processes are depicted in Figure 2.1a. Nanoshells were modified with APTES to functionalize the surface with a reactive primary amine group and, subsequently, conjugated to the carboxylic end of 1V209, which is a purine derivative TLR7a.[65] The TEM images illustrate that no morphological changes were observed after 1V209 conjugation to 100 nm nanoshells. The linkage between silica nanoshells and TLR7 ligand was confirmed by measuring the absorption of 1V209 at 283 nm on NS-TLR7a preparations (Figure 2.1b). Additionally, NS-TLR7a fluoresces at 450 nm when excited with a wavelength of 283 nm (Figure 2.1c). This attribute enables convenient in vitro visualization without additional dye labeling to avoid potential influence on the interaction between nanoshells and cells.

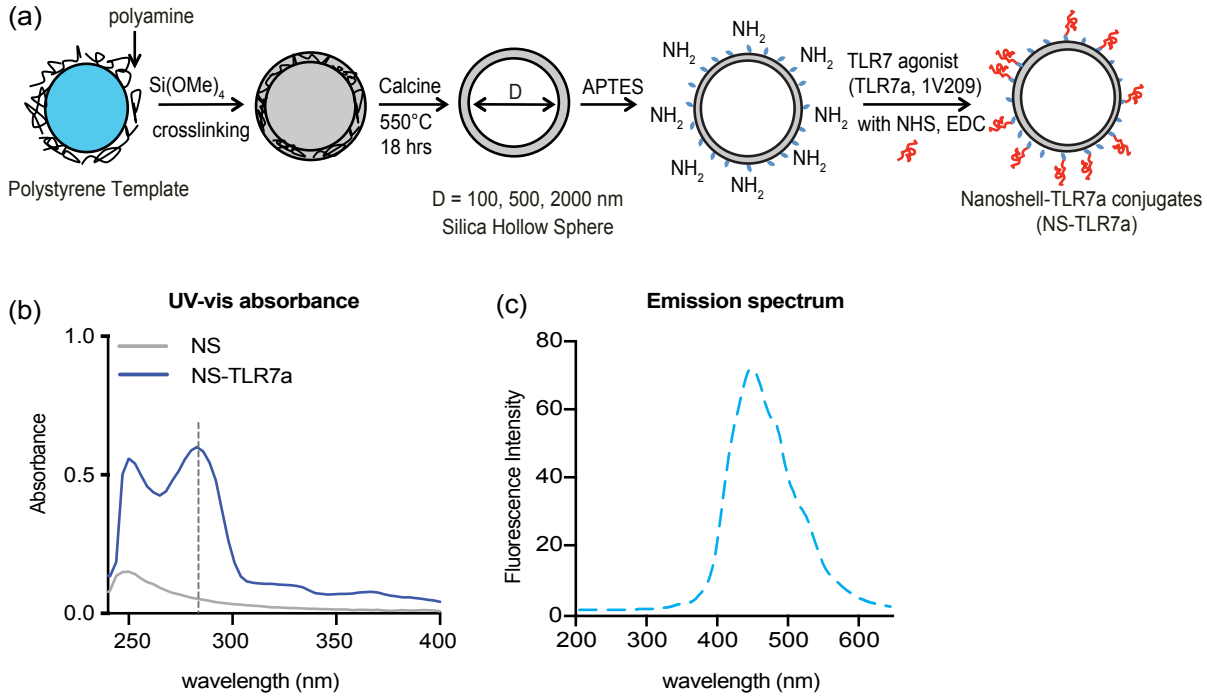

Figure 2. 1: Synthesis and characterization of NS-TLR7a.
(a) Synthesis and conjugation process of NS-TLR7a. (b) UV−vis absorbance spectrum of NS-TLR7a. (c) Fluorescence spectrum of NS-TLR7a with high coating density.

2.4.2 Higher Ligand Density Increase TLR7 Activation of NS-TLR7a

The density of TLR7 ligands on carrier impacts functional outcomes of the conjugates.[37] To determine the influence of the ratio of nanoshells to 1V209, three different reactions were performed: (1) 0.084 mmol 1V209: 1 mg silica nanoshells reacted 2 h; (2) 0.017 mmol 1V209: 1 mg silica nanoshells reacted 2 h; and (3) 0.017 mmol 1V209: 1 mg silica nanoshells reacted 30 min. The amount of 1V209 conjugated to 100 nm nanoshells was quantified using UV−vis absorbance with a Rayleigh scattering subtraction. The absorbance spectra showed that a strong correlation between the initial concentration of 1V209 during conjugation and the final ligand density, 1V209, at the highest molar ratio (0.084 mmol 1V209: 1 mg silica nanoshells) for 2 h of reaction time yielded the highest density of 1V209 on the nanoshell surface. Nanoshells conjugated with less than 1,000 1V209 ligands per nanoshell are defined as low-density NS-TLR7a, 1,000−6,000 1V209 ligands per nanoshells are defined as medium-density NS-TLR7a, and above 6,000 1V209 ligands per nanoshell are defined as high-density NS-TLR7a.

Prior to testing the efficacy as a function of ligand coating, the effect of ligand density on cell viability was evaluated because previous reports have indicated that silica particles may induce apoptosis or necrosis in human immune cells and cancer cells.[68,69]An MTT viability assay was employed to assess the cytotoxicity of the NS-TLR7a in BMDCs (Figure 2.2a). BMDCs were incubated with high-, medium-, or low-density NS-TLR7a, unconjugated 1V209, or silica nanoshells alone. Viability was normalized to the vehicle control (=100%). Medium- and high-density NS-TLR7a equivalent to 2,500 nM TLR7 ligands yielded 96 and 100% viabilities, respectively. The silica nanoshells without conjugation only showed 26% viability. Since the silica toxicity is mainly derived from its bare surface, the biocompatible 1V209 ligand coverage likely reduces the accessibility of silica surface,[70,71,72] thereby mitigating the toxicity as the coating

density increases. These data show that conjugation with 1V209 at medium and high coating densities counteracted the cytotoxicity of silica nanoshells alone.

A strong correlation was observed between ligand density and in vitro immune response. Downstream cytokines IL-6 and IL-12 were measured to assess dendritic cell (DC) activation. IL-6 and IL-12 can promote the differentiation of Th1 cells or cytotoxic T cells, which directly eliminate pathogens or cancerous cells.[73] The agonistic activity of the 1V209 ligand was enhanced in both human PBMCs and mouse BMDCs treated with medium- and high-density NS-TLR7a. The half-maximal effective concentration (EC50) and maximum effect (Emax) of the drug performance were quantified. High-density NS-TLR7a exhibited the lowest EC50 in both IL-6 and IL-12 readouts (279 ± 118 nM and 262 ± 20, respectively). The Emax of high-density NS-TLR is 1.5- and 3-fold higher than that of unconjugated 1V209 for IL-6 and IL-12 cytokine releases, respectively. As for the low-density NS-TLR7a, this formulation appeared to have a lower potency. These cumulative results indicate that high coating density NS-TLR7a using 100 nm nanoshells has the highest efficacy compared to unconjugated 1V209 and to the medium- and low-density coating NS-TLR7a.

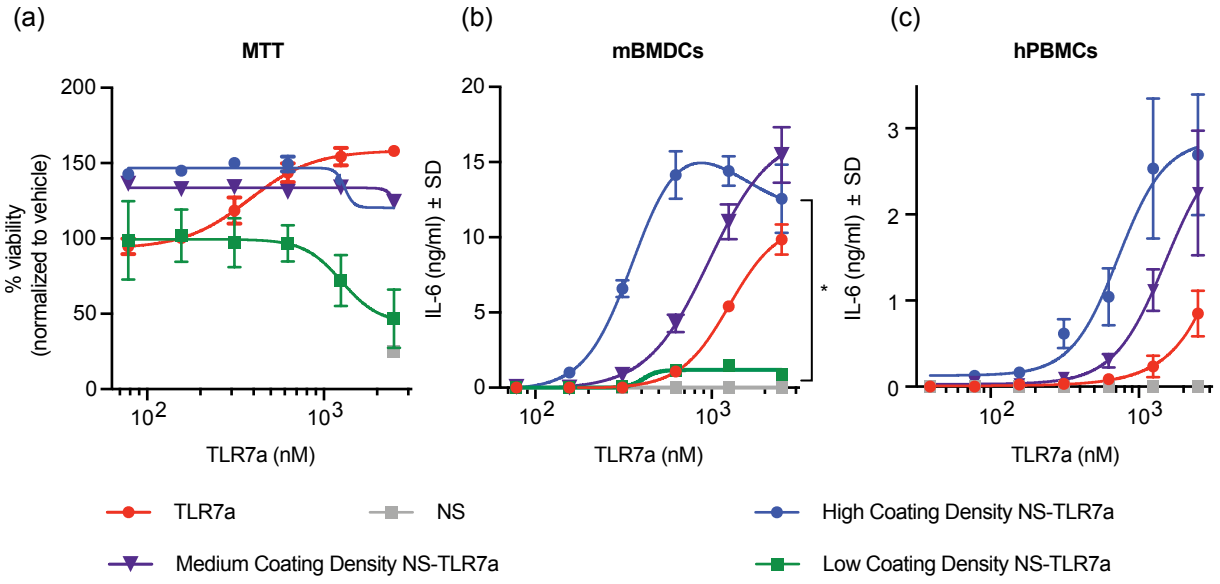

Figure 2. 2: NS-TLR7a induces cytokine production and impacts viability in murine and human immune cells in a dose-dependent manner.
Mouse BMDCs (10^5 cells) or human PBMCs (2×10^5 cells) were plated and incubated with serially diluted 100 nm NS-TLR7a at different coating densities for 18 h. (a) Cell viability in BMDCs for different coating density NS-TLR7a. Cell viability was measured by the MTT assay. IL-6 released in the culture supernatants of (b) mouse BMDCs or (c) human PBMCs incubated with unconjugated TLR7a, high, medium, low coating density NS-TLR7a, and NS. IL-6 cytokine was measured via ELISA. Cytotoxicity and cytokines were plotted by the concentration of TLR7a that were equivalent to unconjugated TLR7a. All data are representative dose−response curves in means ± SD and representative of three experiments. *$P < 0.05$ by two-way analysis of variance (ANOVA) with Tukey's post hoc analysis.

2.4.3 Size of Silica Nanoshell Carriers Influences the Immune-Stimulatory Potency of NS-TLR7a

Previous studies demonstrate that innate immunostimulatory potencies of low-molecular-weight TLR7 ligands correlate with the size of drug carriers.[37] Such size-dependent immunomodulation can be attributed to various mechanisms such as particle internalization or intracellular distribution in DCs that interfere with maturation signaling.[74,75] Therefore, it is hypothesized that the size of silica nanoshells may influence the immune potencies of the TLR7 ligand−nanoshell conjugates. To test this hypothesis, 100, 500, and 2,000 nm hollow silica nanoshells were synthesized, as previously described[76,77] (Figure 2.3a−c), and mouse BMDCs

were treated with unconjugated 1V209, silica nanoshells, or NS-TLR7a of various sizes (100, 500, or 2,000 nm).

Differently sized NS-TLR7a were incubated with BMDCs at 1V209 = 2,500 nM. For these experiments, the absolute concentration of the 1V209 was kept constant, and all conjugates were with fixed coating ligands per area; therefore, the concentration of the silica shells was varied to maintain a constant 1V209 concentration. Silica nanoshells (100 nm) conjugated with 1V209 stimulated the highest cytokine release in BMDCs compared to 500 or 2,000 nm silica nanoshells, as shown in Figure 2.3d,e. Since several viruses have diameters of about 100 nm,[78], the data was consistent with a 100 nm-sized NS-TLR7a, mimicking how pathogens are recognized by APCs and, therefore, enhancing the efficacy of the agonist. Silica nanoshells with a 100 nm diameter with high coating density demonstrated the most potent response and therefore were chosen for further studies.

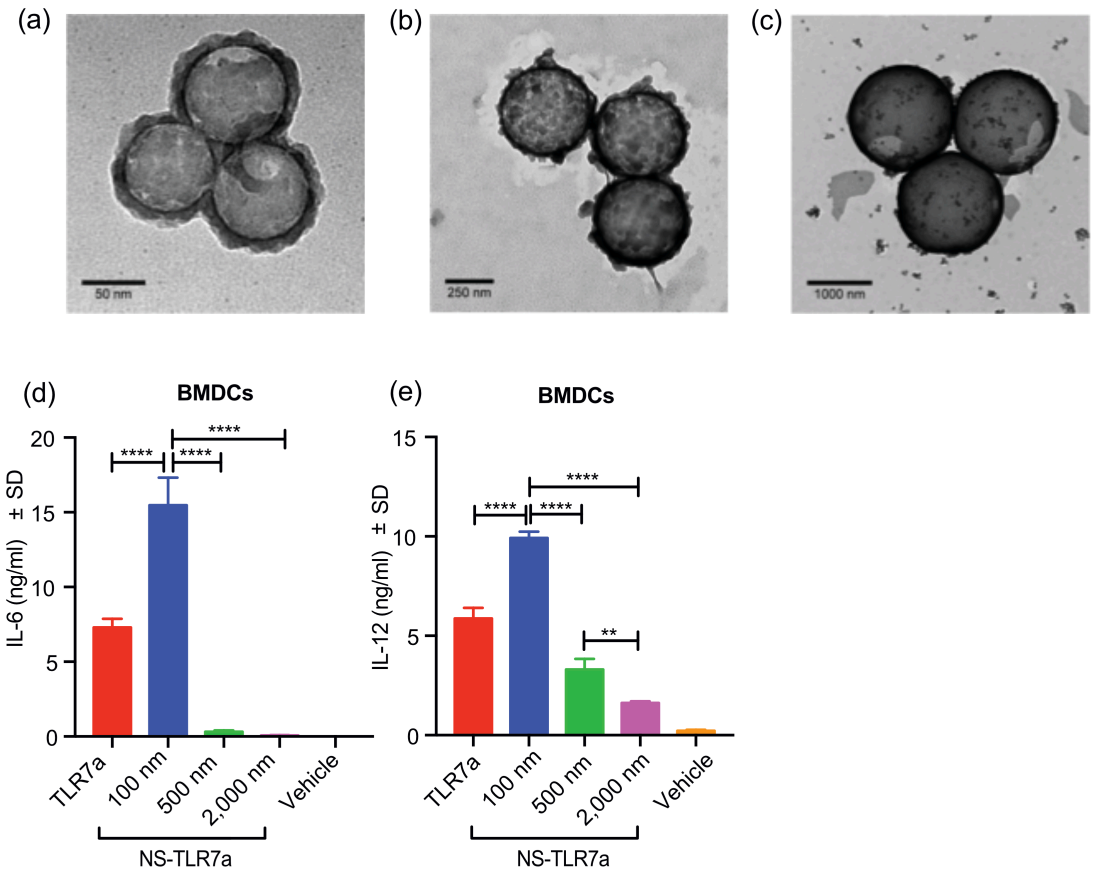

Figure 2. 3: Characterization of silica nanoshells with 100, 500, and 2,000 nm diameters. TEM images of (a) 100 nm, (b) 500 nm, (c) 2,000 nm unmodified silica shells. Mouse BMDCs (10^5 cells) were plated and incubated with serially diluted NS-TLR7a with various sizes of particles for 18 h. (d) IL-6 and (e) IL-12 released in the culture supernatants of mouse BMDCs incubated with unconjugated TLR7a, TLR7a-conjugated 100, 500, and 2,000 NS. For all experiments, TLR7a = 2,500 nM. The level of cytokines was measured by ELISA. All data shown are means ± SD of triplicates and representative of three independent experiments showing similar results. ** and **** denote $p < 0.01$ and $p < 0.0001$ by ordinary one-way ANOVA with Tukey's post hoc analysis, respectively.

2.4.4 NS-TLR7a Quickly Enters BMDCs and Specifically Stimulates TLR7 Signaling

TLR7, located at an endosomal compartment, signals through the MyD88 pathway and results in NF-κB activation, leading to proinflammatory cytokine (IL- 6 and IL-12) release to drive DCs' maturation (Figure 2.4a). Therefore, the trafficking of NS-TLR7a into the endosomal compartment of DCs is important for the ligand to engage with the endosome in DCs where the TLR7 locates. Self-fluorescent properties of 1V209 were used to assess the internalization of NS-

TLR7a in mouse BMDCs over time, using live imaging confocal microscopy. As shown in Figure 2.4b, NS-TLR7a associated with the cell membrane of BMDCs within 1 h and were trafficked into the cytosol compartment at 2 h post- treatment. By 6 h, the majority of NS-TLR7a localized in the late endosome/lysosome subcellular compartments. Collectively, these results showed that NS-TLR is readily taken up by DCs and accumulates in the late endosome/lysosome.

Following the confirmation of NS-TLR7a uptake by BMDCs, TLR7a specificity was investigated in BMDCs derived from wild-type control (WT) and TLR7 knockout (TLR7KO) mice. Level of secreted proinflammatory cytokines IL-6 was used to assess TLR7-mediated NF-κB activation. LPS, a TLR4 agonist, was used as a positive control. As shown in Figure 2.4c, the unconjugated TLR7a, NS- TLR7a, and LPS induced IL-6 in the supernatant of WT BMDCs. However, IL-6 was not detectable in TLR7KO BMDCs treated with 1V209 or NS-TLR7a alone. Conversely, LPS produced IL-6 in TLR7KO BMDCs as it can still stimulate TLR4. These results demonstrated that TLR7a conjugated onto silica nanoshells retain TLR7 specificity.

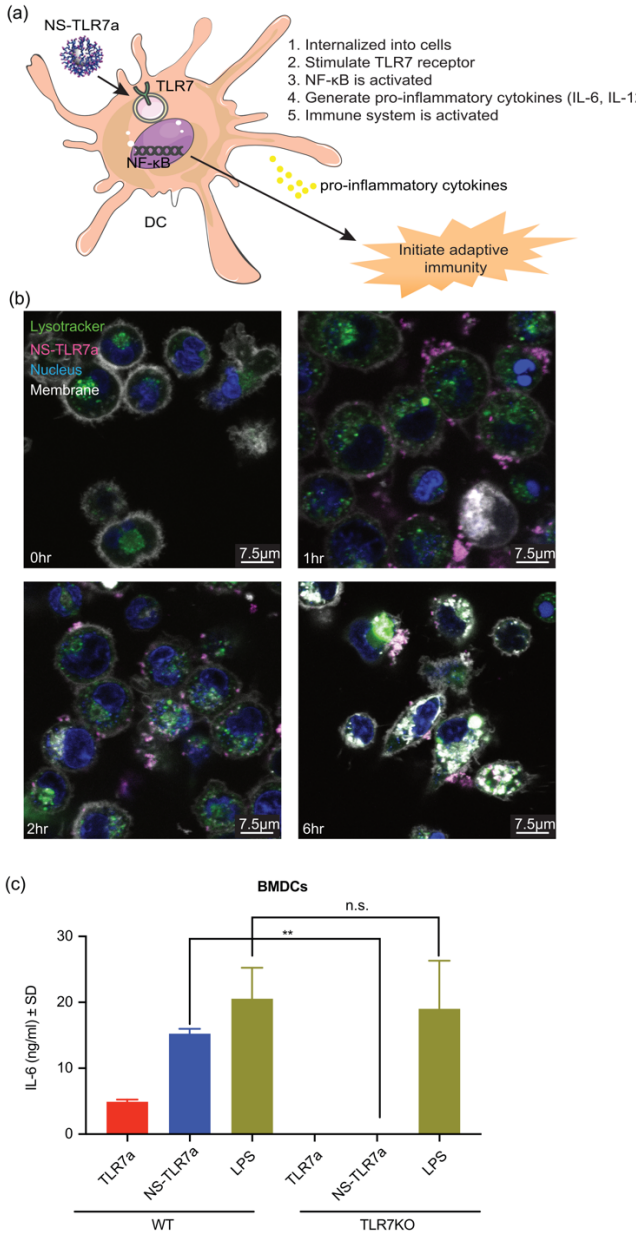

Figure 2. 4: NS-TLR7a enters the endosome compartment of mouse BMDCs.
(a) Illustration of NS-TLR7a targeting TLR7 located in the endosomal compartments stimulating proinflammatory cytokine production and enhancing the immune response. (b) Mouse BMDCs were incubated with NS-TLR7a (pink) for up to 6 h. Live cell dyes for the late endosome/lysosomes (lysotracker, green), nuclei (DAPI, blue), and membrane (membrane mask, white) were added 5−30 min prior to acquisition. Images were acquired 1, 2, and 6 h post-treatment. Untreated BMDCs served as the 0 h negative control. NS-TLR7a progresses from the media, through the membrane, into the cytoplasm, and eventually resides in the late endosome/lysosome of the cell. (c) Unconjugated TLR7a (1,250 nM), NS-TLR7a (1,250 nM), and 100 ng/mL LPS (TLR4 agonist) were incubated with wild-type or TLR7-deficient BMDCs. Secreted IL-6 protein levels were measured by ELISA. All data shown are means ± SD and representative of three independent experiments showing similar results. **** denotes $p < 0.0001$ by ordinary one-way ANOVA with Bonferroni post hoc.

2.4.5 Combination of TLR7a and Silica NS Activates NLRP3 Inflammasome

The silica nanoshell alone or as a conjugate may enhance the immune response.[79] Several studies have reported that the phagocytosis of particulates results in the activation of NACHT, LRR, and PYD domain-containing protein 3 (NALRP3), a protein that acts as an intracellular PRR.[79,80,81,82,83] Upon activation, NALRP3 oligomerizes into a multiprotein complex containing NALRP3, caspase-1, and apoptosis-associated speck-like adaptor protein (shown as ASC in Figure 2.5), which is commonly known as the NLRP3 inflammasome.[80] Such inflammasome regulates inflammatory cytokines such as IL-1β, activating the innate immune cells.[84,85] Inflammasome-mediated release of IL-1β in BMDCs requires two signals: TLR7a activation and NLR activation. Therefore, it was hypothesized that NS-TLR7a can modulate IL-1β production: silica nanoshells (NLR activator) trigger inflammasome complex formation concomitant with 1V209 (TLR7 activator)-signaling pathway activation. To test this hypothesis, BMDCs were treated with varying concentrations of NS-TLR7a, and IL-1β levels in the media were measured by ELISA as an indicator of inflammasome formation. As shown in Figure 2.5a, NS-TLR7a induced IL-1β production in a dose-dependent manner, whereas unconjugated 1V209 or silica nanoshells alone stimulated negligible IL-1β release. Previous studies showed that pure TLR agonists induced IL-1β secretion when there were existing NLRP3 stimuli in the cells such as mitochondrial dysfunction-derived signal, adenosine 5′-triphosphate (ATP), nigericin, etc. In the present study, pure 1V209 (TLR7a) did not induce IL-1β secretion because 1V209 alone did not have NLRP3 stimuli (silica nanoshells) to stimulate the NLRP3 pathway and transform pro-IL-1β into releasable IL-1β. Treating cells with a mixture of unconjugated silica nanoshells and unconjugated 1V209 resulted in a similar level of IL-1β release to that seen with NS-TLR7a treatment. These results suggest that IL-1β production is dependent on two signaling pathways triggered by the presence

of both 1V209 and silica nanoshells but does not require conjugation or cotrafficking through the cells.

To verify that IL-1β release was TLR7-dependent, NS-TLR7a were incubated with TLR7KO BMDCs. TLR7KO BMDCs treated with NS-TLR7a failed to release IL- 1β, indicating that IL-1β release requires TLR7 activation (Figure 2.5b). The mechanism of pro-IL-1β to IL-1β conversion was also verified. Pro-IL-1β is an inactive form and requires caspase to proteolytically cleave and generate releasable IL-1β; therefore, WT BMDCs were incubated with a pan-caspase inhibitor, Z-VAD-FMK, to assess whether NS-TLR7a- mediated IL-1β release was caspase-1-dependent. Caspase inhibition blocked IL-1β release in NS-TLR7a -treated cell (Figure 2.5c), while IL-6 release was refractory to the presence of Z-VAD-FMK (Figure 2.5d). These results indicate that caspase-meditated inflammasome activation by both silica nanoshells and TLR7 activation leads to IL-1β release, and the induction of proinflammatory cytokines IL-6 was independent of caspase-inflammasome activation.

Figure 2.5e depicts a hypothetical mechanism of action by which NS-TLR7a stimulates the innate immune response. The data suggested that these NS-TLR7a can improve the pre-existing innate immune-stimulatory agents and trigger IL-1β production without the need for prepriming cells, while existing nanoparticles require an extra step of prepriming cells. A two-pronged pathway is proposed for NLRP3 inflammasome activation in DCs: the first signal is triggered by 1V209 to generate NALP3 and pro-IL-1β production through the activation of NF-κB, while the second signal is triggered by silica nanoshells. The data are consistent with 1V209 triggering the NF-κB pathway and producing pro-IL-1β (inactive form), while silica nanoshells stimulate the formation of the NLRP3 inflammasome, which cleaves pro-IL-1β into IL-1β (active form) for release. The inflammasome/IL-1 pathway represents a potential therapeutic target for developing

novel cancer treatments in responsive tumor types.[86,87]

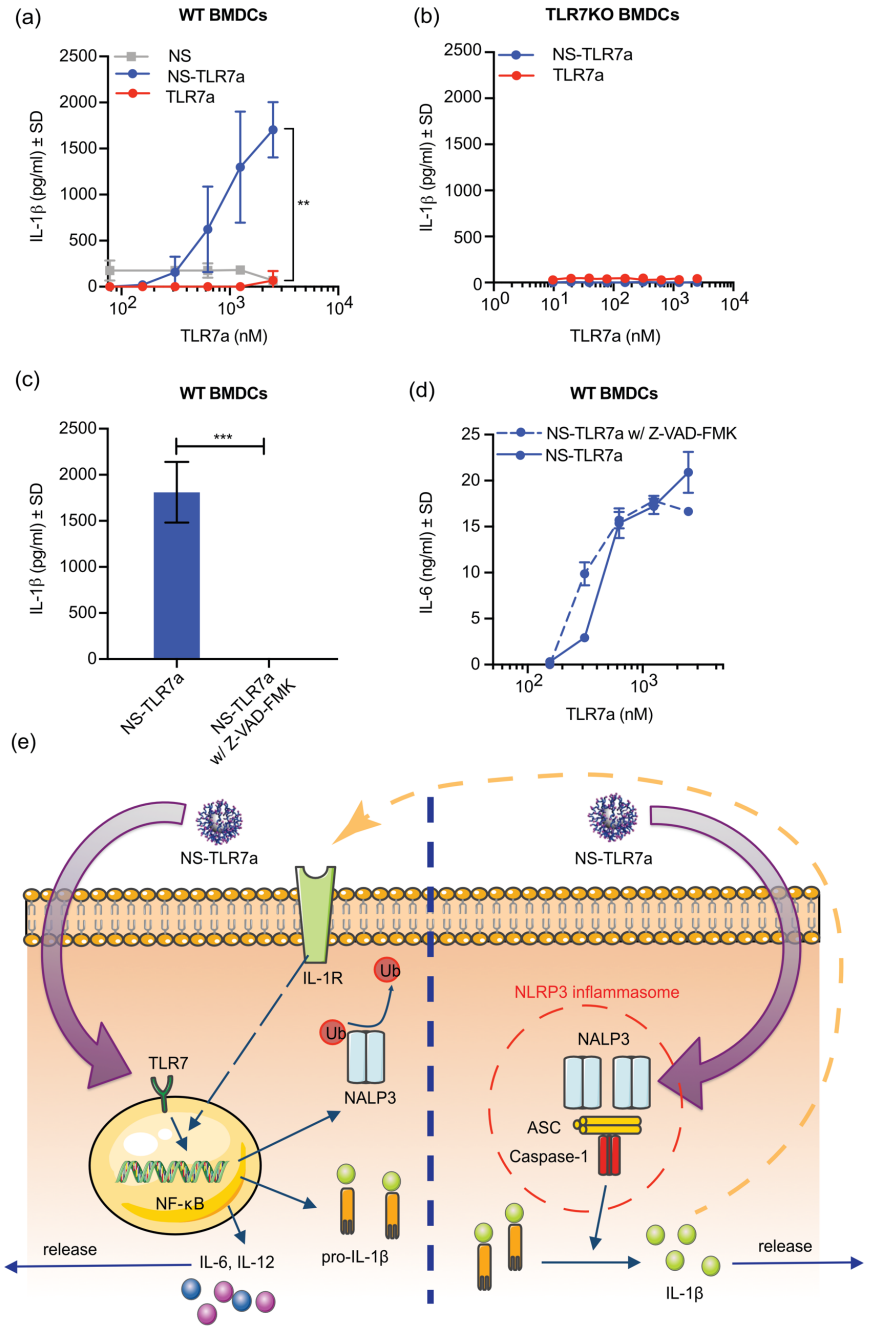

Figure 2. 5: NS-TLR7a induces IL-1β release in BMDCs.
NS-TLR7a (75−2,500 nM, high coating density), unconjugated TLR7a, and NS were incubated with BMDCs for 18 h. IL-1β induction in (a) wild-type BMDCs and (b) TLR7-deficient BMDCs. NS-TLR7a (2,500 nM) were incubated with wild-type BMDCs in the presence of pan-caspase inhibitors (Z-VAD-FMK), and (c) IL-1β and (d) IL-6 inductions were measured. All cytokines were measured by ELISA. All data shown are means ± SD in triplicates. Dose−response curve was analyzed by one-way ANOVA with Dunn's multiple comparison test. (e) Current working hypothesis of the mechanism of TLR7 signaling and NLRP3 pathway induced by NS-TLR7a.

2.4.6 NS-TLR7a Enhances Cellular and Humoral Immune Response

Conjugation of TLR7 ligands onto silica nanoshells can enhance the in vitro potency of TLR7 agonistic activity and IL-1β production, and silica nanoshells can support prolonged local depot effects that may enhance immune-stimulatory effects when translating to in vivo studies.[88] Therefore, an immunization model using OVA was performed to study the effects of NS-TLR7a on the in vivo immune response. IgG2a and IgG1 were used as indicators for Th1-type and Th2-type immune responses, respectively.[89] The Th1-type response, regulating cellular immunity, contributes to the development and activation of cytotoxic T cells. Conversely, Th2-type immunity regulates the humoral immune response and induces the proliferation and differentiation of B cells. Th1-type immunity is critical for cancer immunotherapy and virus elimination, while Th2-type immunity is critical for body protection against parasite infection.[39,90] Five groups (n = 3–4) of mice were immunized with OVA plus (1) silica nanoshells alone, (2) 1V209 alone, (3) mixture of 1V209 and nanoshells without conjugation (Mix.), (4) NS-TLR7a, and (5) vehicle as a negative control. The simple mixture of silica nanoshells and 1V209 without covalent bonds was evaluated at the same time to assess whether the linkage between TLR7 ligands and nanoshells is needed to have desirable pharmacokinetics. The mice were immunized as protocol shown in Figure 2.6a. Antibody production in sera is shown in Figure 2.6b,c.

NS-TLR7a (covalent bond) enhanced both IgG2a and IgG1, while unconjugated 1V209 or vehicle-treated groups showed nearly zero IgG2a (Th1 response) production as measured by ELISA. NS-TLR7a treatment showed an approximately 1,000-fold increase in OVA-specific IgG2a antibodies compared to silica nanoshells or the mixture of 1V209 and silica nanoshells. Unconjugated 1V209 did not enhance IgG2a production, possibly due to rapid clearance from the injection site because of the undesirable pharmacokinetics of low-molecular-weight drugs. No

synergistic effect on IgG2a production was observed in samples treated with unconjugated silica nanoshells and free TLR7a (Mix.). These results indicated that simultaneously activating the two pathways was not sufficient to generate a strong Th1 immunity. Because the antigen-specific IFN-γ response indicates the induction of the Th1-type immunity, IFN-γ production was measured in splenocytes isolated from treated mice. Consistent with the trends observed in Th1-type cellular responses, treatment with NS-TLR7a stimulated higher antigen-specific IFN-γ release by splenocytes.

Levels of OVA-specific IgG1 antibodies were increased in all treatments containing silica nanoshells (Figure 2.6c), which suggests that silica nanoshells can enhance Th2-type response but covalent bonding between TLR7 agonists and nanoshells is required for the induction of Th1-type immune response. The mechanism of silica self-adjuvants is probably similar to that of the commercial adjuvant, alum, that activates the immune system through NLRP3 inflammasome formation.[91] However, alum is limited to a Th2-type response enhancement and fails have used TLR7a adsorbed onto commercialized to elicit an equally efficacious Th1 response.[92,93] Some studies adjuvant, alum, to improve adjuvanticity. Since alum is neurotoxic and may damage the blood−brain barrier, there are serious concerns. In the present study using silica nanoshells as the delivery platform of TLR7a, the potential toxicity of silica particle is mitigated by the free surface coverage. The MTT assay (Figure 2.2c) that measured the metabolic activity to model the cell toxicity showed that the higher coverage (higher 1V209 ligand per nanoshell) silica nanoshells displayed lower cytotoxicity, which is likely due to 1V209 ligand blocking the free silica surface. This is consistent with previous reports that the surface generation of reactive oxygen species is the main source of silica toxicity. 1V209 is a small-molecule drug that has undesired properties, such as fast clearance after administration. As shown in Figure 2.6b,c, unconjugated TLR7a

(1V209) demonstrated a quiescent adjuvant activity as shown in the low induction of IgG2a and IgG1. These results implied that unconjugated TLR7a small molecules (1V209) cleared away relatively rapidly from the injection site and thus failed to induce a robust immune response. In summary, small-molecule drug TLR7a cannot be retained locally to continuously stimulate the TLR7-signaling pathway. Conjugation, however, was able to lengthen the retention time of small-molecule agonists, leading to continuous recruitment of APCs and sustained stimulation in situ. Localizing 1V209 largely benefits the efficacy of this small-molecule TLR7a drug. These data together with our in vitro studies implied that the TLR7 ligand−nanoshell conjugates induced both inflammasome-dependent IL-1β and inflammasome-independent proinflammatory cytokines that enhanced the function of APC and induced the desirable antigen-specific Th1-biased immune responses.

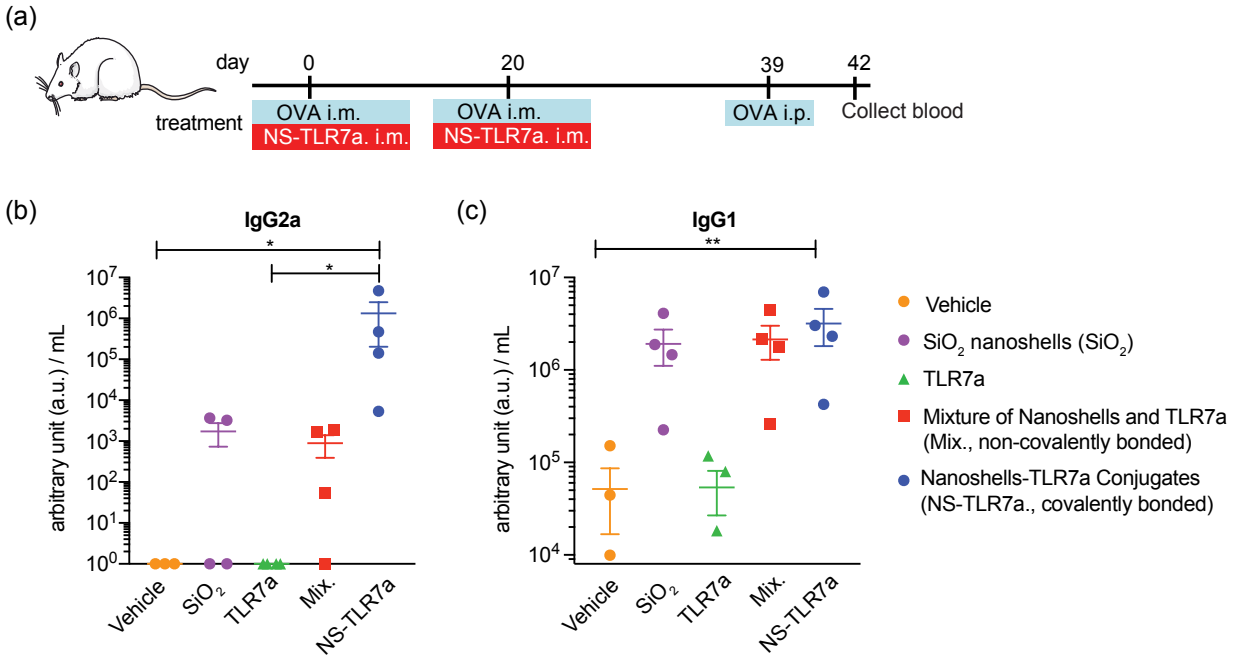

Figure 2. 6: Immunization study of NS-TLR7a with OVA as a model antigen.
(a) Balb/c mice (n = 3−4) were intramuscularly immunized with chicken OVA and NS-TLR7a, unconjugated TLR7a mixed with silica nanoshells (Mix.), silica nanoshells or unconjugated TLR7a alone on days 0 and 20 and sacrificed on day 42. Serum levels of (b) anti-OVA IgG2a and (c) IgG1 measured by ELISA are shown as mean ± standard errors. Data were analyzed with Kruskal−Wallis one-way ANOVA with Dunn's post hoc analysis. * denotes $p < 0.05$ and ** denotes $p < 0.01$.

2.5 Conclusions

The present study has shown that the immune potency of small-molecule TLR7 ligands was amplified when conjugated to silica nanoshells while retaining the ligand−receptor specificity. The amplification is both particle-size-dependent and ligand-density-dependent, where high-density-coated 100 nm silica nanoshells showed the greatest agonistic activities in vitro. The increased coverage of TLR7 ligands on silica nanoshell surfaces mitigated the cytotoxicity of the bare silica nanoshells and improved the therapeutic effect. The NS-TLR7a enhanced both TLR7 signaling and induced the activation of the NALP3 inflammasome to achieve a more robust immune response. The induction of proinflammatory cytokines IL-6 and IL-12 was refractory to the caspase inhibitor, which indicates that the induction of these cytokines was solely TLR7-dependent and -independent of caspase-inflammasome activation. Silica nanoshell conjugation also resulted in the lengthening of the local drug retention time to maximize drug effects. More APCs infiltrate to the administrated site, continuously activate maturation, and strengthen the subsequent immune response. Based on the in vivo vaccination study, antigen-specific immune response was displayed and successfully amplified by NS-TLR7a for both Th1-type and Th2- type immune responses. The dual enhancement implies a broader application as vaccine adjuvants or even as monotherapy for cancer treatment. These results suggested that conjugates could be used in cancer treatment as monotherapy or as a candidate for combinatorial synergistic delivery.

2.6 Acknowledgements

Chapter 2, in full, contain material as it appears in ACS Applied Materials & Interfaces 2019. Huang, Ching-Hsin; Mendez, Natalie; Hernandez Echeagaray, Oscar; Weeks, Joi; Wang, James; Vallez, Charles N.; Gude, Natalie; Trogler, William; Carson, Dennis A.; Hayashi, Tomoko; Kummel, Andrew C., ACS Publications, 2019. The dissertation author was the primary author of

this paper.

Chapter 3: Immunostimulatory TLR7 Agonist-Nanoparticles Together with Checkpoint Blockade for Effective Cancer Immunotherapy

3.1 Abstract

Mono- or dual-checkpoint inhibitors for immunotherapy have changed the paradigm of cancer care; however, only a minority of patients responds to such treatment. Combining small molecule immunostimulators can improve treatment efficacy, but they are restricted by poor pharmacokinetics. In this study, conjugated TLR7 agonists onto silica nanoparticles show extended drug localization after intratumoral injection. The nanoparticle-based TLR7 agonist increases immune stimulation by activating the TLR7 signaling pathway. When treating CT26 colon cancer, nanoparticle conjugated TLR7 agonists increase T cell infiltration into the tumors by >4× and upregulate expression of the interferon $\boldsymbol{\gamma}$ gene compared to its unconjugated counterpart by ≈2×. Toxicity assays establish that the conjugated TLR7 agonist is a safe agent at the effective dose. When combined with checkpoint inhibitors that target programmed cell death protein 1 (PD-1) and cytotoxic T-lymphocyte-associated protein 4 (CTLA-4), a 10–100× increase in immune cell migration is observed; furthermore, 100 mm3 tumors are treated, and a 60% remission rate is observed including remission at contralateral noninjected tumors. The data show that nanoparticle-based TLR7 agonists are safe and can potentiate the effectiveness of checkpoint inhibitors in immunotherapy resistant tumor models and promote a long-term specific memory immune function.

3.2 Introduction

Colorectal cancer (CRC) is one of the top three causes of cancer death world-wide, it is currently being investigated for immunotherapy.[94] Metastatic CRC (mCRC) patients usually receive systemic therapy, such as anti-VEGF or anti-EGFR, but often this results in acquired resistance resistance.[94,95] The checkpoint inhibitor antibodies, targeting programmed cell death protein 1 (a-PD-1) and cytotoxic T-lymphocyte-associated protein 4 (a-CTLA-4), block the inhibitory signals between T cells/tumor cells and T cells/APC and have shown promising therapeutic effects. Checkpoint inhibitors, such as ipilimumab (a-CTLA-4 antibody) and nivolumab (a-PD-1 anti-body), improve outcomes for many tumors, which include melanoma, advanced lung, and head and neck cancers. They are also being evaluated to treat mCRC patients.[96] However, a large portion of patients, including the majority of mCRC patients, do not respond to immune checkpoint inhibitors.[97,98,99]

Data from current clinical trials indicate that patients whose tumors are mismatch repair deficient (MMRd) are likely to respond to checkpoint inhibitor therapies.[100,101,102] It has been postulated that the DNA mismatch repair deficiency leads to more neoantigens released that are easily recognized by the body's immune cells to induce tumor-specific immune response. Pembrolizumab (a-PD-1 drug) has recently been designated by the FDA for use in MMRd tumors, regardless of the tumor location.[103] Even though immune checkpoint inhibitors have shown great promise for many cancer patients, mismatch repair proficient (MMRp) cancer patients are less responsive.[102,104] Even in MMRd mCRC, the objective response rate is about 40%.[105] Checkpoint inhibitors are not effective in MMRp mCRC[105] consistent with MMRp cancers having lower lymphocyte infiltration into tumors.[100] Therefore, rendering these tumors sensitive to immunotherapy remains a major challenge,[99] and using immunostimulatory agents could be a

complementary approach to improve cancer treatment with checkpoint inhibitors. Murine colon cancer cell line, CT26, one of the most extensively used syngeneic mouse tumor models that lack mutations in mismatch repair genes,[106,107,108] was chosen for the present study.

A previously synthesized nanoparticle-based immunostimulatory agent, which consists of a TLR7a conjugated with 100 nm silica NS termed NS-TLR7a (agonist number per nanoshell is 6,000 or greater),[109] has shown improved TLR7 immune adjuvant activity.[109] NS-TLR7a increased cytokine IL-12 secretion and activated the inflammasome pathway in mouse dendritic cells (DCs).[109] Furthermore, NS-TLR7a enhanced a Th1-biased immune response that is often associated with induction of cytotoxic T lymphocytes (CTL)[109] that play a critical role in cancer immunotherapy because they recognize and kill cancerous cells.[110] In the present study, NS-TLR7a was used to amplify the immune response combined with checkpoint inhibitors to restore the T lymphocytes' killing capability in an animal model. Such combination therapy has the potential to treat MMRp patients by developing tumor antigen-specific T cells at both the tumor site and systemically. Nanoparticle-based TLR7/8 agonists were used in a combination treatment strategy similar to previous studies. Most previous studies lacked investigation of potential immune-related adverse effects and other systemic toxicity, which is a critical problem with potent immunostimulating drugs.[111,112] Some previous studies used known tumor antigens to induce and amplify the immune response,[113] but identifying the neoantigens accounting for immune responses of spontaneous tumors is very challenging.[114] Furthermore, most focused on local control of tumor growth and did not address the potential of systemic immune responses and tumor progression at distal sites.[113,115,116] Experiments reported here have built upon previous work, but have addressed some unresolved issues identified previously and have demonstrated both the safety and efficacy of the NS-TLR7a/checkpoint inhibitor combination therapy.

In this study, the NS-TLR7a was shown to be stationary after injection and thus escaped rapid splenic clearance. Compared to systemic injection, the direct injection increases the ratio in the tumor to liver by >2,500×. Although NS-TLR7a was retained at the local injection site, it had the ability to induce a robust systemic tumor antigen-specific immune response in the CT26 murine colon cancer model. The NS-TLR7a increased $CD3^+$ tumor infiltrating lymphocytes (TIL) by 4× and upregulated the expression level of the (IFN-γ) gene compared to simply administering free TLR7a. Compared to unconjugated TLR7a, NS-TLR7a increased cytokine induction in sera that returned to baseline after 24 h. Toxicology studies of repeated doses further indicated that the NS-TLR7a had limited toxicity, and did not significantly affect the complete blood cell (CBC) count or hepatic function compared to the control vehicle. NS-TLR7a was, there- fore, combined with a-PD-1 and a-CTLA-4 antibody therapies to better inhibit tumor growth by increasing the number of infiltrating immune cells 10–100× compared to the vehicle group in the CT26 tumor model. The CT26 tumor model had only a modest response to checkpoint inhibitor monotherapy. The triple combination therapy including NS-TLR7a, a-PD-1, and a-CTLA-4 induced both injected and contralateral tumors into full remission and improved survival rates from 0% with a-PD-1 and a- CTLA-4 monotherapy to 60% with NS-TLR7a plus a-PD-1 and a-CTLA-4. Therefore, NS-TLR7a has potential to be an enhancer for current immunotherapy and may improve the outcome of cancer treatment in MMRp colon cancers and perhaps in other MMRp cancers.

Although small molecule TLR7 agonists are effective innate immune stimulators, there are two major problems for their clinical use: (1) because TLR7 is located in an endosomal compartment, effective endosomal delivery is required, and (2) TLR7a is quickly cleared after local administration. Our previous report demonstrated TLR7a conjugated to silica particles are quickly taken up by DCs and exhibit improved immune-potency.

3.3 Experimental

3.4.1 Materials

Diethylenetriamine (DETA, Cat. No. D93856), TMOS, TMPS, NHS, EDC, and organic solvents were purchased from Sigma Aldrich (St. Louis, MO). Hundred nanometer polystyrene templates were purchased from Polysciences Inc. (Warrington, PA). 2-(4-Isothiocyanatobenzyl)-diethylenetriaminepentaacetic acid (DTPA) was purchased from Macrocyclics (Dallas, TX). ^{111}InCl3 was purchased from Covidien (Mansfield, MA). 4-[6-Amino-2-(2- methoxyethoxy)-8-oxo-7H-purin-9(8H)-yl]methylbenzoic acid (1V209) was synthesized as previously described. Anti-mouse PD-1 (CD279) antibodies (clone RMP1-14, Cat. No. BP0146) or anti-mouse CTLA-4 (CD152) antibodies (clone 9D9, Cat. No. BP0164) were purchased from BioXcell (West Lebanon, NH). RPMI (Cat. No. 11875-093, Gibco) and DMEM (Cat. No. 15-013-CV, Corning) were supplemented with 10% fetal bovine serum (Cat. No. 35-011-CV, Corning) and 100 U/mL penicillin, 100 μg/mL streptomycin, 292 μg/mL glutamine (Cat. No. 10378-016, Thermo Fisher Scientific) to prepare complete media (RP-10 or DMEM-10).

3.4.2 Animals and Tumor Model

Mouse colon cancer cell line CT26 (Cat. No. CRL-2638) was purchased from American Type Culture Collection. Six- to eight-week-old female BALB/c mice were purchased from The Jackson Laboratory. 10^6 cells/50 μL PBS were s.c. injected into the right and left flanks, and treatment was started at a tumor size of approximately 100 mm^3. Tumor volume was determined by caliper with the modified ellipsoidal formula: volume (mm) = (width × width × length)/2.[117] Pain and distress in tumor-bearing mice were closely monitored. Procedures causing more than momentary or slight pain or distress must be performed with appropriate anesthesia. If a tumor becomes ulcerated or necrotic, or if a single subcutaneous (s.c.) tumor exceeds 2 cm in diameter,

immediate euthanasia is performed. For multiple s.c. tumors, when the combined volume of tumors exceeds 4 cm, euthanasia is performed. All procedures and protocols were approved by the UCSD IACUC.

3.4.3 Histological Analysis

Tissue samples were fixed in 10% formalin (one part of stock formaldehyde (37–40%) and nine parts of water) and transferred to 70% ethanol before paraffin block processing and sectioning. Immunohistochemistry used rat anti-CD3 antibody (1:200, Cat. No. ab11089, Abcam). Images were obtained using a 10× dry objective on a SP8 Leica confocal microscope. A minimum of eight fields were examined per section and at least three sections per sample. Cell count analysis was performed using ImageJ and Leica proprietary software.

3.4.4 RNA Extraction and RT-qPCR Expression Analysis

CT26-derived tumor tissues from the in vivo studies were collected and flash frozen to −80 °C for storage. Tissue lysates were prepared with a Next Advance NA-01 tis- sue homogenizer, in isolation buffer (sucrose (MW 342.3) 70 × 10^{-3} m; mannitol (MW 182.2) 190 × 10^{-3} m; HEPES pH 7–8, 20 × 10^{-3} m; EDTA pH 8, 0.2 × 10^{-3} m) supplemented with protease and phosphatase inhibitors (1:100 dilution; Cat. No. 535140, P5726, Sigma-Aldrich) and RNASE-free homogenization beads (Cat. No. SSB14B and SSB32, Next-Advance). Total RNA was extracted from cells and/or tissues lysates using the Quick-RNA Miniprep Kit (Cat. No. 11-328, Zymo Research), according to manufacturer's instructions, and reverse transcribed using the iScript cDNA Synthesis Kit (Cat. No. 170-8891, Bio-Rad). qPCR was done using SYBR Green and results were analyzed using the ΔΔCq method[118] and normalized to housekeeping genes 18S and GAPDH. Primer sequences were designed using NCBI's Primer BLAST and spanned exon-exon junctions.

3.4.5 Biodistribution

NS-TLR7a was prepared as previously described.[109] One milliliter of 3 mg/mL of NS-TLR7a was functionalized with 2 μL of 1 mg/mL DTPA and pulse-vortexed for 24 h. Functionalized NS-TLR7a was washed and resuspended in 0.1 m citrate buffer (pH 6) to 2 mg/mL solution. Two milligrams of the NS were incubated with ≈100 μCi of In^{111} chloride for 30 min. Radiolabeled NS-TLR7a was washed twice with buffer and twice with MilliQ purified water. During the wash procedure, the In^{111}-labeled NS and the supernatant were measured by dose calibrator to track the In^{111} retention. After washing, In^{111}-NS-TLR7a was resuspended to 4 mg/mL in MilliQ purified water for in vivo injection. 100 μL of In^{111}- NS-TLR7a was injected into two-tumor-bearing mice intratumorally (i.t.) or intravenously. Mice were imaged via planar scintigraphy immediately, and then 8, 24, 48, and 72 h postinjection. After 72 h, mice were sacrificed. Spleen, lung, heart, right tumor (treated), left tumor (untreated), kidney, and liver were collected and the gamma intensity counted.

3.4.6 Toxicology Analysis

(1) Sera Cytokine Analysis: Female BALB/c bearing one CT26 tumor was i.t. injected with single doses of TLR7a (50 nmol per mouse), NS-TLR7a (50 nmol TLR7a; 1.8 mg NS), NS (1.8 mg per mouse), or vehicle (n = 4 per group). Blood samples were collected at 0, 2, and 24 h after treatment, and sera were isolated. Luminex bead assays were used to determine the systemic cytokine levels of IL-6, IL-12, IP-10, and MCP-1, and were measured with the use of a MAGPIX machine (Luminex Corporation). (2) Repeated dose toxicology assessment: Female BALB/c mice (n = 4–5 per group), each bearing two CT26 tumors on the right and left flanks, were i.t. injected with NS-TLR7a or vehicle every other day for a total of 6 doses. Whole blood and sera were collected on day 14 post-treatment for CBC and biochemistry analysis. For CBC analysis, ≈50 μL

of whole blood was collected in BD microtainer ethylenediaminetetraacetic acid (EDTA) tubes (Cat. No. 365-974, BD Vacutainer Labware Medical). The tubes were flicked immediately after filling and inverted several times to distribute the anticoagulant. For biochemistry analysis, the test requires a minimum of 120 μL of sera in lithium heparin tubes (Cat. No. 22-040-104, Fisher Scientific). Both CBC and biochemistry analyses were performed by UCSD Murine Hematology and Coagulation Core Laboratory. (3) Single dose toxicology assessment: Four to five BALB/c mice per group were s.c. injected with one dose of TLR7a (12.5 nmol per injection), NS-TLR7a (12.5 nmol TLR7a; 0.44 mg silica nanoshells per injection), silica NS (0.44 mg per injection), or PBS. Approximately 50 μL of whole blood were collected in the BD microtainer EDTA tubes. The tubes were flicked immediately after filling and inverted several times to distribute the anticoagulant. CBC anal sis was performed by UCSD Murine Hematology and Coagulation Core Laboratory.

3.4.7 Analysis of Tumor-Infiltrating Immune Cells

Each mouse had two CT26 tumors on the right and left flanks. Hundred micrograms of checkpoint inhibitor, a-PD-1 and/or a-CTLA-4 antibodies were injected i.p. three times weekly (day 0, 3, 6, 9, 12, 14). A 12.5 nmol of NS-TLR7a in 50 μL PBS were injected i.t. every other day for a total of six doses (day 1, 3, 5, 7, 9, 11). Day 0 was defined as the day of first treatment. Mice were sacrificed on day 14 for tumor infiltrating lymphocyte analysis. Tumors were dissociated into cell suspension using a mouse tumor dissociation kit with use of the gentleMACS Octo Dissociator according to the manufacturer's protocol (Miltenyi Biotec). Cell suspensions were incubated and stained with cocktails of anti-mouse CD45 (Cat. No. 103-114, BioLengend) and anti- mouse CD8 (Cat. No. 48-0081, Invitrogen) antibodies at 4 °C for 30 min. Fixation/Permeabilization Solution kits were used for intracellular IFN-γ staining (Cat. No. 17-7311, BD Biosciences) and granzyme

B (Cat. No. 515-403, BioLegend). The stained cells were analyzed by flow cytometry (MACS Quant, Miltenyi Biotec).

3.4.8 Statistical Analysis

The data were pooled from 2 to 4 rounds of experiments and presented as means with standard error (SE). To determine the significance between the means of two groups, a t test with Welch's correction was performed. One-way ANOVA was used with a Bonferroni post hoc test to compare means of two or more samples. Statistical comparisons of continuous variables between groups were performed using two-way ANOVA followed by a Bonferroni post hoc test. For TIL data, a Kruskal–Wallis test was performed with Dunn's multiple comparisons test. n.s. indicates not significant and analyses are indicated as * ($p < 0.05$), ** ($p < 0.01$), ***($p < 0.001$), and ****($p < 0.0001$). GraphPad Prism software 8.3.1 version was used for all statistical analyses.

3.4 Results and Discussion

3.4.1 Locally Injected NS-TLR7a Retained at Tumor

In the present study, the biodistribution of the locally versus systemically administrated NS-TLR7a was performed to investigate whether the conjugation of TLR7a onto nanoparticles improves sustained localization of the adjuvant at a local tumor injection site. NS-TLR7a was labeled with radioactive In^{111} and injected i.t. or i.v. into mice. Each mouse had two s.c. CT26 tumors in the right and left flanks but only one tumor was injected with radiolabeled NS-TLR7a. Planar γ-scintigraphy was used to monitor the particle distribution over 72 h (Figure 3.1a). Subsequently, organ biodistribution was performed by sacrificing the mice and measuring organ radioactivity 72-h postinjection (Figure 3.1b). Scintigraphy shown in Figure 3.1a demonstrates that systemically injected (i.v.) NS-TLR7a accumulated in the reticuloendothelial system organs, such as liver and spleen, which is typical of most i.v. injected nanoparticles immediately after

injection.[119,120,121] This accretion continued with time (Figure 3.1a). Conversely, i.t. injected nanoparticles were retained at the injected tumor (right flank tumor) site for over 72 h, and only a small fraction of nanoparticles accumulated in the spleen, liver, or kidney. A small amount of i.t. injected nanoparticles traveled to the contralateral tumor (left flank tumor), as early as 24 h after i.t. injection (Figure 3.1a).

At 72-h postinjection, organs were harvested for gamma counting to quantify the nanoparticles in each organ (Figure 3.1b), for the systemically injected group, the nanoparticles mainly accumulated in liver (21.4%) and spleen (4.5%). A small portion of nanoparticles (0.3–0.4%) traveled to the tumor sites, which is likely due to a modest enhanced permeability and retention effect (EPR effect). Conversely, locally injected nanoparticles were mainly retained at the injected tumor (52.4%), and only small amounts of nanoparticles accumulated in the liver (1.4%) or spleen (0.5%). Compared to systemic injection, the direct injection increases the amount in the tumor 175× and decreases the amount in the liver 15× so the ratio in the tumor to liver increases by >2,500×. A small amount of locally injected nanoparticles traveled to the distant tumor (0.3%). The lengthened retention time with the locally injected drug is consistent with the high efficacy (vide infra) of the i.t. injected agent. Such retention may further amplify the immune response induced by TLR7 activation because the drug can continuously stimulate and drive DCs to maturation. The lower amount of nanoparticle uptake at liver and spleen after direct tumor injection is consistent with NS-TLR7a residing in the tumor for a long period of time thereby having the potential to better activate the innate immune system and enhance tumor antigen presentation.

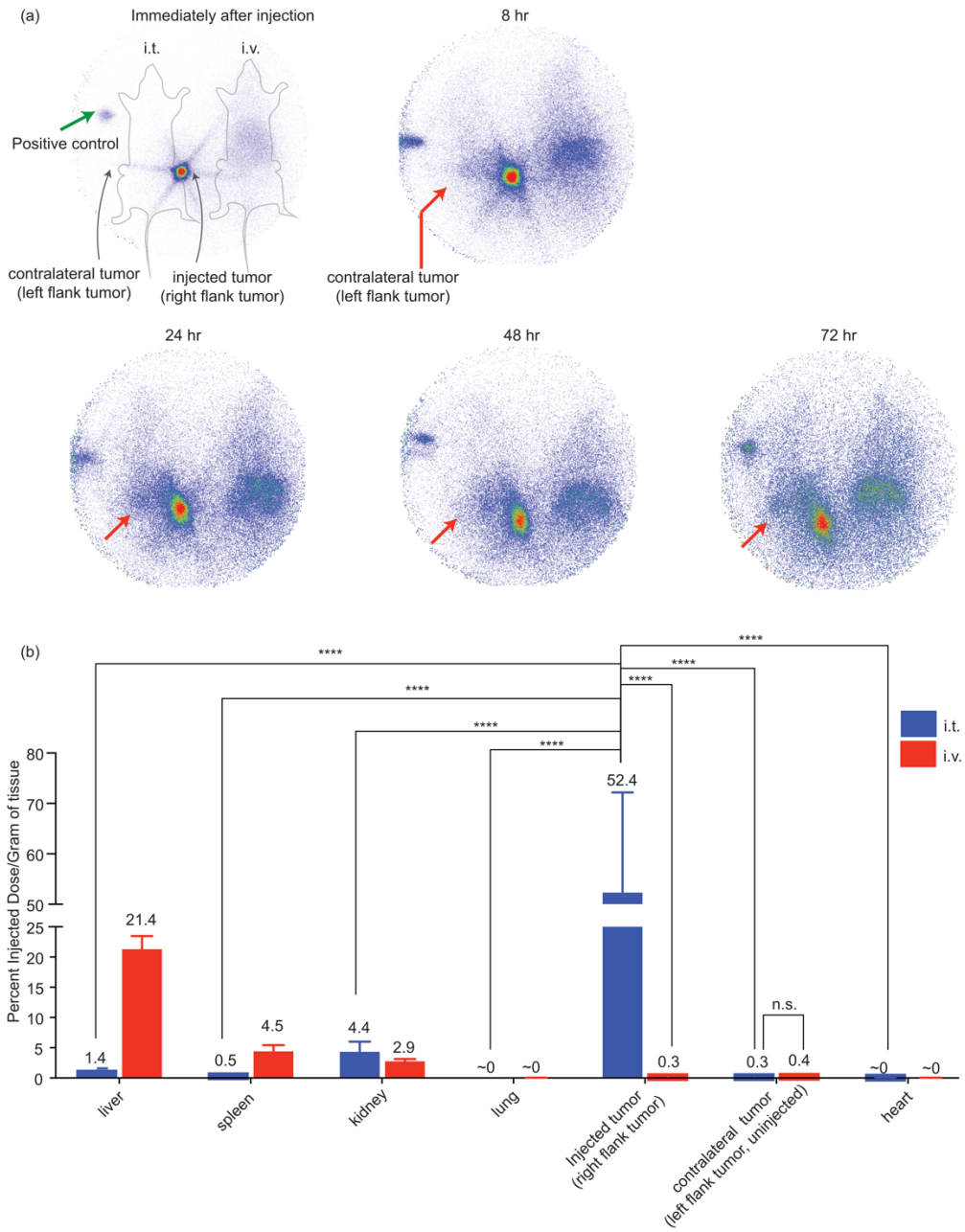

Figure 3. 1: Locally injected NS-TLR7a retained at tumor.
(a, b) Biodistribution of NS-TLR7a. In^{111} labeled NS-TLR7a were i.t. and i.v. injected into CT26 tumor bearing mice (n = 5 per group). Each mouse had two tumors in the right and left flanks to observe the particle distribution. a) Scintigraphy images of NS-TLR7a i.t. and i.v. injected mice. Pure In^{111} was placed in a tube at the scintigraphic plane as a positive control (green arrow). The Red arrows pointing to the left flank tumor that was not injected with nanoparticles. b) i.t. (blue) and i.v. (red) injected mice were sacrificed and each organ was harvested for gamma counting at 72 h after NS-TLR7a injection. Numbers above bars indicate mean values, and ≈0 when the value is smaller than 0.1. Note that the gamma counts were divided by grams of tissue so the sum is not 100%. Data shown are means ± SE of the mean of five mice in the representative of two independent experiments showing similar results. Data were analyzed with two-way ANOVA using Bonferroni post hoc test.

3.4.2 Locally Injected NS-TLR7a Enhanced the Immune Response

The effects of i.t. injected TLR7a with or without conjugation onto silica NS were tested in a CT26 mouse tumor model. Mice were implanted with 10^6 CT26 cells, and the treatment began when tumors reached 100 mm . Tumor-bearing mice were i.t. treated with TLR7a (12.5 nmol per injection), NS-TLR7a (12.5 nmol TLR7a; 0.44 mg NS per injection), NS (0.44 mg per injection), or PBS every other day up to 8 days (Figure 3.2a). As shown in Figure 3.2b, the group treated with NS-TLR7a exhibited a significant tumor growth regression (>2×) compared to the vehicle or NS-treated group until 8 days after treatment.

Tumors were harvested on day 8 for immunohistochemical analysis, and $CD3^+$ cells were assessed for T cell subpopulations in the tumor microenvironment [note: $CD3^+$ cells include both cytotoxic T cells ($CD8^+$) and T helper cells ($CD4^+$)]. As shown in the representative immunohistochemistry images (Figure 3.2c,d), and the quantified data (Figure 3.2e), TLR7a conjugated onto NS showed a higher $CD3^+$ cell infiltration (>4×) compared to unconjugated TLR7a, which is likely due to prolonged retention of NS- TLR7a in the tumor environment relative to unconjugated ligand. This allows sufficient interaction time to activate DC and subsequent adaptive immunity. The control of bare NS injection did not lead to higher $CD3^+$ cell infiltration. Consistently, the tumors injected with NS-TLR7a exhibited higher IFN-γ expression (a critical cytokine for developing adaptive immunity against cancer cells) compared to vehicle, NS, or unconjugated TLR7a in harvested tumors (Figure 3.2f), which suggests the presence of activated TIL. These data are consistent with the concept that conjugating an immunotherapy agent onto NS can improve the in vivo therapeutic effect and modulate the immune cell response to a cancerous tumor.

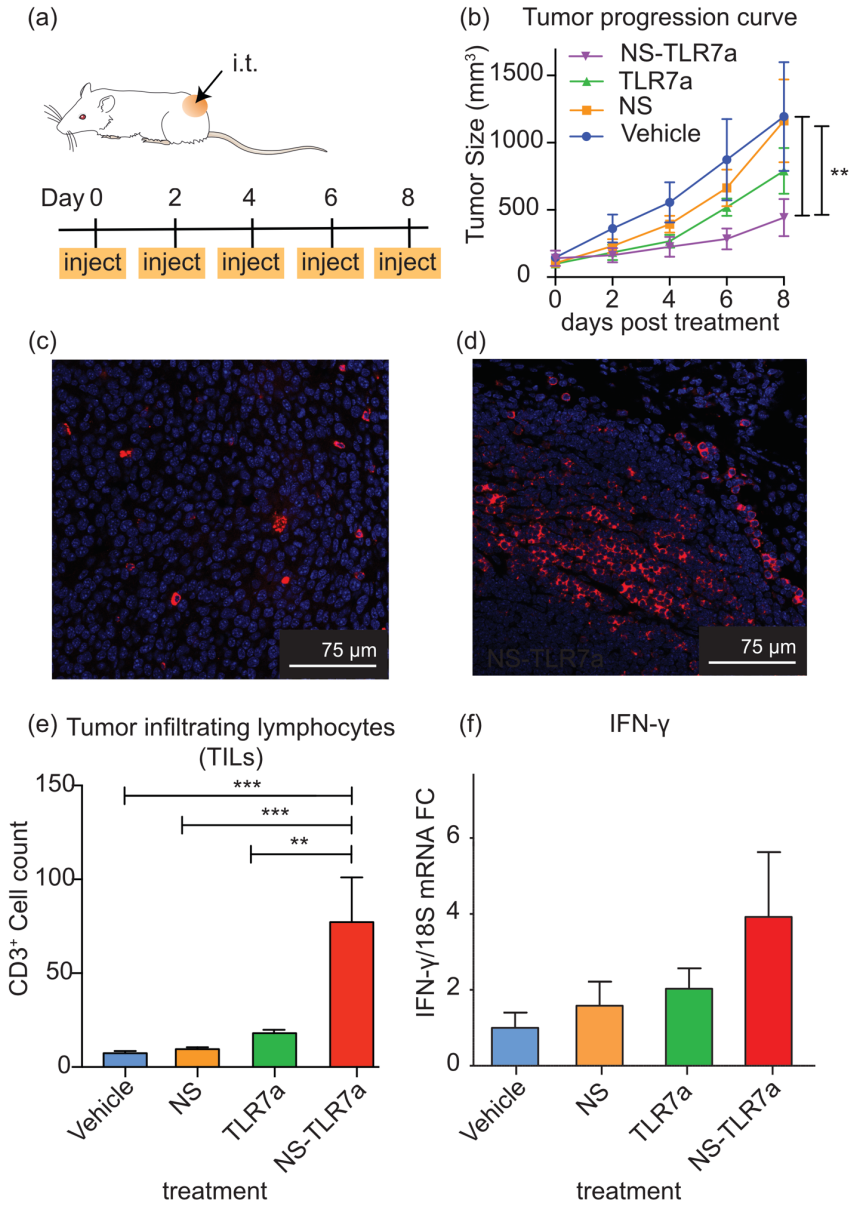

Figure 3. 2: Locally injected NS-TLR7a enhanced the immune response.
Tumor growth regression in mice treated with i.t. NS-TLR7a monotherapy or controls. BALB/c mice were implanted with CT26 cells and treatment began when tumors reached 100 mm^3. Mice (n = 5 per group) were randomized and treated i.t. every other day with vehicle (PBS), silica NS, unconjugated TLR7a, or NS-TLR7a. Tumor tissues were collected on day 8 post-treatment for analysis. (a) Experimental protocol. (b) Average tumor growth curves. (c,d) Immunohistochemistry (IHC) images of $CD3^+$ cells infiltrating into the tumor environments for (e) unconjugated TLR7a or (f) NS-TLR7a locally injected tumor. Representative IHC images are shown. (e) Quantified $CD3^+$ T cells from 30 to 46 random IHC images per group. (f) IFN-γ gene expression level in tumor samples for vehicle, NS, TLR7a, and NS-TLR7a treated groups (n = 4–5 per group). Data shown are mean ± SE of the representative of two independent experiments showing similar results. One-way ANOVA with Bonferroni post hoc test was used for statistical significance analysis indicated as * $p < 0.05$, **$p < 0.01$, ***$p < 0.001$, and n.s. indicates not significant.

3.4.3 Negligible Systemic Toxicity by i.t. Injection of NS-TLR7a

The safety of NS-TLR7a was investigated. First, a systemic cytokine release study was performed to determine the potential toxic effects of the NS-TLR7a agent (Figure 3.3a–e). Single doses of either TLR7a (50 nmol per mouse), NS-TLR7a (50 nmol TLR7a; 1.76 mg NS), NS (1.76 mg per mouse), or vehicle were administered i.t. and blood was collected at 0, 2, and 24 h postinjection. As shown in Figure 3.3b–e, there was a statistically significant increase of IL-6, IL-12, IP-10, and MCP-1 in blood samples collected from NS-TLR7a 2 h postinjection ($p < 0.005$) for IL-6, IL-12, IP-10, and MCP-1, respectively. IL-6 and IL-12 are downstream cytokines of TLR7 signaling and can help differentiate T cells.[122,73] IP-10 and MCP-1 are chemokines that can regulate the migration of immune cells.[123] After 24 h, all treated samples re- turned to baseline levels. No weight loss or behavioral changes were observed in any treatment groups at the given doses. These data show that NS-TLR7a induced only a transient systemic cytokine response which returns to basal levels by 24 h.

Systemic toxicology was also evaluated for repeatedly dosed NS-TLR7a because an effective immunostimulatory agent (i.e., TLR7 agonists) may result in undesired immune-related adverse effects. Four to five female BALB/c mice bearing CT26 tumors on right and left flanks were i.t. injected with 12.5 nmol of NS-TLR7a or vehicle (PBS) every other day for six treatments, and body weight and behavior were observed over the time of treatment (Figure 3.3f). Repeated treatments of NS-TLR7a or vehicle did not induce body weight loss or behavioral changes (reduced activity, piloerection, lethargy, or tachypnea). On day 14, blood and sera were collected for hematological and biochemical analysis (Figure 3.3g,h). At the given dose and administration routes, NS-TLR7a did not induce hepatic, pancreatic, or renal dysfunctions. The electrolyte composition also remained stable after treatment. A minor adverse event in the studies was a

modest erythrocytopenia (Figure 3.3g) that has been previously reported in an oral dosing study of a TLR7a.[124] This effect attenuated throughout the study.[124] Although it was not statistically significant, local NS-TLR7a treatment induced a net reduction of the white blood cells in circulation, including lymphocytes, monocytes, neutrophils, eosinophils, and basophils (Figure 3.3h). The cell numbers of each subtype of white blood cell (neutrophils, eosinophils, basophils, lymphocytes, and monocytes) were combined and averaged. The average number was normalized to the average number of vehicle treated animals. Figure 3.3h indicated that repeated NS-TLR7a therapy had a noticeable trend of reduction after NS-TLR7a therapy compared to the vehicle group ($p = 0.0523$). These data are consistent with other reports that low molecular weight TLR7a induce reversible lymphopenia which is type I IFN-dependent and an on-target adverse effect of this therapy.[125,126] Since lymphopenia induced by TLR7a therapy is transient,[127,128] CBC was performed 24 h post-subcutaneous injection. Neither NS-TLR7a nor TLR7a treatment showed different counts of white blood cells or red blood cells compared to vehicle group, which shows that local injection of NS-TLR7a and TLR7a had negligible adverse effects on mice. Collectively, a repeated local injection, but not a local single injection of NS-TLR7a, has potential to induce erythrocytopenia and lymphopenia, which suggests that further optimization of the dosing schedule will be necessary.

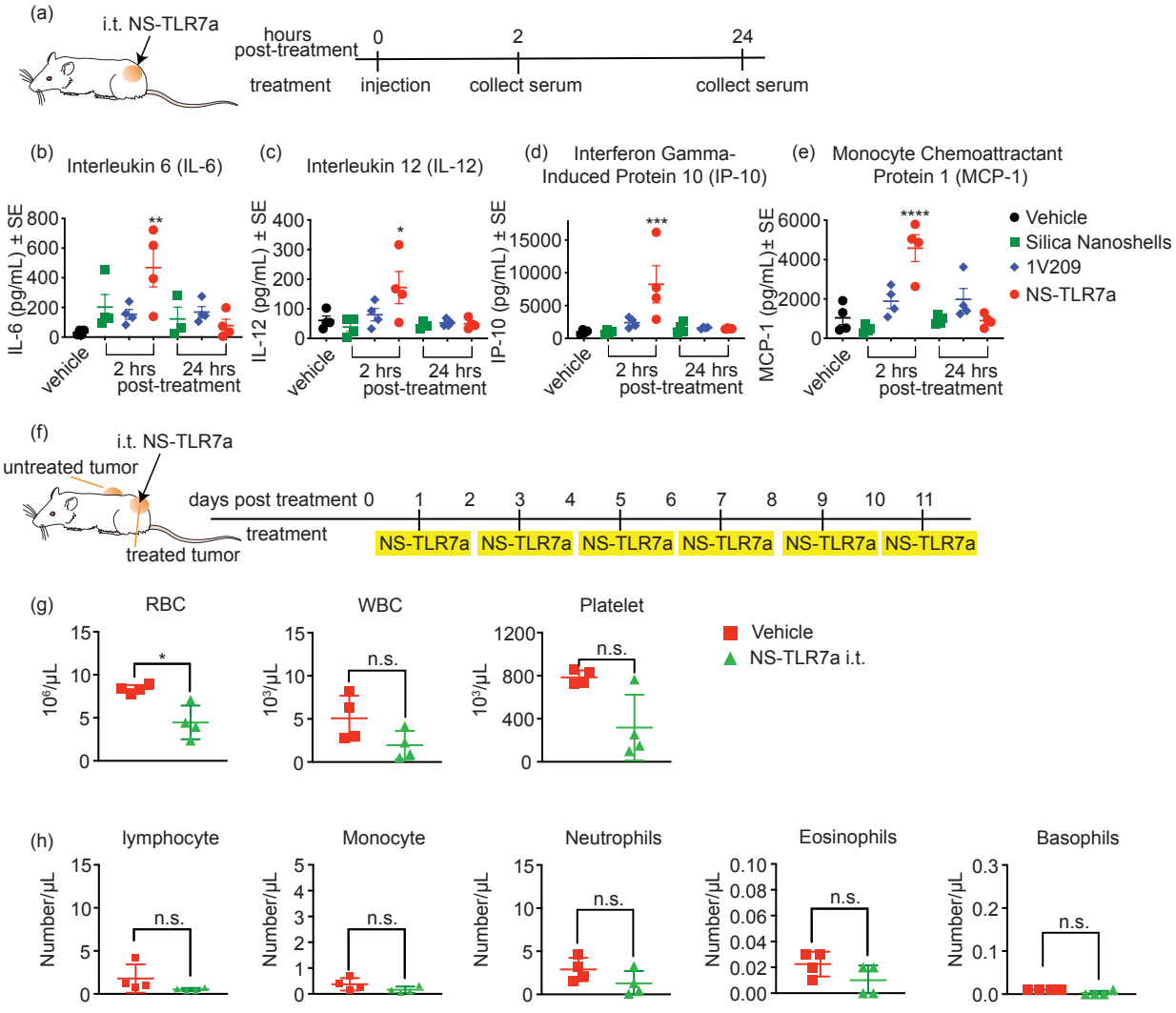

Figure 3. 3: Negligible systemic toxicity by i.t. injection of NS-TLR7a.
(a) Single doses of TLR7a (50 nmol per mouse), NS-TLR7a (50 nmol TLR7a; 1.8 mg NS), NS (1.8 mg/mouse), or vehicle were i.t. administered (n = 4 per group). Blood was collected at 0, 2, and 24 h and sera were isolated. Cytokine levels for of (b) IL-6, (c) IL-12, (d) IP-10, and (e) MCP-1 were measured using Luminex beads assays. Each dot indicates an individual animal and horizontal and vertical bars are means ± SE. One-way ANOVA compared to vehicle group with Bonferroni post hoc test was used for assessing statistical significance. (f–h) Toxicology investigation of NS-TLR7a. (f) Female BALB/c mice (n = 4–5 per group) each bearing two tumors on the right and left flanks were i.t. injected with NS-TLR7a or vehicle every other day for a total of six doses. Whole blood and sera were collected on day 14 post-treatment for complete blood count and biochemistry analyses. The investigation includes: (g) red blood cells, white blood cells, and platelets. h) leukocyte sublet. n.s. indicates not significant and analysis indicated as *($p < 0.05$), **($p < 0.01$), ***($p < 0.001$), and ****($p < 0.0001$).

3.4.4 Tumor Infiltration Lymphocytes Analysis of the Combination Therapy

TLR agonists, being strong immunostimulatory agents, can reverse the immunosuppressive microenvironment created by tumors.[129,130] Intratumoral treatment with TLR7a increases the ratio of M1 (antitumor phenotype) to M2 (protumor phenotype) tumor associated macrophages.[130] TLR7a also causes rapid reduction of myeloid-derived suppressor cells (MDSC) within the tumor microenvironment.[131] The combined TLR7a and PD-L1 blockade results in a reduced number of T regulatory cells in the tumor microenvironment.[132] The above data (Figures 3.2 and 3.3) showed that NS-TLR7a therapy was safe and reduced tumor progression; however, monotherapy with NS-TLR7a only resulted in partial tumor remission. Given the known efficacy of anti-PD-1 (a-PD-1) and anti-CTLA4 (a-CTLA-4) therapies and their ligand expression in this murine tumor type as well as human colorectal cancer,[97] a-PD-1 and a-CTLA-4 therapies were combined with NS-TLR7a therapy. As single agents, both a-PD-1 and a-CTLA-4 are known to have modest therapeutic effects; therefore, the potential treatment combinations were first screened by determining the TIL population. Five treatment groups were used to study the cell population upon combination therapy: (1) vehicle, (2) a-PD-1 + a-CTLA-4, (3) NS-TLR7a + a-CTLA-4 + a-PD-1 (triple therapy), (4) NS-TLR7a + a-PD-1, and (5) NS-TLR7a + a-CTLA-4. Single agent therapy was not chosen as a group because previous studies showed that single blockade of a checkpoint pathway has limited efficacy on CT26 tumors.[133] The treatment protocol is shown in Figure 3.4a: NS-TLR7a was i.t. injected and checkpoint inhibitors a-PD-1 and/or a-CTLA-4 were i.p. injected. Both the directly injected tumors (treated tumor) and the contralateral not directly injected tumors (untreated tumors) were harvested on day 14 after the first treatment to study the TIL in the tumor environment. The NS-TLR7a + a-PD-1 + a-CTLA-4 (triple therapy) treated group showed a greater infiltrated number of $CD45^+$ (leukocytes) and $CD8^+$

cells (cytotoxic T cells) in both treated and untreated tumors (Figure 3.4b,c,f, and g) compared to the other therapy combinations. About a 100-fold increase in $CD45^+CD8^+$ cells ($p = 0.0991$ and 0.0094), in $CD45^+CD8^+$IFN-γ^+ cells ($p = 0.0083$ and 0.005), and in $CD45^+CD8^+$granzyme B^+ cells ($p = 0.0132$ and <0.0001) was observed in both treated and contralateral tumors, respectively, following triple therapy. This shows that the TIL were activated (Figure 3.4d,e,h,i). The $CD8^+$ IFN-γ^+ cells indicate activation of cytotoxic T cells to destroy tumor cells and the $CD8^+$ granzyme B^+ cells can mediate apoptosis.[134,135,136] The increase of immune cells, IFN-γ^+ and granzyme B^+ cells, in both treated and contralateral tumors demonstrate that the improvement of the immune response for the triple therapy is systemic, since only one flank tumor site was injected with NS-TLR7a.

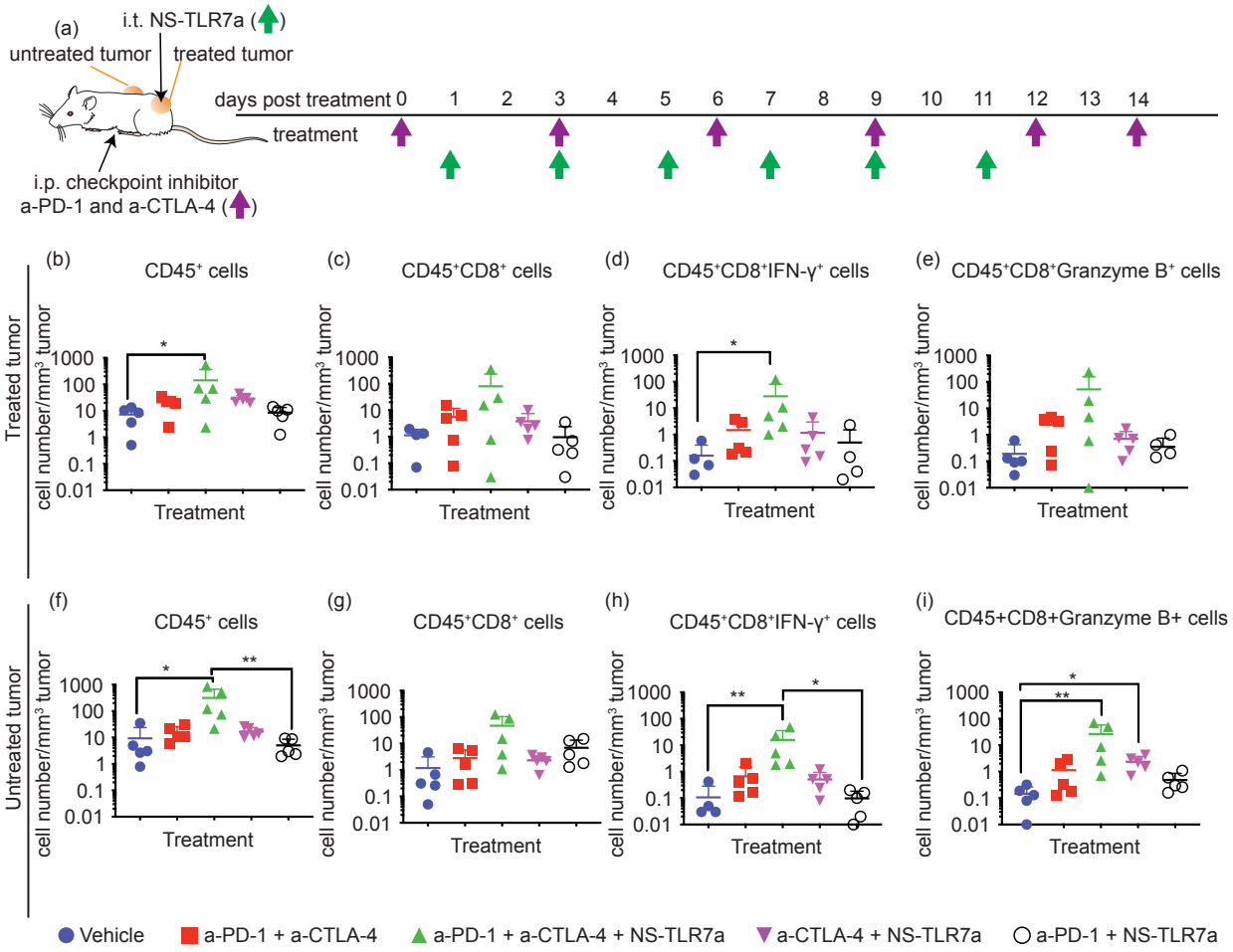

Figure 3. 4: TIL analysis and tumor progression curve following the combination therapy. (a–i) TIL analysis of NS-TLR7a combination therapy. CT26 colon tumor cells were s.c. implanted into female BALB/c mice (4–5 mice per group) at right and left flanks. NS-TLR7a, a-PD-1, and a-CTLA-4 were combined to treat CT26 tumor-bearing mice and the immune cell populations in the tumor microenvironment were investigated. (a) Experimental protocol. Day 0 is defined as the day of the first treatment; NS-TLR7a was i.t. injected into one flank tumor (treated tumor) and checkpoint inhibitors were i.p. injected. In the treated tumor, (b) $CD45^+$, (c) $CD45^+CD8^+$, (d) $CD45^+CD8^+IFN\text{-}\gamma^+$, and (e) $CD45^+CD8^+$granzyme B+ cells were enumerated. The same analyses were done on the untreated contralateral flank tumors (f–i). Immune cell populations in treated and untreated tumors were compared. Each dot indicates an individual animal and vertical and horizontal bars are means ± SE of two independent pooled experiments showing similar results. Data were analyzed by the Kruskal–Walls test using Dunn's multiple comparisons post hoc test.

3.4.5 Tumor Progression Curve Following the Combination Therapy

After determining that triple therapy with NS-TLR7a, a-PD-1, and a-CTLA-4 showed the highest number of activated lymphocyte infiltration, the efficacy of triple therapy to suppress tumor growth and promote long-term survival was investigated in the CT26 model. The combined

checkpoint inhibitors (a-PD-1+a-CTLA-4) were reported to have promising therapeutic treatment outcome, and, therefore, this was chosen for comparison with triple therapy which consisted of NS-TLR7a, a-PD-1, and a-CTLA-4. To assess abscopal effects by induction of systemic anti-tumor immune responses, only one (right side) of the two flank tumors was injected with NS-TLR7a; the treatment protocol is shown in Figure 3.5a. As shown in Figure 3.5b–h, the triple therapy with NS-TLR7a, a-PD-1, and a-CTLA-4 induced complete remission at the treated right side tumor (complete remission rate: 80%) as well as at the contralateral untreated tumor (complete remission rate: 60%). To the authors' knowledge, this is the highest reported systemic remission rate for any two tumor murine colon cancer model in which the starting tumor size is 100 mm^3 that use nanoparticle-based TLR7/8 agonists combined with checkpoint inhibitors.

Several previous studies have used nanoparticle-based TLR7/8 agonists combined with checkpoint inhibitors or chemodrugs to treat cancer. Combination therapy using polymer nanoparticles such as PLGA/PEG to deliver agonists demonstrated a delay in tumor growth;[116,137] however, most studies employed a single-tumor-bearing model, and therefore, it is unknown if these treatments induced abscopal effect that triggers systemic antigen-specific responses with the potential to treat metastatic tumors. Agonists loaded on cyclodextrin combined with a-PD-1 showed excellent therapeutic outcome on a two-tumor mouse model;[112] however, the study used the MC38 tumor model, which is intrinsically responsive to PD-1/PD-L1 blockade.[107]

The earlier nanoparticle biodistribution study showed that locally injected nanoparticles mainly stay at the injected site (Figure 3.1). This observation suggests that the tumor inhibition effects observed for the contralateral tumor is due to a systemic adaptive immune response and less likely due to the small amount of NS-TLR7a that traveled to the distant tumor. To further validate that triple therapy induced tumor-specific adaptive immune responses, the mice with

tumor remission after triple therapy were implanted with CT26 cells on a nontreated flank site, and the growth of rechallenged tumors monitored. No tumor growth was detected in the challenged mice (rechallenged mouse tumor free rate: 100%), proving that immune memory was produced during the initial treatment/remission.

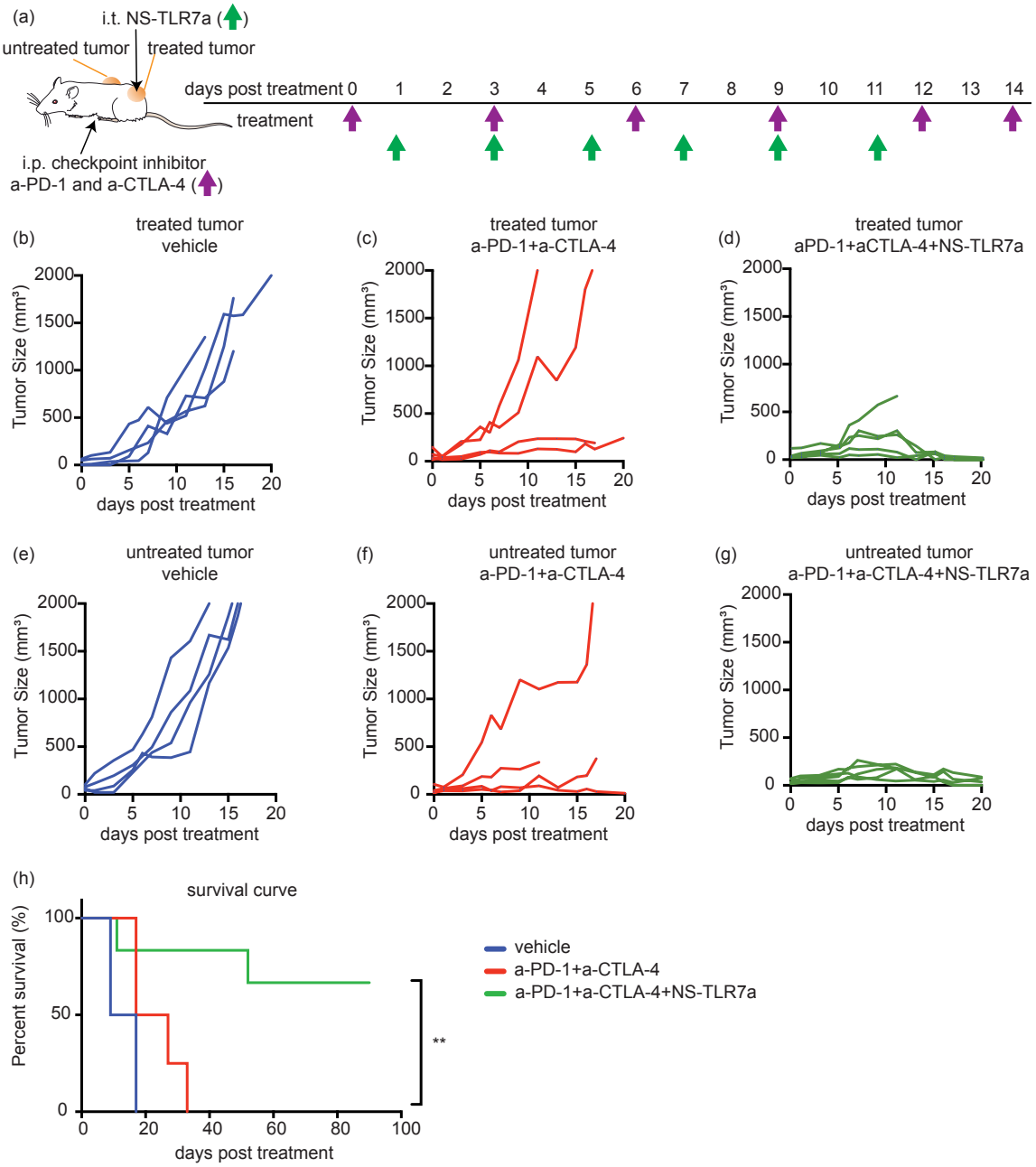

Figure 3. 5: Suppression of tumor growth and survival rates with combination therapy. CT26 colon tumor-bearing mice (8–10 mice per group) were treated with vehicle, combined checkpoint inhibitors (a-PD-1+a-CTLA-4), and checkpoint inhibitors combined with NS-TLR7a (a-PD-1+a-CTLA-4+NS-TLR7a). The treatment protocol is shown in (a). The progressions of both (b–d) treated tumors and (e–g) untreated tumors were monitored. Checkpoint inhibitors (100 μg; a-PD-1 and a-CTLA-4) were injected i.p. three times per week. A 12.5 nmol NS-TLR7a was i.t injected every other day. Mice were sacrificed when tumors reached 2,000 mm^3 or ulceration occurred as required by the UCSD IACUC guideline (policy 9.04). Data were pooled from two independent experiments, which showed similar results. (h) Survival was monitored until day 90 and a Logrank test was used for significance. *means $p < 0.05$, **means $p < 0.01$, ***means $p < 0.001$, and ****means $p < 0.0001$.

3. 5 Conclusions

In this study, the therapeutic efficacy of TLR7a conjugated to silica NS was described when used as monotherapy and as combination therapy with checkpoint inhibitors. Conjugating TLR7a onto NS lengthened the TLR7a retention at the locally injected tumor. As shown in the biodistribution study, i.t injected NS-TLR7a was retained 175× higher in the tumor and 15× lower in the liver when compared to i.v. injected NS-TLR7a. When i.t. NS-TLR7a was combined with checkpoint inhibitor therapy to treat a colorectal cancer model (CT26) that only has modest responses to checkpoint inhibitor immunotherapy, a 10–100× increase in tumor infiltrating lymphocytes and complete tumor remission was observed; treated and contralateral (untreated) tumors had complete remission rates of 80% and 60%, respectively. Triple therapy induced abscopal effects on distant tumors, and the cured treated mice that were rechallenged with CT26 cells rejected the implanted cells, indicating that the triple therapy induced tumor antigen-specific systemic immune response. In summary, i.t. injection of NS conjugated TLR7a may provide a method to induce a safe and more robust antitumor immune response to checkpoint inhibitor immunotherapy, against cancer types that are less responsive to checkpoint inhibitor treatments.

3. 6 Acknowledgements

Chapter 3, in full, contains material as it appears in Advanced Therapeutics 2020. Huang, Ching-Hsin; Mendez, Natalie; Hernandez Echeagaray, Oscar; Weeks, Joi; Wang, James; Yao, Shiyin; Blair, Sarah L.; Gude, Natalie; Trogler, William; Carson, Dennis A.; Hayashi, Tomoko; Kummel, Andrew C., Wiley, 2020. The dissertation author was the primary author of this paper.

References

(1) Kiessling, F.; Fokong, S.; Bzyl, J.; Lederle, W.; Palmowski, M.; Lammers, T. Recent Advances in Molecular, Multimodal and Theranostic Ultrasound Imaging. *Advanced Drug Delivery Reviews* **2014**, *72*, 15–27. https://doi.org/10.1016/j.addr.2013.11.013.

(2) Ferrara, K.; Pollard, R.; Borden, M. Ultrasound Microbubble Contrast Agents: Fundamentals and Application to Gene and Drug Delivery. *Annual Review of Biomedical Engineering* **2007**, *9* (1), 415–447. https://doi.org/10.1146/annurev.bioeng.8.061505.095852.

(3) Uemura, H.; Sano, F.; Nomiya, A.; Yamamoto, T.; Nakamura, M.; Miyoshi, Y.; Miki, K.; Noguchi, K.; Egawa, S.; Homma, Y.; Kubota, Y. Usefulness of Perflubutane Microbubble-Enhanced Ultrasound in Imaging and Detection of Prostate Cancer: Phase II Multicenter Clinical Trial. *World Journal of Urology* **2013**, *31* (5), 1123–1128. https://doi.org/10.1007/s00345-012-0833-1.

(4) Halpern, E. J. Contrast-Enhanced Ultrasound Imaging of Prostate Cancer. *Reviews in urology* **2006**, *8 Suppl 1* (Suppl 1), S29-37.

(5) Unnikrishnan, S.; Klibanov, A. L. Microbubbles as Ultrasound Contrast Agents for Molecular Imaging: Preparation and Application. *American Journal of Roentgenology* **2012**, *199* (2), 292–299. https://doi.org/10.2214/AJR.12.8826.

(6) Sirsi, S.; Borden, M. Microbubble Compositions, Properties and Biomedical Applications. *Bubble science engineering and technology* **2009**, *1* (1–2), 3–17. https://doi.org/10.1179/175889709X446507.

(7) Correas, J.-M.; Bridal, L.; Lesavre, A.; Méjean, A.; Claudon, M.; Hélénon, O. Ultrasound Contrast Agents: Properties, Principles of Action, Tolerance, and Artifacts. *European Radiology* **2001**, *11* (8), 1316–1328. https://doi.org/10.1007/s003300100940.

(8) Sarkar, K.; Katiyar, A.; Jain, P. Growth and Dissolution of an Encapsulated Contrast Microbubble: Effects of Encapsulation Permeability. *Ultrasound in Medicine & Biology* **2009**, *35* (8), 1385–1396. https://doi.org/10.1016/j.ultrasmedbio.2009.04.010.

(9) Schutt, E. G.; Klein, D. H.; Mattrey, R. M.; Riess, J. G. Injectable Microbubbles as Contrast Agents for Diagnostic Ultrasound Imaging: The Key Role of Perfluorochemicals. *Angewandte Chemie International Edition* **2003**, *42* (28), 3218–3235. https://doi.org/10.1002/anie.200200550.

(10) Liberman, A.; Martinez, H. P.; Ta, C. N.; Barback, C. V.; Mattrey, R. F.; Kono, Y.; Blair, S. L.; Trogler, W. C.; Kummel, A. C.; Wu, Z. Hollow Silica and Silica-Boron Nano/Microparticles for Contrast-Enhanced Ultrasound to Detect Small Tumors. *Biomaterials* **2012**, *33* (20), 5124–5129. https://doi.org/10.1016/j.biomaterials.2012.03.066.

(11) Lin, P.-L.; Eckersley, R. J.; Hall, E. A. H. Ultrabubble: A Laminated Ultrasound Contrast

Agent with Narrow Size Range. *Advanced Materials* **2009**, *21* (38â□“39), 3949–3952. https://doi.org/10.1002/adma.200901096.

(12) Hu, H.; Zhou, H.; Du, J.; Wang, Z.; An, L.; Yang, H.; Li, F.; Wu, H.; Yang, S. Biocompatiable Hollow Silica Microspheres as Novel Ultrasound Contrast Agents for in Vivo Imaging. *Journal of Materials Chemistry* **2011**, *21* (18), 6576. https://doi.org/10.1039/c0jm03915b.

(13) Mendez, N.; Liberman, A.; Corbeil, J.; Barback, C.; Viveros, R.; Wang, J.; Wang-Rodriguez, J.; Blair, S. L.; Mattrey, R.; Vera, D.; Trogler, W.; Kummel, A. C. Assessment of in Vivo Systemic Toxicity and Biodistribution of Iron-Doped Silica Nanoshells. *Nanomedicine: Nanotechnology, Biology and Medicine* **2017**, *13* (3), 933–942. https://doi.org/10.1016/j.nano.2016.10.018.

(14) Zhou, Y.-F. High Intensity Focused Ultrasound in Clinical Tumor Ablation. *World journal of clinical oncology* **2011**, *2* (1), 8–27. https://doi.org/10.5306/wjco.v2.i1.8.

(15) Zhou, Y.; Wang, Z.; Chen, Y.; Shen, H.; Luo, Z.; Li, A.; Wang, Q.; Ran, H.; Li, P.; Song, W.; Yang, Z.; Chen, H.; Wang, Z.; Lu, G.; Zheng, Y. Microbubbles from Gas-Generating Perfluorohexane Nanoemulsions for Targeted Temperature-Sensitive Ultrasonography and Synergistic HIFU Ablation of Tumors. *Advanced materials (Deerfield Beach, Fla.)* **2013**, *25* (30), 4123–4130. https://doi.org/10.1002/adma.201301655.

(16) Hamano, N.; Negishi, Y.; Takatori, K.; Endo-Takahashi, Y.; Suzuki, R.; Maruyama, K.; Niidome, T.; Aramaki, Y. Combination of Bubble Liposomes and High-Intensity Focused Ultrasound (HIFU) Enhanced Antitumor Effect by Tumor Ablation. *Biological & pharmaceutical bulletin* **2014**, *37* (1), 174–177.

(17) Kajiyama, K.; Yoshinaka, K.; Takagi, S.; Matsumoto, Y. Micro-Bubble Enhanced HIFU. *Physics Procedia* **2010**, *3* (1), 305–314. https://doi.org/10.1016/J.PHPRO.2010.01.041.

(18) Liberman, A.; Wu, Z.; Barback, C. V; Viveros, R. D.; Wang, J.; Ellies, L. G.; Mattrey, R. F.; Trogler, W. C.; Kummel, A. C.; Blair, S. L. Hollow Iron-Silica Nanoshells for Enhanced High Intensity Focused Ultrasound. *The Journal of surgical research* **2014**, *190* (2), 391–398. https://doi.org/10.1016/j.jss.2014.05.009.

(19) Wang, X.; Chen, H.; Chen, Y.; Ma, M.; Zhang, K.; Li, F.; Zheng, Y.; Zeng, D.; Wang, Q.; Shi, J. Perfluorohexane-Encapsulated Mesoporous Silica Nanocapsules as Enhancement Agents for Highly Efficient High Intensity Focused Ultrasound (HIFU). *Advanced Materials* **2012**, *24* (6), 785–791. https://doi.org/10.1002/adma.201104033.

(20) Liberman, A.; Wang, J.; Lu, N.; Viveros, R. D.; Allen, C. A.; Mattrey, R. F.; Blair, S. L.; Trogler, W. C.; Kim, M. J.; Kummel, A. C. Mechanically Tunable Hollow Silica Ultrathin Nanoshells for Ultrasound Contrast Agents. *Advanced Functional Materials* **2015**. https://doi.org/10.1002/adfm.201500610.

(21) Martinez, H. P.; Kono, Y.; Blair, S. L.; Sandoval, S.; Wang-Rodriguez, J.; Mattrey, R. F.;

Kummel, A. C.; Trogler, W. C. Hard Shell Gas-Filled Contrast Enhancement Particles for Colour Doppler Ultrasound Imaging of Tumors. *MedChemComm* **2010**, *1* (4), 266–270. https://doi.org/10.1039/c0md00139b.

(22) Phillips, P.; Gardner, · E; Phillips, P.; Gardner, E. Contrast-Agent Detection and Quantification. *Eur Radiol Suppl* **2004**, *14*, 4–10. https://doi.org/10.1007/s10406-004-0075-4.

(23) Liberman, A.; Paul Martinez, H.; Ta, C. N.; Barback, C. V; Mattrey, R. F.; Kono, Y.; Blair, S. L.; Trogler, W. C.; Kummel, A. C.; Wu, Z. Hollow Silica and Silica-Boron Nano/Microparticles for Contrast- Enhanced Ultrasound to Detect Small Tumors. *Biomaterials* **2012**, *33* (20), 5124–5129. https://doi.org/10.1016/j.biomaterials.2012.03.066.

(24) Tung, Y.-S.; Liu, H.-L.; Wu, C.-C.; Ju, K.-C.; Chen, W.-S.; Lin, W.-L. Contrast-Agent-Enhanced Ultrasound Thermal Ablation. *Ultrasound in Med. & Biol.* **2006**, *32* (7), 1103–1110. https://doi.org/10.1016/j.ultrasmedbio.2006.04.005.

(25) Umemura, S.-I.; Kawabata, K.-I.; Sasaki, K. In Vivo Acceleration of Ultrasonic Tissue Heating by Microbubble Agent. *IEEE transactions on ultrasonics, ferroelectrics, and frequency control* **2005**, *52* (10), 1690–1698.

(26) Pohaku Mitchell, K. K.; Liberman, A.; Kummel, A. C.; Trogler, W. C. Iron(III)-Doped, Silica Nanoshells: A Biodegradable Form of Silica. *Journal of the American Chemical Society* **2012**, *134* (34), 13997–14003. https://doi.org/10.1021/ja3036114.

(27) Moyer, T. J.; Zmolek, A. C.; Irvine, D. J. Beyond Antigens and Adjuvants: Formulating Future Vaccines. *The Journal of clinical investigation* **2016**, *126* (3), 799–808. https://doi.org/10.1172/JCI81083.

(28) Skrastina, D.; Petrovskis, I.; Lieknina, I.; Bogans, J.; Renhofa, R.; Ose, V.; Dishlers, A.; Dekhtyar, Y.; Pumpens, P. Silica Nanoparticles as the Adjuvant for the Immunisation of Mice Using Hepatitis B Core Virus-Like Particles. *PLoS ONE* **2014**, *9* (12), e114006. https://doi.org/10.1371/journal.pone.0114006.

(29) Xin, L.; Li, Y.; Soong, L. Role of Interleukin-1beta in Activating the CD11c(High) CD45RB- Dendritic Cell Subset and Priming Leishmania Amazonensis-Specific CD4+ T Cells in Vitro and in Vivo. *Infection and immunity* **2007**, *75* (10), 5018–5026. https://doi.org/10.1128/IAI.00499-07.

(30) Hogenesch, H. Mechanism of Immunopotentiation and Safety of Aluminum Adjuvants. *Frontiers in immunology* **2012**, *3*, 406. https://doi.org/10.3389/fimmu.2012.00406.

(31) Fromen, C. A.; Rahhal, T. B.; Robbins, G. R.; Kai, M. P.; Shen, T. W.; Luft, J. C.; DeSimone, J. M. Nanoparticle Surface Charge Impacts Distribution, Uptake and Lymph Node Trafficking by Pulmonary Antigen-Presenting Cells. *Nanomedicine : nanotechnology, biology, and medicine* **2016**, *12* (3), 677–687.

(32) Pradhan, P.; Qin, H.; Leleux, J. A.; Gwak, D.; Sakamaki, I.; Kwak, L. W.; Roy, K. The Effect of Combined IL10 SiRNA and CpG ODN as Pathogen-Mimicking Microparticles on Th1/Th2 Cytokine Balance in Dendritic Cells and Protective Immunity against B Cell Lymphoma. *Biomaterials* **2014**, *35* (21), 5491–5504.

(33) Xia, Y.; Wu, J.; Du, Y.; Miao, C.; Su, Z.; Ma, G. Bridging Systemic Immunity with Gastrointestinal Immune Responses via Oil-in-Polymer Capsules. *Advanced Materials* **2018**, 1801067.

(34) Zhu, G.; Lynn, G. M.; Jacobson, O.; Chen, K.; Liu, Y.; Zhang, H.; Ma, Y.; Zhang, F.; Tian, R.; Ni, Q.; Cheng, S.; Wang, Z.; Lu, N.; Yung, B. C.; Wang, Z.; Lang, L.; Fu, X.; Jin, A.; Weiss, I. D.; Vishwasrao, H.; Niu, G.; Shroff, H.; Klinman, D. M.; Seder, R. A.; Chen, X. Albumin/Vaccine Nanocomplexes That Assemble in Vivo for Combination Cancer Immunotherapy. *Nature Communications* **2017**, *8* (1), 1954.

(35) Smirnov, D.; Schmidt, J. J.; Capecchi, J. T.; Wightman, P. D. Vaccine Adjuvant Activity of 3M-052: An Imidazoquinoline Designed for Local Activity without Systemic Cytokine Induction. *Vaccine* **2011**, *29* (33), 5434–5442.

(36) Li, C.; Zhang, X.; Chen, Q.; Zhang, J.; Li, W.; Hu, H.; Zhao, X.; Qiao, M.; Chen, D. Synthetic Polymeric Mixed Micelles Targeting Lymph Nodes Trigger Enhanced Cellular and Humoral Immune Responses. *ACS Applied Materials & Interfaces* **2018**, *10* (3), 2874–2889.

(37) Shinchi, H.; Crain, B.; Yao, S.; Chan, M.; Zhang, S. S.; Ahmadiiveli, A.; Suda, Y.; Hayashi, T.; Cottam, H. B.; Carson, D. A. Enhancement of the Immunostimulatory Activity of a TLR7 Ligand by Conjugation to Polysaccharides. *Bioconjugate Chemistry* **2015**, *26* (8), 1713–1723.

(38) Shao, K.; Singha, S.; Clemente-Casares, X.; Tsai, S.; Yang, Y.; Santamaria, P. Nanoparticle-Based Immunotherapy for Cancer. **2015**, *9* (1), 16–30.

(39) Knutson, K. L.; Disis, M. L. Tumor Antigen-Specific T Helper Cells in Cancer Immunity and Immunotherapy. *Cancer Immunology, Immunotherapy* **2005**, *54* (8), 721–728.

(40) Maisonneuve, C.; Bertholet, S.; Philpott, D. J.; De Gregorio, E. Unleashing the Potential of NOD-and Toll-like Agonists as Vaccine Adjuvants.

(41) Schön, M. P.; Schön, M. TLR7 and TLR8 as Targets in Cancer Therapy. *Oncogene* **2008**, *27* (2), 190–199.

(42) Walsh, K. B.; Teijaro, J. R.; Zuniga, E. I.; Welch, M. J.; Fremgen, D. M.; Blackburn, S. D.; von Tiehl, K. F.; Wherry, E. J.; Flavell, R. A.; Oldstone, M. B. A. Toll-like Receptor 7 Is Required for Effective Adaptive Immune Responses That Prevent Persistent Virus Infection. *Cell host & microbe* **2012**, *11* (6), 643–653.

(43) Dumitru, C. D.; Antonysamy, M. A.; Tomai, M. A.; Lipson, K. E. Potentiation of the Anti-

Tumor Effects of Imidazoquinoline Immune Response Modifiers by Cyclophosphamide. *Cancer biology & therapy* **2010**, *10* (2), 155–165.

(44) Latz, E.; Xiao, T. S.; Stutz, A. Activation and Regulation of the Inflammasomes. *Nature reviews. Immunology* **2013**, *13* (6), 397–411.

(45) Conniot, J.; Silva, J. M.; Fernandes, J. G.; Silva, L. C.; Gaspar, R.; Brocchini, S.; Florindo, H. F.; Barata, T. S. Cancer Immunotherapy: Nanodelivery Approaches for Immune Cell Targeting and Tracking. *Frontiers in Chemistry* **2014**, *2*, 105.

(46) Tao, C.; Zhu, Y.; Xu, Y.; Zhu, M.; Morita, H.; Hanagata, N. Mesoporous Silica Nanoparticles for Enhancing the Delivery Efficiency of Immunostimulatory DNA Drugs. *Dalton Trans.* **2014**, *43* (13), 5142–5150.

(47) Warashina, S.; Nakamura, T.; Sato, Y.; Fujiwara, Y.; Hyodo, M.; Hatakeyama, H.; Harashima, H. A Lipid Nanoparticle for the Efficient Delivery of SiRNA to Dendritic Cells. *Journal of Controlled Release* **2016**, *225*, 183–191.

(48) Rosalia, R. A.; Cruz, L. J.; van Duikeren, S.; Tromp, A. T.; Silva, A. L.; Jiskoot, W.; de Gruijl, T.; Löwik, C.; Oostendorp, J.; van der Burg, S. H.; Ossendorp, F. CD40-Targeted Dendritic Cell Delivery of PLGA-Nanoparticle Vaccines Induce Potent Anti-Tumor Responses. *Biomaterials* **2015**, *40*, 88–97.

(49) Sercombe, L.; Veerati, T.; Moheimani, F.; Wu, S. Y.; Sood, A. K.; Hua, S. Advances and Challenges of Liposome Assisted Drug Delivery. *Frontiers in pharmacology* **2015**, *6*, 286.

(50) Narang, Ajits.; Chang, R.-K.; Hussain, M. A. Pharmaceutical Development and Regulatory Considerations for Nanoparticles and Nanoparticulate Drug Delivery Systems. *Journal of Pharmaceutical Sciences* **2013**, *102* (11), 3867–3882.

(51) Kaur, R.; Bramwell, V. W.; Kirby, D. J.; Perrie, Y. Pegylation of DDA:TDB Liposomal Adjuvants Reduces the Vaccine Depot Effect and Alters the Th1/Th2 Immune Responses. *Journal of Controlled Release* **2012**, *158* (1), 72–77.

(52) Kaur, R.; Henriksen-Lacey, M.; Wilkhu, J.; Devitt, A.; Christensen, D.; Perrie, Y. Effect of Incorporating Cholesterol into DDA:TDB Liposomal Adjuvants on Bilayer Properties, Biodistribution, and Immune Responses. *Edificio Empresarial "C"* **2000**, *182*.

(53) Nakano, Y.; Mori, M.; Yamamura, H.; Naito, S.; Kato, H.; Taneichi, M.; Tanaka, Y.; Komuro, K.; Uchida, T. Cholesterol Inclusion in Liposomes Affects Induction of Antigen-Specific IgG and IgE Antibody Production in Mice by a Surface-Linked Liposomal Antigen. *Bioconjugate Chemistry* **2002**, *13* (4), 744–749.

(54) Mahmud, M.; Piwoni, A.; Filiczak, N.; Janicka, M.; Gubernator, J. Long-Circulating Curcumin-Loaded Liposome Formulations with High Incorporation Efficiency, Stability and Anticancer Activity towards Pancreatic Adenocarcinoma Cell Lines In Vitro. *PLOS ONE*

2016, *11* (12), e0167787.

(55) Koide, H.; Asai, T.; Hatanaka, K.; Akai, S.; Ishii, T.; Kenjo, E.; Ishida, T.; Kiwada, H.; Tsukada, H.; Oku, N. T Cell-Independent B Cell Response Is Responsible for ABC Phenomenon Induced by Repeated Injection of PEGylated Liposomes. *International Journal of Pharmaceutics* **2010**, *392* (1–2), 218–223.

(56) Raghuvanshi, R. S.; Katare, Y. K.; Lalwani, K.; Ali, M. M.; Singh, O.; Panda, A. K. Improved Immune Response from Biodegradable Polymer Particles Entrapping Tetanus Toxoid by Use of Different Immunization Protocol and Adjuvants. *International Journal of Pharmaceutics* **2002**, *245* (1–2), 109–121.

(57) Lynn, G. M.; Laga, R.; Darrah, P. A.; Ishizuka, A. S.; Balaci, A. J.; Dulcey, A. E.; Pechar, M.; Pola, R.; Gerner, M. Y.; Yamamoto, A.; Buechler, C. R.; Quinn, K. M.; Smelkinson, M. G.; Vanek, O.; Cawood, R.; Hills, T.; Vasalatiy, O.; Kastenmüller, K.; Francica, J. R.; Stutts, L.; Tom, J. K.; Ryu, K. A.; Esser-Kahn, A. P.; Etrych, T.; Fisher, K. D.; Seymour, L. W.; Seder, R. A. In Vivo Characterization of the Physicochemical Properties of Polymer-Linked TLR Agonists That Enhance Vaccine Immunogenicity. *Nature Biotechnology* **2015**, *33* (11), 1201–1210.

(58) Skwarczynski, M.; Toth, I. Peptide-Based Synthetic Vaccines. *Chemical Science* **2016**, *7* (2), 842–854.

(59) Desai, N. Challenges in Development of Nanoparticle-Based Therapeutics. *The AAPS journal* **2012**, *14* (2), 282–295.

(60) Heidegger, S.; Gößl, D.; Schmidt, A.; Niedermayer, S.; Argyo, C.; Endres, S.; Bein, T.; Bourquin, C. Immune Response to Functionalized Mesoporous Silica Nanoparticles for Targeted Drug Delivery. *Nanoscale* **2016**, *8* (2), 938–948.

(61) Wang, X.; Li, X.; Ito, A.; Yoshiyuki, K.; Sogo, Y.; Watanabe, Y.; Yamazaki, A.; Ohno, T.; Tsuji, N. M. Hollow Structure Improved Anti-Cancer Immunity of Mesoporous Silica Nanospheres In Vivo. *Small* **2016**, *12* (26), 3510–3515. https://doi.org/10.1002/smll.201600677.

(62) Wang, X.; Li, X.; Ito, A.; Watanabe, Y.; Sogo, Y.; Tsuji, N. M.; Ohno, T. Stimulation of in Vivo Antitumor Immunity with Hollow Mesoporous Silica Nanospheres. *Angewandte Chemie - International Edition* **2016**. https://doi.org/10.1002/anie.201506179.

(63) Lu, Y.; Yang, Y.; Gu, Z.; Zhang, J.; Song, H.; Xiang, G.; Yu, C. Glutathione-Depletion Mesoporous Organosilica Nanoparticles as a Self-Adjuvant and Co-Delivery Platform for Enhanced Cancer Immunotherapy. *Biomaterials* **2018**, *175*, 82–92.

(64) Hirai, T.; Yoshikawa, T.; Nabeshi, H.; Yoshida, T.; Tochigi, S.; Ichihashi, K.; Uji, M.; Akase, T.; Nagano, K.; Abe, Y.; Kamada, H.; Itoh, N.; Tsunoda, S.; Yoshioka, Y.; Tsutsumi, Y. Amorphous Silica Nanoparticles Size-Dependently Aggravate Atopic Dermatitis-like Skin

Lesions Following an Intradermal Injection. *Particle and fibre toxicology* **2012**, *9*, 3.

(65) Chan, M.; Hayashi, T.; Kuy, C. S.; Gray, C. S.; Wu, C. C. N.; Corr, M.; Wrasidlo, W.; Cottam, H. B.; Carson, D. A. Synthesis and Immunological Characterization of Toll-Like Receptor 7 Agonistic Conjugates. *Bioconjugate Chemistry* **2009**, *20* (6), 1194–1200.

(66) Suthabanditpong, W.; Takai, C.; Fuji, M.; Buntem, R.; Shirai, T. Improved Optical Properties of Silica/UV-Cured Polymer Composite Films Made of Hollow Silica Nanoparticles with a Hierarchical Structure for Light Diffuser Film Applications. *Phys. Chem. Chem. Phys. Phys. Chem. Chem. Phys* **2016**, *18* (18), 16293–16301.

(67) Hayashi, T.; Rao, S. P.; Takabayashi, K.; Van Uden, J. H.; Kornbluth, R. S.; Baird, S. M.; Taylor, M. W.; Carson, D. A.; Catanzaro, A.; Raz, E. Enhancement of Innate Immunity against Mycobacterium Avium Infection by Immunostimulatory DNA Is Mediated by Indoleamine 2,3-Dioxygenase. *Infection and Immunity* **2001**, *69* (10), 6156–6164.

(68) Vallhov, H.; Gabrielsson, S.; Strømme, M.; Scheynius, A.; Garcia-Bennett, A. E. Mesoporous Silica Particles Induce Size Dependent Effects on Human Dendritic Cells. *Nano Letters* **2007**.

(69) Chang, J.-S.; Ke Liang B. Chang; Deng-Fwu Hwang, A.; Kong, Z.-L. In Vitro Cytotoxicitiy of Silica Nanoparticles at High Concentrations Strongly Depends on the Metabolic Activity Type of the Cell Line.

(70) A, F. B. H. Reactive Oxygen Species (ROS) and Reactive Nitrogen Species (RNS) Generation by Silica in Inflammation and Fibrosis. *Free Radical Biology and Medicine* **2003**, *34* (12), 1507–1516. https://doi.org/10.1016/S0891-5849(03)00149-7.

(71) Chen, L.; Liu, J.; Zhang, Y.; Zhang, G.; Kang, Y.; Chen, A.; Feng, X.; Shao, L. The Toxicity of Silica Nanoparticles to the Immune System. *Nanomedicine* **2018**, *13* (15), 1939–1962.

(72) Lehman, S. E.; Morris, A. S.; Mueller, P. S.; Salem, A. K.; Grassian, V. H.; Larsen, S. C. Silica Nanoparticle-Generated ROS as a Predictor of Cellular Toxicity: Mechanistic Insights and Safety by Design. *Environmental science. Nano* **2016**, *3* (1), 56–66.

(73) Tanaka, T.; Narazaki, M.; Kishimoto, T. IL-6 in Inflammation, Immunity, and Disease. *Cold Spring Harbor perspectives in biology* **2014**, *6* (10), a016295.

(74) Tomić, S.; Đokić, J.; Vasilijić, S.; Ogrinc, N.; Rudolf, R.; Pelicon, P.; Vučević, D.; Milosavljević, P.; Janković, S.; Anžel, I.; Rajković, J.; Rupnik, M. S.; Friedrich, B.; Čolić, M. Size-Dependent Effects of Gold Nanoparticles Uptake on Maturation and Antitumor Functions of Human Dendritic Cells In Vitro. *PLoS ONE* **2014**, *9* (5), e96584.

(75) Seydoux, E.; Rothen-Rutishauser, B.; Nita, I. M.; Balog, S.; Gazdhar, A.; Stumbles, P. A.; Petri-Fink, A.; Blank, F.; von Garnier, C. Size-Dependent Accumulation of Particles in Lysosomes Modulates Dendritic Cell Function through Impaired Antigen Degradation.

International journal of nanomedicine **2014**, *9*, 3885–3902.

(76) Martinez, H. P.; Kono, Y.; Blair, S. L.; Sandoval, S.; Wang-Rodriguez, J.; Mattrey, R. F.; Kummel, A. C.; Trogler, W. C. Hard Shell Gas-Filled Contrast Enhancement Particles for Colour Doppler Ultrasound Imaging of Tumors. *MedChemComm* **2010**, *1* (4), 266–270.

(77) Yang, J.; Lind, J. U.; Trogler, W. C. Synthesis of Hollow Silica and Titania Nanospheres. *Chem. Mater* **2008**, *20* (2875–2877).

(78) Bouvier, N. M.; Palese, P. The Biology of Influenza Viruses. *Vaccine* **2008**, *26 Suppl 4* (Suppl 4), D49-53.

(79) Zhang, H.; Dunphy, D. R.; Jiang, X.; Meng, H.; Sun, B.; Tarn, D.; Xue, M.; Wang, X.; Lin, S.; Ji, Z.; Li, R.; Garcia, F. L.; Yang, J.; Kirk, M. L.; Xia, T.; Zink, J. I.; Nel, A.; Brinker, C. J. Processing Pathway Dependence of Amorphous Silica Nanoparticle Toxicity: Colloidal vs Pyrolytic. **2012**. https://doi.org/10.1021/ja304907c.

(80) Hornung, V.; Bauernfeind, F.; Halle, A.; Samstad, E. O.; Kono, H.; Rock, K. L.; Fitzgerald, K. A.; Latz, E. Silica Crystals and Aluminum Salts Activate the NALP3 Inflammasome through Phagosomal Destabilization. *Nature Immunology* **2008**, *9* (8), 847–856.

(81) Catherine Dostert1, Virginie Pétrilli1, Robin Van Bruggen2, Chad Steele3, Brooke T. Mossman4, J. T. Innate Immune Activation Through Nalp3 Inflammasome Sensing of Asbestos and Silica. *Science (New York, N.Y.)* **2008**, *320* (5876), 674–677.

(82) Morishige, T.; Yoshioka, Y.; Inakura, H.; Tanabe, A.; Yao, X.; Narimatsu, S.; Monobe, Y.; Imazawa, T.; Tsunoda, S.; Tsutsumi, Y.; Mukai, Y.; Okada, N.; Nakagawa, S. The Effect of Surface Modification of Amorphous Silica Particles on NLRP3 Inflammasome Mediated IL-1β Production, ROS Production and Endosomal Rupture. *Biomaterials* **2010**, *31* (26), 6833–6842.

(83) Sandberg, W. J.; Låg, M.; Holme, J. A.; Friede, B.; Gualtieri, M.; Kruszewski, M.; Schwarze, P. E.; Skuland, T.; Refsnes, M. Comparison of Non-Crystalline Silica Nanoparticles in IL-1β Release from Macrophages. *Particle and fibre toxicology* **2012**, *9*, 32.

(84) Al Moussawi, K.; Kazmierczak, B. I. Distinct Contributions of Interleukin-1α (IL-1α) and IL-1β to Innate Immune Recognition of Pseudomonas Aeruginosa in the Lung. *Infection and immunity* **2014**, *82* (10), 4204–4211.

(85) Newton, K.; Dixit, V. M. Signaling in Innate Immunity and Inflammation. *Cold Spring Harbor perspectives in biology* **2012**, *4* (3).

(86) Davis, B. K.; Wen, H.; Ting, J. P.-Y. The Inflammasome NLRs in Immunity, Inflammation, and Associated Diseases. *Annual review of immunology* **2011**, *29*, 707–735.

(87) Ghiringhelli, F.; Apetoh, L.; Tesniere, A.; Aymeric, L.; Ma, Y.; Ortiz, C.; Vermaelen, K.;

Panaretakis, T.; Mignot, G.; Ullrich, E.; Perfettini, J.-L.; Schlemmer, F.; Tasdemir, E.; Uhl, M.; Génin, P.; Civas, A.; Ryffel, B.; Kanellopoulos, J.; Tschopp, J.; André, F.; Lidereau, R.; McLaughlin, N. M.; Haynes, N. M.; Smyth, M. J.; Kroemer, G.; Zitvogel, L. Activation of the NLRP3 Inflammasome in Dendritic Cells Induces IL-1β–Dependent Adaptive Immunity against Tumors. *Nature Medicine* **2009**, *15* (10), 1170–1178.

(88) Russell, R. F.; McDonald, J. U.; Lambert, L.; Tregoning, J. S. Use of the Microparticle Nanoscale Silicon Dioxide as an Adjuvant To Boost Vaccine Immune Responses against Influenza Virus in Neonatal Mice. *Journal of Virology* **2016**, *90* (9), 4735–4744.

(89) Holdsworth, S. R.; Kitching, A. R.; Tipping, P. G. *Th1 and Th2 T Helper Cell Subsets Affect Patterns of Injury and Outcomes in Glomerulonephritis*; 1999; Vol. 55.

(90) Spellberg, B.; Edwards, J. E. Type 1/Type 2 Immunity in Infectious Diseases. *Clinical Infectious Diseases* **2001**, *32* (1), 76–102.

(91) Eisenbarth, S. C.; Colegio, O. R.; O'Connor, W.; Sutterwala, F. S.; Flavell, R. A. Crucial Role for the Nalp3 Inflammasome in the Immunostimulatory Properties of Aluminium Adjuvants. *Nature* **2008**, *453* (7198), 1122–1126.

(92) Wen, Y.; Shi, Y. Alum: An Old Dog with New Tricks. *Emerging Microbes & Infections* **2016**, *5* (3), e25–e25.

(93) Lee, S.; Nguyen, M. T. Recent Advances of Vaccine Adjuvants for Infectious Diseases. *Immune network* **2015**, *15* (2), 51–57.

(94) Ciombor, K. K.; Wu, C.; Goldberg, R. M. Recent Therapeutic Advances in the Treatment of Colorectal Cancer. *Annual Review of Medicine* **2015**, *66* (1), 83–95. https://doi.org/10.1146/annurev-med-051513-102539.

(95) Fakih, M. G. Metastatic Colorectal Cancer: Current State and Future Directions. *Journal of clinical oncology : official journal of the American Society of Clinical Oncology* **2015**, *33* (16), 1809–1824. https://doi.org/10.1200/JCO.2014.59.7633.

(96) Hodi, F. S.; Chesney, J.; Pavlick, A. C.; Robert, C.; Grossmann, K. F.; McDermott, D. F.; Linette, G. P.; Meyer, N.; Giguere, J. K.; Agarwala, S. S.; Shaheen, M.; Ernstoff, M. S.; Minor, D. R.; Salama, A. K.; Taylor, M. H.; Ott, P. A.; Horak, C.; Gagnier, P.; Jiang, J.; Wolchok, J. D.; Postow, M. A. Combined Nivolumab and Ipilimumab versus Ipilimumab Alone in Patients with Advanced Melanoma: 2-Year Overall Survival Outcomes in a Multicentre, Randomised, Controlled, Phase 2 Trial. *The Lancet Oncology* **2016**, *17* (11), 1558–1568. https://doi.org/10.1016/S1470-2045(16)30366-7.

(97) Duraiswamy, J.; Kaluza, K. M.; Freeman, G. J.; Coukos, G. Dual Blockade of PD-1 and CTLA-4 Combined with Tumor Vaccine Effectively Restores T-Cell Rejection Function in Tumors. *Cancer research* **2013**, *73* (12), 3591–3603. https://doi.org/10.1158/0008-5472.CAN-12-4100.

(98) Arora, S. P.; Mahalingam, D. Immunotherapy in Colorectal Cancer: For the Select Few or All? *Journal of gastrointestinal oncology* **2018**, *9* (1), 170–179. https://doi.org/10.21037/jgo.2017.06.10.

(99) Emambux, S.; Tachon, G.; Junca, A.; Tougeron, D. Results and Challenges of Immune Checkpoint Inhibitors in Colorectal Cancer. *Expert Opinion on Biological Therapy* **2018**, *18* (5), 561–573. https://doi.org/10.1080/14712598.2018.1445222.

(100) Le, D. T.; Durham, J. N.; Smith, K. N.; Wang, H.; Bartlett, B. R.; Aulakh, L. K.; Lu, S.; Kemberling, H.; Wilt, C.; Luber, B. S.; Wong, F.; Azad, N. S.; Rucki, A. A.; Laheru, D.; Donehower, R.; Zaheer, A.; Fisher, G. A.; Crocenzi, T. S.; Lee, J. J.; Greten, T. F.; Duffy, A. G.; Ciombor, K. K.; Eyring, A. D.; Lam, B. H.; Joe, A.; Kang, S. P.; Holdhoff, M.; Danilova, L.; Cope, L.; Meyer, C.; Zhou, S.; Goldberg, R. M.; Armstrong, D. K.; Bever, K. M.; Fader, A. N.; Taube, J.; Housseau, F.; Spetzler, D.; Xiao, N.; Pardoll, D. M.; Papadopoulos, N.; Kinzler, K. W.; Eshleman, J. R.; Vogelstein, B.; Anders, R. A.; Diaz, L. A. Mismatch Repair Deficiency Predicts Response of Solid Tumors to PD-1 Blockade. *Science (New York, N.Y.)* **2017**, *357* (6349), 409–413. https://doi.org/10.1126/science.aan6733.

(101) Overman, M. J.; McDermott, R.; Leach, J. L.; Lonardi, S.; Lenz, H.-J.; Morse, M. A.; Desai, J.; Hill, A.; Axelson, M.; Moss, R. A.; Goldberg, M. V; Cao, Z. A.; Ledeine, J.-M.; Maglinte, G. A.; Kopetz, S.; André, T. Nivolumab in Patients with Metastatic DNA Mismatch Repair-Deficient or Microsatellite Instability-High Colorectal Cancer (CheckMate 142): An Open-Label, Multicentre, Phase 2 Study. *The Lancet Oncology* **2017**, *18* (9), 1182–1191. https://doi.org/10.1016/S1470-2045(17)30422-9.

(102) Le, D. T.; Uram, J. N.; Wang, H.; Bartlett, B. R.; Kemberling, H.; Eyring, A. D.; Skora, A. D.; Luber, B. S.; Azad, N. S.; Laheru, D.; Biedrzycki, B.; Donehower, R. C.; Zaheer, A.; Fisher, G. A.; Crocenzi, T. S.; Lee, J. J.; Duffy, S. M.; Goldberg, R. M.; de la Chapelle, A.; Koshiji, M.; Bhaijee, F.; Huebner, T.; Hruban, R. H.; Wood, L. D.; Cuka, N.; Pardoll, D. M.; Papadopoulos, N.; Kinzler, K. W.; Zhou, S.; Cornish, T. C.; Taube, J. M.; Anders, R. A.; Eshleman, J. R.; Vogelstein, B.; Diaz, L. A. PD-1 Blockade in Tumors with Mismatch-Repair Deficiency. *New England Journal of Medicine* **2015**, *372* (26), 2509–2520. https://doi.org/10.1056/NEJMoa1500596.

(103) Boyiadzis, M. M.; Kirkwood, J. M.; Marshall, J. L.; Pritchard, C. C.; Azad, N. S.; Gulley, J. L. Significance and Implications of FDA Approval of Pembrolizumab for Biomarker-Defined Disease. *J Immunother Cancer* **2018**, *6* (1), 35. https://doi.org/10.1186/s40425-018-0342-x.

(104) Le, D. T.; Uram, J. N.; Wang, H.; Bartlett, B.; Kemberling, H.; Eyring, A.; Azad, N. S.; Laheru, D.; Donehower, R. C.; Crocenzi, T. S.; Goldberg, R. M.; Fisher, G. A.; Lee, J. J.; Greten, T. F.; Koshiji, M.; Kang, S. P.; Anders, R. A.; Eshleman, J. R.; Vogelstein, B.; Diaz, L. A. Programmed Death-1 Blockade in Mismatch Repair Deficient Colorectal Cancer. *Journal of Clinical Oncology* **2016**, *34* (15_suppl), 103–103. https://doi.org/10.1200/JCO.2016.34.15_suppl.103.

(105) Fellner, C. Promising Drugs in Clinical Development To Treat Advanced Colorectal Cancer. *PT* **2017**, *42* (4), 262–265.

(106) Castle, J. C.; Loewer, M.; Boegel, S.; de Graaf, J.; Bender, C.; Tadmor, A. D.; Boisguerin, V.; Bukur, T.; Sorn, P.; Paret, C.; Diken, M.; Kreiter, S.; Türeci, Ö.; Sahin, U. Immunomic, Genomic and Transcriptomic Characterization of CT26 Colorectal Carcinoma. *BMC Genomics* **2014**, *15* (1), 190. https://doi.org/10.1186/1471-2164-15-190.

(107) Efremova, M.; Rieder, D.; Klepsch, V.; Charoentong, P.; Finotello, F.; Hackl, H.; Hermann-Kleiter, N.; Löwer, M.; Baier, G.; Krogsdam, A.; Trajanoski, Z. Targeting Immune Checkpoints Potentiates Immunoediting and Changes the Dynamics of Tumor Evolution. *Nature communications* **2018**, *9* (1), 32. https://doi.org/10.1038/s41467-017-02424-0.

(108) Yu, G.; Wu, Y.; Wang, W.; Xu, J.; Lv, X.; Cao, X.; Wan, T. Low-Dose Decitabine Enhances the Effect of PD-1 Blockade in Colorectal Cancer with Microsatellite Stability by Re-Modulating the Tumor Microenvironment. *Cellular & Molecular Immunology* **2019**, *16* (4), 401–409. https://doi.org/10.1038/s41423-018-0026-y.

(109) Huang, C.-H.; Mendez, N.; Echeagaray, O. H.; Weeks, J.; Wang, J.; Vallez, C. N.; Gude, N.; Trogler, W. C.; Carson, D. A.; Hayashi, T.; Kummel, A. C. Conjugation of a Small-Molecule TLR7 Agonist to Silica Nanoshells Enhances Adjuvant Activity. *ACS Applied Materials & Interfaces* **2019**, *11* (30), 26637–26647. https://doi.org/10.1021/acsami.9b08295.

(110) Tosolini, M.; Kirilovsky, A.; Mlecnik, B.; Fredriksen, T.; Mauger, S.; Bindea, G.; Berger, A.; Bruneval, P.; Fridman, W.-H.; Pagès, F.; Galon, J. Clinical Impact of Different Classes of Infiltrating T Cytotoxic and Helper Cells (Th1, Th2, Treg, Th17) in Patients with Colorectal Cancer. *Cancer research* **2011**, *71* (4), 1263–1271. https://doi.org/10.1158/0008-5472.CAN-10-2907.

(111) Chen, Q.; Xu, L.; Liang, C.; Wang, C.; Peng, R.; Liu, Z. Photothermal Therapy with Immune-Adjuvant Nanoparticles Together with Checkpoint Blockade for Effective Cancer Immunotherapy. *Nature Communications* **2016**, *7* (1), 13193. https://doi.org/10.1038/ncomms13193.

(112) Rodell, C. B.; Arlauckas, S. P.; Cuccarese, M. F.; Garris, C. S.; Li, R.; Ahmed, M. S.; Kohler, R. H.; Pittet, M. J.; Weissleder, R. TLR7/8-Agonist-Loaded Nanoparticles Promote the Polarization of Tumour-Associated Macrophages to Enhance Cancer Immunotherapy. *Nature Biomedical Engineering* **2018**, *2* (8), 578–588. https://doi.org/10.1038/s41551-018-0236-8.

(113) Kim, H.; Sehgal, D.; Kucaba, T. A.; Ferguson, D. M.; Griffith, T. S.; Panyam, J. Acidic PH-Responsive Polymer Nanoparticles as a TLR7/8 Agonist Delivery Platform for Cancer Immunotherapy. *Nanoscale* **2018**, *10* (44), 20851–20862. https://doi.org/10.1039/C8NR07201A.

(114) Alcazer, V.; Bonaventura, P.; Tonon, L.; Wittmann, S.; Caux, C.; Depil, S. Neoepitopes-Based Vaccines: Challenges and Perspectives. *European Journal of Cancer* **2019**, *108*, 55–60. https://doi.org/10.1016/J.EJCA.2018.12.011.

(115) Nuhn, L.; De Koker, S.; Van Lint, S.; Zhong, Z.; Catani, J. P.; Combes, F.; Deswarte, K.; Li, Y.; Lambrecht, B. N.; Lienenklaus, S.; Sanders, N. N.; David, S. A.; Tavernier, J.; De Geest, B. G. Nanoparticle-Conjugate TLR7/8 Agonist Localized Immunotherapy Provokes Safe Antitumoral Responses. *Advanced Materials* **2018**, *30* (45), 1803397. https://doi.org/10.1002/adma.201803397.

(116) Schmid, D.; Park, C. G.; Hartl, C. A.; Subedi, N.; Cartwright, A. N.; Puerto, R. B.; Zheng, Y.; Maiarana, J.; Freeman, G. J.; Wucherpfennig, K. W.; Irvine, D. J.; Goldberg, M. S. T Cell-Targeting Nanoparticles Focus Delivery of Immunotherapy to Improve Antitumor Immunity. *Nature Communications* **2017**, *8* (1), 1747. https://doi.org/10.1038/s41467-017-01830-8.

(117) Euhus, D. M.; Hudd, C.; Laregina, M. C.; Johnson, F. E. Tumor Measurement in the Nude Mouse. *Journal of Surgical Oncology* **1986**. https://doi.org/10.1002/jso.2930310402.

(118) Livak, K. J.; Schmittgen, T. D. Analysis of Relative Gene Expression Data Using Real-Time Quantitative PCR and the 2−ΔΔCT Method. *Methods* **2001**, *25* (4), 402–408. https://doi.org/10.1006/meth.2001.1262.

(119) Duan, X.; Li, Y. Physicochemical Characteristics of Nanoparticles Affect Circulation, Biodistribution, Cellular Internalization, and Trafficking. *Small* **2013**, *9* (9–10), 1521–1532. https://doi.org/10.1002/smll.201201390.

(120) Brown, A. L.; Kai, M. P.; DuRoss, A. N.; Sahay, G.; Sun, C. Biodistribution and Toxicity of Micellar Platinum Nanoparticles in Mice via Intravenous Administration. *Nanomaterials (Basel, Switzerland)* **2018**, *8* (6). https://doi.org/10.3390/nano8060410.

(121) Yang, L.; Kuang, H.; Zhang, W.; Aguilar, Z. P.; Wei, H.; Xu, H. Comparisons of the Biodistribution and Toxicological Examinations after Repeated Intravenous Administration of Silver and Gold Nanoparticles in Mice. *Scientific Reports* **2017**, *7* (1), 3303. https://doi.org/10.1038/s41598-017-03015-1.

(122) Macatonia, S. E.; Hosken, N. A.; Litton, M.; Vieira, P.; Hsieh, C. S.; Culpepper, J. A.; Wysocka, M.; Trinchieri, G.; Murphy, K. M.; O'Garra, A. Dendritic Cells Produce IL-12 and Direct the Development of Th1 Cells from Naive CD4+ T Cells. *Journal of immunology (Baltimore, Md. : 1950)* **1995**, *154* (10), 5071–5079.

(123) Luster, A. D.; Leder, P. IP-10, a -C-X-C- Chemokine, Elicits a Potent Thymus-Dependent Antitumor Response in Vivo. *The Journal of experimental medicine* **1993**, *178* (3), 1057–1065. https://doi.org/10.1084/jem.178.3.1057.

(124) Lanford, R. E.; Guerra, B.; Chavez, D.; Giavedoni, L.; Hodara, V. L.; Brasky, K. M.;

Fosdick, A.; Frey, C. R.; Zheng, J.; Wolfgang, G.; Halcomb, R. L.; Tumas, D. B. GS-9620, an Oral Agonist of Toll-like Receptor-7, Induces Prolonged Suppression of Hepatitis B Virus in Chronically Infected Chimpanzees. *Gastroenterology* **2013**, *144* (7), 1508–1517, 1517.e1-10. https://doi.org/10.1053/j.gastro.2013.02.003.

(125) Pockros, P. J.; Guyader, D.; Patton, H.; Tong, M. J.; Wright, T.; McHutchison, J. G.; Meng, T.-C. Oral Resiquimod in Chronic HCV Infection: Safety and Efficacy in 2 Placebo-Controlled, Double-Blind Phase IIa Studies. *Journal of Hepatology* **2007**, *47* (2), 174–182. https://doi.org/10.1016/j.jhep.2007.02.025.

(126) Baenziger, S.; Heikenwalder, M.; Johansen, P.; Schlaepfer, E.; Hofer, U.; Miller, R. C.; Diemand, S.; Honda, K.; Kundig, T. M.; Aguzzi, A.; Speck, R. F. Triggering TLR7 in Mice Induces Immune Activation and Lymphoid System Disruption, Resembling HIV-Mediated Pathology. *Blood* **2008**, *113* (2), 377–388. https://doi.org/10.1182/blood-2008-04-151712.

(127) Perkins, H.; Khodai, T.; Mechiche, H.; Colman, P.; Burden, F.; Laxton, C.; Horscroft, N.; Corey, T.; Rodrigues, D.; Rawal, J.; Heyen, J.; Fidock, M.; Westby, M.; Bright, H. Therapy with TLR7 Agonists Induces Lymphopenia: Correlating Pharmacology to Mechanism in a Mouse Model. *Journal of Clinical Immunology* **2012**, *32* (5), 1082–1092. https://doi.org/10.1007/s10875-012-9687-y.

(128) Kamphuis, E.; Junt, T.; Waibler, Z.; Forster, R.; Kalinke, U. Type I Interferons Directly Regulate Lymphocyte Recirculation and Cause Transient Blood Lymphopenia. *Blood* **2006**, *108* (10), 3253–3261. https://doi.org/10.1182/blood-2006-06-027599.

(129) Rabinovich, G. A.; Gabrilovich, D.; Sotomayor, E. M. Immunosuppressive Strategies That Are Mediated by Tumor Cells. *Annual review of immunology* **2007**, *25*, 267–296. https://doi.org/10.1146/annurev.immunol.25.022106.141609.

(130) Sato-Kaneko, F.; Yao, S.; Ahmadi, A.; Zhang, S. S.; Hosoya, T.; Kaneda, M. M.; Varner, J. A.; Pu, M.; Messer, K. S.; Guiducci, C.; Coffman, R. L.; Kitaura, K.; Matsutani, T.; Suzuki, R.; Carson, D. A.; Hayashi, T.; Cohen, E. E. W. Combination Immunotherapy with TLR Agonists and Checkpoint Inhibitors Suppresses Head and Neck Cancer. *JCI Insight* **2017**, *2* (18). https://doi.org/10.1172/JCI.INSIGHT.93397.

(131) Spinetti, T.; Spagnuolo, L.; Mottas, I.; Secondini, C.; Treinies, M.; Rüegg, C.; Hotz, C.; Bourquin, C. TLR7-Based Cancer Immunotherapy Decreases Intratumoral Myeloid-Derived Suppressor Cells and Blocks Their Immunosuppressive Function. *OncoImmunology* **2016**, *5* (11), e1230578. https://doi.org/10.1080/2162402X.2016.1230578.

(132) Nishii, N.; Tachinami, H.; Kondo, Y.; Xia, Y.; Kashima, Y.; Ohno, T.; Nagai, S.; Li, L.; Lau, W.; Harada, H.; Azuma, M. Systemic Administration of a TLR7 Agonist Attenuates Regulatory T Cells by Dendritic Cell Modification and Overcomes Resistance to PD-L1 Blockade Therapy. *Oncotarget* **2018**, *9* (17), 13301–13312. https://doi.org/10.18632/oncotarget.24327.

(133) Wang, S.; Campos, J.; Gallotta, M.; Gong, M.; Crain, C.; Naik, E.; Coffman, R. L.; Guiducci, C. Intratumoral Injection of a CpG Oligonucleotide Reverts Resistance to PD-1 Blockade by Expanding Multifunctional CD8+ T Cells. *Proceedings of the National Academy of Sciences of the United States of America* **2016**, *113* (46), E7240–E7249. https://doi.org/10.1073/pnas.1608555113.

(134) Wowk, M. E.; Trapani, J. A. Cytotoxic Activity of the Lymphocyte Toxin Granzyme B. *Microbes and Infection* **2004**, *6* (8), 752–758. https://doi.org/10.1016/J.MICINF.2004.03.008.

(135) Martínez-Lostao, L.; Anel, A.; Pardo, J. How Do Cytotoxic Lymphocytes Kill Cancer Cells? *Clinical cancer research : an official journal of the American Association for Cancer Research* **2015**, *21* (22), 5047–5056. https://doi.org/10.1158/1078-0432.CCR-15-0685.

(136) Chen, L.; Tourvieille, B.; Burns, G. F.; Bach, F. H.; Mathieu-Mahul, D.; Sasportes, M.; Bensussan, A. Interferon: A Cytotoxic T Lymphocyte Differentiation Signal. *European Journal of Immunology* **1986**, *16* (7), 767–770. https://doi.org/10.1002/eji.1830160709.

(137) Seth, A.; Lee, H.; Cho, M. Y.; Park, C.; Korm, S.; Lee, J.-Y.; Choi, I.; Lim, Y. T.; Hong, K. S. Combining Vasculature Disrupting Agent and Toll-like Receptor 7/8 Agonist for Cancer Therapy. *Oncotarget* **2017**, *8* (3), 5371–5381. https://doi.org/10.18632/oncotarget.14260.